Simulation of Solid State Qubit Control and Readout

by

Zhenyi Qi

A dissertation submitted in partial fulfillment of
the requirements for the degree of

Doctor of Philosophy
(Physics)

at the

UNIVERSITY OF WISCONSIN-MADISON

2019

Date of final oral examination: 08/06/2019

The dissertation is approved by the following members of the Final Oral Committee:

Vavilov, Maxim G., Professor, Department of Physics

Kolkowitz, Shimon, Professor with Some Titles, Department of Physics

McDermott, Robert, Professor, Department of Physics

Knezevic, Irena, Professor, Electric and Computer Engineering

Kechedzhi, Kostyantyn, Research Scientist, Google Inc.

Simulation of Solid State Qubit Control and Readout

by

Zhenyi Qi

Submitted in partial fulfillment of the
requirements for the degree of
Doctor of Philosophy

Abstract

Simulation of quantum systems on classical computers is one necessary step to better control over quantum systems. Good control needs to be both efficient and precise. Through numerical modeling, one can have a better idea about the relevant timescales of a quantum system under qubit operations and how it is affected by the environment when taking into account the interaction between the system and the environment. In this thesis, we simulated the control and readout processes of two solid-state qubit systems, namely, semiconductor qubits and superconducting qubits. For the semiconductor qubit, we used Bloch-Redfield method to investigate how singlet-triplet qubits are affected by charge noise. For the superconducting qubit, we solved the time-dependent master equation to simulate the dynamics of superconducting qubits under various two-qubit gates for both fixed-coupling qubits and tunable couplers. We compared the performance of different two-qubit gates and discussed their advantages and disadvantages. Quantum Monte Carlo method is also used to solve the Lindblad equation to more efficiently catch the important dynamics of a high-dimensional Hilbert space and optimize the readout of a superconducting qubit in a multi-qubit system.

Thesis Advisor: Maxim G. Vavilov
Title: Professor

Acknowledgments

First and foremost, I really want to express my deepest gratitude to my graduate advisor, Maxim G. Vavilov, who guides me through all the difficulties in my research with enormous patience and is always encouraging, supportive (financially and career-wise) and inspiring. Maxim doesn't talk much but is always there when I need help (especially when I was stuck in research and when I was preparing presentations and interviews). During our conversations on physics, Maxim is too nice and patient to be a (stereotypical) Russian advisor. I was a total moron at least in the field of quantum computing before I worked with Maxim but he put a lot of trust on me and turned me into a more confident person, which will have a profound positive effect on my life. Most importantly, I've been tought by Maxim to always push a step further in research – polished presentations of figures and clearer understanding of the underlying physics. Maxim, you also has a slightly weird sense of humor that people can only find in physicists, which makes doing physics with you even more fun.

Thanks to all my committee members. Robert McDermott, thank you so much for providing a lot of support for my career. Shimon Kolkowitz and Irena Knezevic, I am really honored to have you on my committee and appreciate you spending the time reading my thesis and attending my defense!

I also would like to thank Susan Coppersmith for getting me started in the field of quantum computing. Susan gave me a lot of thoughtful suggestions for my study, career and life. Her passion for solving problems has greatly impressed me and set an example of what a researcher should be like.

I send my sincere appreciation to Mark Friesen. Mark, you have always been so supportive, kind and considerable. Working with you has been a very pleasant experience. I also feel so lucky that I have you edit my first paper. It sets a standard of academic writing for me in the rest of my PhD.

I am extremely lucky to meet Kostya Kechechi in the March meeting of 2018 and absolutely enjoyed doing projects with him. The fact that Kostya's solid foundation

in physics always dwarfed me and his inclination to understand every corner of a problem motivate me to do better everytime I tended to stop and push the projects to another level.

Konstantin Nesterov, I want to thank you for always being helpful. I have learned a lot of programming skills from your elegant code and it would have taken me much more time to get started on CHTC computing system without your patient help.

Also thanks to all physicists, computer scientists and engineers who contributed to the famous Qutip Python library. I benefit a lot from their excellent work on building the great toolbox for researchers in this field. Most of my research work would have been much harder without the well-maintained Qutip library.

Dan McCammon, is there anyone in the universe who is nicer, warmer and kinder than you? My vocabulary is really limited (you might have noticed this) to express my appreciation for your kindness and hospitality. You are such an encouraging person. Although we didn't talk often later in my PhD, I want to let you know that I couldn't imagine how I could have made through some tough moments in my PhD without you. Your mere presence is warmth to me. If there's only one person in the world I wish I could be, it is you. You let me know how great a human being could be and it is now my lifetime goal.

Mom, you are trying so hard to be a good mother to your standard but I want you know that you have been a great one for both me and my step-sister. Thank you for giving so much love and a lot of freedom to me.

My step-father, I would not be able to be where I am without your dedication to the family and your sense of responsibility. You are such an optimistic and open-minded person who always brings happiness to people around you. Thank you for being the backbone of our family and creating a wonderful home atmosphere for me and Yan.

Grandmom and grandpa, I miss you so much. It's my lifetime pity that there is no way for me to tell you that I'm a grown-up now and to know if you will be proud of who I am today (but you always were). I will live as if you were by my side.

My cats, XiaoHuang and XiaoBai, thanks for being picky, careless and cute. I'll

bring you to a great journey in the front and buy you better foods and scraching boards.

Jason, let me thank you with the rest of my life.

Contents

Chapter 1

Introduction to quantum computing

It is fair to say quantum mechanics is at least one of the most counterintuitive theories for the brains of human beings (it is probably straightforward for some aliens). One important contribution to this counterintuitive feeling is quantum entanglement. Although we can hardly claim that it is understood, it did already give birth to the exciting field of quantum information science (QIS). Quantum computing, as a subfield of QIS, has attracted considerable attentions of researchers around the world for several decades and has seen impressive progress in both theories and experiments. In this chapter, we summerize the minimal necessary quantum mechanics to understand the rest of the thesis and briefly introduce different physical realizations of qubits so that the readers have a more concrete idea of quantum computers.

1.1 Quantum mechanics in data processing

Although much more complicated and efficient compared to their ancestors, modern computers are still essentially data processors. Data is stored in binary form which is physically realized by open and closed states of transistors and is operated by controling the states of them. When quantum mechanics plays a role, both the form of the data and the data processing change revolutionarily. In terms of the data representation, one of course does not have to be bounded to use sequences of 1s and 0s even in classical computers. But a switch from binary to octonary is theoretically

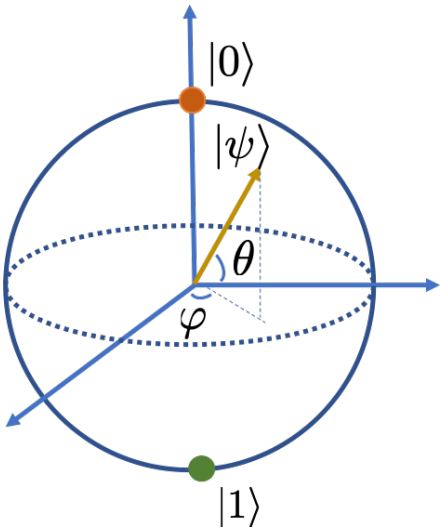

Figure 1-1: Bloch sphere representation of a qubit.

trivial and can be technically challenging. Quantum mechanics, instead, allows the existence of the superposition of 0 and 1, expanding the state space of a single 'bit' from two points to a two-dimensional surface – Bloch sphere. We call this new form of bit as quantum bit, or simply qubit.

A Bloch sphere representation of one possible state of a qubit $|\psi\rangle$ is shown in Figure 1-1. It visually represents a two-dimensional Hilbert space, which is a vector space that possesses inner product. In a two-dimensional vector space, we can take two vectors that are not parallel with each other as a set of basis. The most convenient choice would be two orthogonal vectors, which we can define as state 0 and state 1. In Dirac notation, we use $|0\rangle \equiv (1,0)^T$ and $|1\rangle \equiv (0,1)^T$ to denote them. Then the inner product of two vectors $|\psi_1\rangle$ and $|\psi_2\rangle$ is written as $\langle\psi_1|\psi_2\rangle$ and any state $|\psi\rangle$ of a qubit can be written as a linear combination of the vectors in the set of basis, i.e., $|0\rangle$ and $|1\rangle$. For the one in Figure 1-1, it should be

$$|\psi\rangle = \cos\frac{\theta}{2}|0\rangle + e^{i\varphi}\sin\frac{\theta}{2}|1\rangle. \tag{1.1}$$

When we have n qubits, the dimension of the corresponding Hilbert space is 2^n, since any state $|\psi\rangle$ can be a linear combination of $|1,0,0,...0\rangle$, $|0,1,0,...0\rangle$, $|0,0,1,...0\rangle$ ... $|0,0,0,...1\rangle$, where each $|.\rangle$ has a sequence of n numbers in it and

it is defined as the direct product of 2-dimensional Hilbert spaces of single qubits, i.e., $\left|b_1, b_2, ..., b_n\right\rangle \equiv \left|b1\right\rangle \otimes \left|b_2\right\rangle \otimes \left|b_3\right\rangle \otimes ... \otimes \left|b_n\right\rangle$.

One then realizes that not all the states $\left|\psi\right\rangle$ in a Hilbert space with dimension larger than two can be written in the direct product form of single qubits, otherwise this superposition of states bears no difference than the bits in classical computers since we can always redefine the single qubit basis such that each qubit is either in its 0 state or 1 state. We call those states that cannot be decomposed into the direct product of two-dimensional Hilbert spaces as entangled states. It is this entanglement that enables quantum computers to store/process information exponentially larger/faster than their classical counterparts and possibly shifts the paradigm of data processing in the future.

One of the simplest example of entangled states are Bell states, which are

$$\begin{aligned}
\left|\Phi^+\right\rangle &= \frac{1}{\sqrt{2}}\left(|0\rangle_A \otimes |0\rangle_B + |1\rangle_A \otimes |1\rangle_B\right) \\
\left|\Phi^-\right\rangle &= \frac{1}{\sqrt{2}}\left(|0\rangle_A \otimes |0\rangle_B - |1\rangle_A \otimes |1\rangle_B\right) \\
\left|\Psi^+\right\rangle &= \frac{1}{\sqrt{2}}\left(|0\rangle_A \otimes |1\rangle_B + |1\rangle_A \otimes |0\rangle_B\right) \\
\left|\Psi^-\right\rangle &= \frac{1}{\sqrt{2}}\left(|0\rangle_A \otimes |1\rangle_B - |1\rangle_A \otimes |0\rangle_B\right),
\end{aligned} \tag{1.2}$$

where we use subscript A and B to denote two 'different' qubits. The notation $\left|i\right\rangle_A \otimes \left|j\right\rangle_B$ will be shortened as $\left|i, j\right\rangle$ in the remaining thesis for simplicity. One can easily prove that none of them can be written in product form of two qubits and they form a basis for the two qubit Hilbert space such that any two qubit states can be written as a linear combination of these four states.

1.2 Qubit gates

With the qubits storing the data that can potentially lie in a high-dimensional space in a quantum computer, the goal of the data processing becomes clear. Changing the state of a single qubit is definitely an indispensible part. In addition to that,

generating entangled qubit states is the sole of quantum computing as it makes a quantum computer fundamentally different from a classical one. All these operators, in the language of circuits, are called quantum gates. And a discrete sequence of gates on qubits that describes the data procedure in a quantum computer is called quantum circuit.

Although entanglements can exist in arbitrarily large number of qubits, fortunately, it can be proved that arbitrary unitary transforms can be constructed from a set of single-qubit gates and two-qubit gates[1, p. 191-194].

Single qubit operations that perserve the norm of a qubit state are 2×2 unitary transformations. It is easy to prove that any unitary operation U on a single qubit can be decomposed to two rotations around Z axis and one rotation around Y axis of the Bloch sphere up to a universal phase[1, p. 175-176] . Explicitly,

$$U = e^{i\alpha} R_z(\beta) R_y(\gamma) R_z(\delta), \tag{1.3}$$

where $R_k(\theta) \equiv e^{-i\theta K/2}$ with K is one of the Pauli matrices σ_x, σ_y or σ_z and correspondingly $k = x, y,$ or z. Therefore, to find a universal set of all single-qubit operations, one only need two from the Pauli matrices. There are some other useful single-qubit gates that can simplify the circuit a lot if available, like Hadamard gate and T gate. We will omit the discussions about them and keep in mind that they can always be decomposed into the gates in the universal sets.

In classical computers, controlled operations (If *some condition* then *some action*) are already very important. It correlates different pieces of information and allows more complex logic to be executed. For quantum computers, it plays a even more important role – generate entanglements.

One and probably the most mentioned example of controlled operations is CNOT

gate, the matrix representation of which is

$$\begin{bmatrix} 1 & 0 & 0 & 0 \\ 0 & 1 & 0 & 0 \\ 0 & 0 & 0 & 1 \\ 0 & 0 & 1 & 0 \end{bmatrix} \tag{1.4}$$

in the most standard $\big|0,0\big\rangle, \big|0,1\big\rangle, \big|1,0\big\rangle, \big|1,1\big\rangle$ basis with $\big|0\big\rangle = (1,0)^T$ and $\big|1\big\rangle = (0,1)^T$.

The reason why control gates on qubits can generate entanglements lies in the fact that qubits can be in the superposition state of $\big|0\big\rangle$ and $\big|1\big\rangle$. A simple example would be the generation of a Bell state. If a system of two qubits is in the state of $1/\sqrt{2}(\big|0\big\rangle + \big|1\big\rangle) \otimes \big|0\big\rangle$, after a CNOT gate, it is $1/\sqrt{2}(\big|0,0\big\rangle + \big|1,1\big\rangle)$, which is now a maximally entangled two-qubit state.

1.3 Physical realizations of qubits

While qubit itself is simply a two-level quantum-mechanical system which is ubiquitous, qubits as good candidates for quantum computing are challenging from both physics and engineering perspectives. This is partly because qubtis need to be well isolated to maintain the information, while at the same time can be controlled, i.e., they are needed to interact with the environment such that computations(data processing) or readout(data extraction) can be done. More precisely, in order to make a practical fault-tolerant quantum computers, there are some requirements for the physical system[2], including qubits to be well-characterized, precise initialization, much longer decoherence time than gate operations, ability to construct universal gate sets and a qubit-specific measurement capability.

Despite the difficulties, many physical realizations of qubits are being explored and have made great progress in the last decades. Among them are photons, trapped ions, Ryberg atoms, Nitrogen-Vacancy, nuclear spins in molecules, spins in quantum dots and superconducting qubits. Very roughly speaking, the support for information can

be divided into three classes: photon, spin and charge (some qubits like fluxoniums and phase qubits may not be considered as one of the three kinds).

Because photon interaction with environment is weak, photon qubits are usually born with long decoherence times. The information can be encoded as the photon polarization, the path of a photon and number state in a cavity. Even conversion between polarization and path encoding can be easily realized with a polarizing beam splitter (PBS). The difficult part for using photons to do quantum computing is the realization of two-qubit entangling gates. It was initially believed that materials with very strong nonlinearity is required to implement a conditional phase shift. In 2001, Knill et ac. showed that it is possible to use only linear optical circuits to accomplish scalable quantum computing using single photons[3], after when fast progress has happened and applications of photon qubits on semi-practical problems are already being explored[4–6].

Trapped ions[7], together with Nitrogen-vacancy[8] , NMR qubits[9] and singlet-triplet qubits in quantum dots[10] are using spin degrees of freedom to store the information. Since the accessible magnetic energy associated with spins is quite small, spin carriers need to be located at a relatively isolated environment compared to other qubit systems.

Qubits encoded in charge degree of freedom are used in superconducting charge qubits, electrons in quantum dots (spins can also be used). For charge qubits, uncontrolled charge movements usually lead to decoherence and therefore affect the charge qubit performance.

Among all these qubit realizations, semiconductor qubits and superconducting qubits are two of most promising qubits for building a scalable practically-useful quantum computer. In this thesis, we will focus on these two kinds of qubits. In Chapter 3, we will dive deep into semiconductor single-triplet qubit and its error mechanisms. In Chapter 456, we focus on superconducting qubits, specifically transmon qubit, and discuss two-qubit gate implementations and readout scheme for such qubit systems.

Chapter 2

Modeling of qubit systems

One of the most difficult challenges on the road of building a practially useful quantum computer is its susceptibility to noise. While it is of great interest to show that a noisy intermediate-scale quantum (NISQ) can outperform its classical counterparts[11], it is also at least equally important to understand the noise mechanisms and push the limits towards the threshold for a fully fault-tolerant quantum computing. The numerical approach to a better understanding of factors that affect the gate accuracies requires modeling of a real quantum system that is not isolated from the environment. Quantum computing involves a sequence of operations on a quantum system in a finite range of time, which inevitably invoke master equations in order to describe the evolution of a quantum system.

Except a small number of solvable models, master equations are usually derived perturbatively[12], giving equations of Bloch-Redfield's form[13–17], or written phenomenologically with proper physical constraints, giving the widely used Lindblad equation[18, 19]. [20]

The physical constraints that should be considered for the evolution of a quantum system are[21]:

- The Hermiticiy of the density matrix should be preserved.
- The sum of probabilities over any complete set of orthogonal states should be one, i.e., the trace should be preserved.

- The probability of all possible states of the system should be equal or larger than zero, i.e., the density matrix should be positive semidefinite at all the time.

Lindblad equations are construted to satisfy the above conditions while Bloch-Redfield(BR) equations have long been critized that they can violate the positivity. However, BR method is a handy tool when dealing with a system which interacts with a specific kind of environment and can be very useful when the statistics of the environment noise is known. Thus we'll include a brief review for BR in Sec. 2.1 and an application of BR equation in a real quantum system can be found in Chapter 3. When only phenomenological description can be made about the dissipation of a quantum system, Lindblad equation is widely used. We include a short derivation for Lindblad equation in Sec. 2.2.

Traditionally, both BR and Lindblad methods describe the evolution of the density matrix of the system, which scales with $N \times N$. In addition, the relaxation tensor or superoperator scales with N^4. Solving this equation for an interesting timescale can soon become resource(both time and memory)-consuming as the size of the quantum system increases. Quantum Monte Carlo (QMC), or quantum jump approach is one way to mitigate this growing dimension, making numerical simulations of quantum systems more scalable. A short demonstration of how this method could be used to solve LindBlad equation numerically is presented in 2.3. In Chapter 6, where a relatively large system is considered, QMC is readily applied to help analyze the dynamics of the system.

2.1 Bloch-Redfield equations

Bloch-Redfield method[13, 14, 17, 22, 23] falls into the category of system-plus-reservoir approach that deals with a dissipative quantum system. It starts with the total Hamiltonian of the composite system of the system that we are interested in and the environment (bath) that interacts with the interesting part, which takes the form

$$H = H_S + H_B + H_I, \tag{2.1}$$

where H_S is the system Hamiltonian, H_B is the reservoir Hamiltonian and H_I the interaction between the two. The interaction Hamiltonian can be written as $H_I = \sum S_n B_n$, where S_n act on the system degrees of freedom and B_n on the bath degrees of freedom. Then an accurate description of the total system evolution is given by

$$\dot{\rho} = -\frac{i}{\hbar}\left[H, \rho\right], \tag{2.2}$$

where ρ is the density operator of the whole system. In Liouvillian form, it is written as

$$\dot{\rho} \equiv \mathcal{L}\rho(t), \tag{2.3}$$

where $\mathcal{L} = \mathcal{L}_S + \mathcal{L}_B + \mathcal{L}_I$, with each term $\mathcal{L}_i$ $(i = S, B, I)$, when acting on the density operator, has the form of

$$\mathcal{L}_i\rho = L_i\rho L_i^\dagger - \frac{1}{2}\left(L_i^\dagger L_i\rho + \rho L_i^\dagger L_i\right). \tag{2.4}$$

An important assumption in Bloch-Redfield approach now is to assume that the interaction between the interesting system (referred as 'system' below) and the environment is sufficiently weak such that $\rho(t) \approx \rho_S(t) \otimes \rho_B$, where ρ_S denotes the system density matrix and ρ_B the bath density matrix. Here note that ρ_B is not a function of time because it's assumed to be a large reservoir that's in equilibrium all the time and is hardly affected by evolution of the system.

With this weak interacton assumption, one can either use Eqn. (2.3) and follow *Nakajima-Zwanzig* approach[15, 16], in which a projection is made on the whole space to the system space and $\mathcal{L}_I$ is truncated to its second order, or equivalently, start with Eqn. (2.2), trace over the bath and neglect terms higher than second order in H_I[24, 25]. In the interaction picture, this second order perturbation theory gives

$$\begin{aligned}\frac{\partial}{\partial t}\rho_I(t) = -\frac{1}{\hbar^2}\sum_{m,n}\int_{t_0}^{t} dt' \Big(&C_{mn}\left(t-t'\right)\left[S_{m,I}(t), S_{n,I}\left(t'\right)\rho_I\left(t'\right)\right] \\ &- C_{mn}^*\left(t-t'\right)\left[S_{m,I}(t), \rho_I\left(t'\right)S_{n,I}\left(t'\right)\right]\Big),\end{aligned} \tag{2.5}$$

where $C_{mn}(t) = \mathrm{tr}\left(B_{m,I}(t)B_n\rho_B\right)$ is the bath correlation function, through which the properties of the reservoir enter the evolution of the system. The reservoir is in its thermal equilibrium state, thus bears the form

$$\rho_B = \prod_j e^{-\hbar\omega_j r_j^\dagger r_j/k_BT}(1 - e^{-\hbar\omega_j/k_BT}), \tag{2.6}$$

where $r_j(r_j^\dagger)$ is the mode annihilator(creator) of the environment.

Equation (2.5) is still not convenient for numerical calculation since it is not Markovian. In order to validate a Markovian approximation, one needs to realize that there are two time-scales here. One is the relaxation time of the system τ_r and the other correlation time of the bath τ_B. If $\tau_B \ll \tau_r$, the upper limit of the integration can be pushed to ∞ as we have short correlation time for the bath. Since the system changes so slow, $\rho_I(t') \approx \rho_I(t)$. Substituting the integration variable t' by $\tau = t - t'$, one gets

$$\begin{aligned}\frac{\partial}{\partial t}\rho_I(t) = -\frac{1}{\hbar^2}\sum_{m,n}\int_0^\infty d\tau \,\big(&C_{mn}(\tau)\left[S_{m,I}(t), S_{n,I}(t-\tau)\rho_I(t)\right] \\ &- C^*_{mn}(\tau)\left[S_{m,I}(t), \rho_I(t)S_{n,I}(t-\tau)\right]\big)\end{aligned} \tag{2.7}$$

We can transform the equation back to Schrödinger picture and represent in the system eigenbasis (labeled by a, b, c, d), getting

$$\begin{aligned}\frac{d}{dt}\rho_{ab}(t) = &- i\omega_{ab}\rho_{ab}(t) \\ &- \hbar^{-2}\sum_{m,n}\sum_{c,d}^{\mathrm{sec}}\int_0^\infty d\tau\,\Bigg\{C_{mn}(\tau)\left[\delta_{bd}\sum_n S^m_{aj}S^n_{jc}e^{i\omega_{cj}\tau} - S^m_{ac}S^n_{db}e^{i\omega_{ca}\tau}\right] \\ &+ C_{mn}(-\tau)\left[\delta_{ac}\sum_n S^m_{dj}S^n_{jb}e^{i\omega_{jd}\tau} - S^m_{ac}S^n_{db}e^{i\omega_{bd}\tau}\right]\Bigg\}\rho_{cd}(t),\end{aligned} \tag{2.8}$$

where the "sec" means summation of the secular terms which satisfy $|\omega_{ab} - \omega_{cd}| \ll 1/\tau_r$. In experiments, noise-power spectrum $\mathcal{S}(\omega)$ might be easier to measure. It

relates to the bath correlation function as follows

$$\mathcal{S}(\omega) = \int_{-\infty}^{\infty} d\tau e^{i\omega\tau} C(\tau). \tag{2.9}$$

The above BR equation (2.8) together with information about the power spectrum density gives a relatively clear guide for numerical simulations of the dynamics of a dissipative quantum system, under Born-Markov approximation. When the system Hamiltonian varies with time, both the spectrum and matrix elements of transitions will be modified. If the evolution is slow, one can use the instantaneous eigenbasis. Because of the existance of a new gauge term due to the time-dependence, the new effective Hamiltonion will generally not be diagonal. Under the assumption of slow evolution, one can truncate the diagonalization transformations to a finite number[26]. In Chapter 3, we considered a Landau-Zener interferometry problem using BR equations. Landau-Zener transitions have also been previously studied under BR frame with either classical noise[27, 28] or quantum fluctuations[29–37]. Dephasing due to noise in a Landau-Zener transition has also been well analyzed[38, 39].

2.2 Lindblad equations

Both BR equations and Lindblad equation start from the composite system of the system of interest and its environment. Unlike BR equations, the Lindblad master equation describes the interaction with environment in terms of dephasing and transition processes characterized only by phenomenological decoherence rates[18, 40] and satisfies trace constraint and non-negative eigenvalues.

In this section, the derivation follows the lecture notes[41]. It again starts from Equation (2.3). For an infinitesmal time, we can assume that after tracing over the bath degrees of freedom, the change of system density matrix is

$$\frac{d}{dt}\rho_s \simeq \frac{\rho_s(t+\Delta t) - \rho_s(t)}{\Delta t} = \frac{\mathcal{L}_{\Delta t}\left(\rho_s(t)\right) - \rho_s(t)}{\Delta t}, \tag{2.10}$$

where $\mathcal{L}_{\Delta t}$ maps $\rho_s(t)$ to the reduced density matrix to a later time $(t + \Delta t)$. It can

be proved [42] that this evoluation can be written as

$$\begin{aligned} \rho_{ij}(t+\Delta t) &= \sum_{\alpha=1}^{N^2} \lambda^\alpha \sum_{r,s=1}^{N} E_{ir}^\alpha E_{js}^{\alpha *} \rho_{rs} \quad \text{or} \\ \rho(t+\Delta t) &= \sum_{\alpha=1}^{N^2} \lambda^\alpha \mathbf{E}^\alpha \rho \mathbf{E}^{\alpha\dagger} \end{aligned} , \tag{2.11}$$

with $\sum_{\alpha=1}^{N^2} \lambda^\alpha \mathbf{E}^{\alpha\dagger}\mathbf{E}^\alpha = \mathbf{1}$ and $\sum_{i=1}^{N}\sum_{r=1}^{N} E_{ir}^\alpha E_{ir}^{\beta *} = \mathrm{Tr}\, \mathbf{E}^\alpha \mathbf{E}^{\beta\dagger} = \delta^{\alpha\beta}$ (orthogonality). Here we omit the system subscript s for ρ. We can now define a set of operators $\mathbf{M}^\alpha \equiv \sqrt{\lambda^\alpha}\mathbf{E}^\alpha$, which are called Kraus operators and let

$$\rho(t+\Delta t) = \sum_{\alpha=1}^{N^2} \mathbf{M}^\alpha \rho(t) \mathbf{M}^{\alpha\dagger} = \rho(t) + \Delta t \delta\rho(t) + \mathcal{O}(\Delta t^2). \tag{2.12}$$

Note that one can always use a unitary transformation on $\mathbf{M}^\alpha$ such that there exists one operator, $\mathbf{M}^{1\dagger} \approx \mathbf{1}$. So we have

$$\mathbf{M}^1 \rho(t) \mathbf{M}^{1\dagger} = \rho(t) + \Delta t \delta\rho(t) + \mathcal{O}\left(\Delta t^2\right). \tag{2.13}$$

The fact that $\mathbf{M}^{1\dagger} \approx \mathbf{1}$ allows us to write $\mathbf{M}^1$ in the following form

$$\mathbf{M}_1 = 1 - i\mathbf{K}\Delta t + \mathcal{O}\left(\Delta t^2\right). \tag{2.14}$$

Let

$$\mathbf{H} = \hbar\left(\mathbf{K} + \mathbf{K}^+\right)/2 \text{ and } \mathbf{J} = i\left(\mathbf{K} - \mathbf{K}^\dagger\right)/2. \tag{2.15}$$

We get

$$\begin{aligned} \mathbf{M}^1 \rho \mathbf{M}^{1\dagger} =& (1 - i\mathbf{K}\Delta t)\rho\left(\mathbf{1} + i\mathbf{K}^\dagger \Delta t\right) + \mathcal{O}\left(\Delta t^2\right) \\ =& \rho - i\mathbf{K}\Delta t\rho + i\rho\mathbf{K}^\dagger \Delta t + \mathcal{O}\left(\Delta t^2\right) \\ =& \rho - \frac{i\Delta t}{\hbar}\left[\mathbf{H}, \rho\right] - \Delta t(\mathbf{J}\rho, \rho\mathbf{J}). \end{aligned} \tag{2.16}$$

For $\alpha = 2, 3, ..., N^2$, their contributions are only proportional to Δt, i.e., $\sum_{\alpha\neq 1} \mathbf{M}^\alpha \rho \mathbf{M}^{\alpha\dagger} = \Delta t \delta\rho'$. Let $\mathbf{M}^\alpha = \sqrt{\Delta t}\mathcal{L}^\alpha + \mathcal{O}(\Delta t^{3/2})$ for $\alpha \neq 1$. From the completeness of $\{\mathbf{M}^\alpha\}$,

one can easily find $\mathbf{J} = 1/2 \sum_{\alpha \neq 1} \mathcal{L}^{\alpha\dagger}\mathcal{L}^{\alpha}$. Then we arrive at the most common form of the Lindblad master equation:

$$\frac{\mathrm{d}}{\mathrm{d}t}\rho = \frac{i}{\hbar}\left[\mathbf{H}, \rho\right] + \sum_{\alpha \neq 1}(\mathcal{L}^{\alpha}\rho\mathcal{L}^{\alpha\dagger} - \frac{1}{2}\rho\mathcal{L}^{\alpha\dagger}\mathcal{L}^{\alpha} - \frac{1}{2}\mathcal{L}^{\alpha\dagger}\mathcal{L}^{\alpha}\rho) \tag{2.17}$$

2.3 Quantum Monte Carlo Method

In this section, we'll start from Lindblad equation and see how it can be converted into a form that can be used for stochastic numerical simulations. More rigourous and extensive review can be found in 43.

One thing to keep in mind is that in quantum jump method, at any time, the system is represented by a state vector rather than a density matrix. We'll assume there's one collapse operator in our example Lindblad equation for simplicity. More operators can be generalized straightforwardly. In a small time duration, we have

$$\frac{\Delta\rho}{\Delta t} = -\frac{i}{\hbar}[H, \rho] + \frac{\gamma}{2}\left\{2\hat{c}\rho\hat{c}^{\dagger} - \hat{c}^{\dagger}\hat{c}\rho - \rho\hat{c}^{\dagger}c\right\}, \tag{2.18}$$

where $\hat{c}$ is the only collapse operator. Since the system is kept as a state vector, we should always be able to write $\rho = \big|\Psi\big\rangle\big\langle\Psi\big|$. Then according to the above Lindblad equation, $\big|\Psi\big\rangle\big\langle\Psi\big|$ at later time $t + \Delta t$ relates to the state at t by

$$\begin{aligned}
\big|\Psi(t+\Delta t)\big\rangle\big\langle\Psi(t+\Delta t)\big| \approx & \big|\Psi(t)\big\rangle\big\langle\Psi(t)\big| - \frac{i}{\hbar}\Delta t[H, \big|\Psi\big\rangle\big\langle\Psi\big|] \\
& + \frac{\gamma}{2}\Delta t\left\{2\hat{c}\big|\Psi\big\rangle\big\langle\Psi\big|\hat{c}^{\dagger} - \hat{c}^{\dagger}\hat{c}\big|\Psi\big\rangle\big\langle\Psi\big| - \big|\Psi\big\rangle\big\langle\Psi\big|\hat{c}^{\dagger}\hat{c}\right\} \\
= & \gamma\Delta t\hat{c}\big|\Psi\big\rangle\big\langle\Psi\big|\hat{c}^{\dagger} \\
& + \left\{1 - \frac{i}{\hbar}H\Delta t - \frac{\gamma}{2}\Delta t\hat{c}^{\dagger}\hat{c}\right\}\big|\Psi\big\rangle\big\langle\Psi\big|\left\{1 + \frac{i}{\hbar}H\Delta t - \frac{\gamma}{2}\Delta t\hat{c}^{\dagger}\hat{c}\right\}.
\end{aligned} \tag{2.19}$$

Equation (2.19) can be intepreted as follows: at time t, the probability that a collapse $\hat{c}$ happens at a later time $t+\Delta t$ is proportional to Δt. When we say 'collapse happens', it means the state changes from $\big|\Psi\big\rangle$ to $\big|\Psi_{\text{collapse}}\big\rangle \propto \hat{c}\big|\Psi\big\rangle$ (the normalized state should be $\hat{c}\big|\Psi\big\rangle/\sqrt{\langle\Psi\,|\hat{c}^{\dagger}\hat{c}|\,\Psi\rangle}$). Denoting the probability of collapsing as ΔP,

comparing to the first term of Eqn. (2.19), we have

$$\Delta P = \gamma \Delta t \left\langle \Psi \left| \hat{c}^\dagger \hat{c} \right| \Psi \right\rangle, \tag{2.20}$$

which naturally gives a consistent intepretation of γ as in Lindblad equation: it is a rate associated with the collapse process. Then the second term in Eqn. (2.19) is understood as there is $1 - \Delta P$ chance that the state will evolve from $\left|\Psi\right\rangle$ to $\left|\Psi_{\text{no collapse}}\right\rangle$, where

$$\left|\Psi_{\text{no collapse}}\right\rangle = \frac{\left\{1 - (i/\hbar) H \Delta t - (\gamma/2) \Delta t \hat{a}^\dagger \hat{a}\right\} |\Psi\rangle}{(1 - \Delta P)^{1/2}}.$$

In other words, at any time $t + \Delta t > t$, the state of the system randomly splits into two alternatives:

$$|\Psi\rangle = \begin{cases} |\Psi_{\text{ collapse }}\rangle & \text{with probability } \Delta P \\ |\Psi_{\text{ no collapse }}\rangle & \text{with probability } 1 - \Delta P \end{cases} \tag{2.21}$$

This random process can be easily simulated by a accept-reject method. One can randomly generating a number r that is between zero and one. If r is smaller than ΔP, we accept a collapse and reset the system to state $\left|\Psi_{\text{collapse}}\right\rangle$, otherwise $\left|\Psi_{\text{no collapse}}\right\rangle$. ΔP is given by Eqn. (2.20). This process will generate one possible trajectory of the system. It should be repeated many times and observables of interest should be averaged over many such trajectories.

This stochastic method can be easily horizontally-scaled(more trajectories) in a distributed computing system whereas solving Lindblad equation exactly always requires a vertical scale (larger memory) of space resources as system size increases. Therefore, for larger dimensional system, quantum jump method can be very useful for efficient simulations.

Chapter 3

Semiconductor Singlet-triplet qubit

A system of two 1/2-spin particles, say, electrons, lives in a four-dimensional Hilbert space, which by definition can be spanned by four orthogonal vectors. The eigenstates of the total $\vec{S}^2$ is a convenient choice (of course the definition of 'convenience' depends on the problem of interest), which consists of three triplets:

$$\begin{aligned} |1,-1\rangle &= |\downarrow\downarrow\rangle \\ |1,0\rangle &= \frac{1}{\sqrt{2}}(|\uparrow\downarrow\rangle + |\downarrow\uparrow\rangle) \\ |1,+1\rangle &= |\uparrow\uparrow\rangle \end{aligned} \tag{3.1}$$

and one singlet:

$$|0,0\rangle = \frac{1}{\sqrt{2}}(|\uparrow\downarrow\rangle - |\downarrow\uparrow\rangle), \tag{3.2}$$

where on the left of the equations, the number pairs in $\left|s, m_{\mathrm{s}}\right\rangle$ denote the spin quantum number $s = 0$ or 1 and magnetic spin quantum numbers $m_{\mathrm{s}} = -1, 0, 1$. If the two electrons are seperated (their orbitals are orthogonal), these four states are degenerate in energy when there is no magnetic field.

Whenever we are talking about a qubit, we are refering a two-level quantum-mechanical system. For a system of two spins, we can simply pick two states out of an orthogonal set of four states as our logic 0 and 1. A singlet-triplet qubit, by its name, is a qubit whose 0 and 1 states are chosen to be a singlet and one of the

triplets. If we denote state S as $\left|0\right\rangle$, there is some freedom of choosing either $T_{\pm}$[44] or T_0[45] as state $\left|1\right\rangle$ depending on the kind of coupling we exploit to manipulate the qubit state. In this chapter, we'll use a Si-based $S - T_{-}$ qubit as an example to describe how single qubit manipulation works for a singlet-triplet qubit and then, use the BR equations as introduced in Chapter 2, to show the fact that it subjects to charge noise of the environment can substantially affect its performance as a qubit.

3.1 Single qubit operations

Once two levels as two orthogonal states of a qubit are chosen, the next step to test if it can be used as a real qubit as a building block of a quantum computer is to see if it can be coherently manipulated. The general idea is to tilt the axis of the Hamiltonian by introducing a coupling between the two states so that a Rabi oscillation can happen between state $\left|0\right\rangle$ and state $\left|1\right\rangle$.

The standard method of introducing the coupling between computational $\left|0\right\rangle$ and $\left|1\right\rangle$ states for singlet-triplet qubits in semiconductor quantum dot experiments is via fast electric control of the tunneling rates between two quantum dots where the two spins reside. For $S - T_0$ qubit, this control over the tunneling coupling tunes the exchange interaction. For $S - T_{\pm}$ qubit, a universal magnetic field gives rise to Zeemann splitting among the triplets and a magnetic field gradient couples $T_{\pm}$ to S states. Tunneling coupling controls whether the system is close to the magnetic degeneracy point for $T_{\pm}$ and S. The details are elaborated in the following subsections.

3.1.1 Charge states in double quantum dot

Here we'll take the experiment taken by Xian[46] as an example to explain the configuration and setup of a singlet-triplet qubit experiment. A micrograph of a Si-based double quantum dot that is identical to the device in the experiment is shown in Fig. 3-1(a).

LP and RP are two electrostatic gates that controls the local voltages of the left/right dots so that the energy detuning ε between them can be rapidly changed

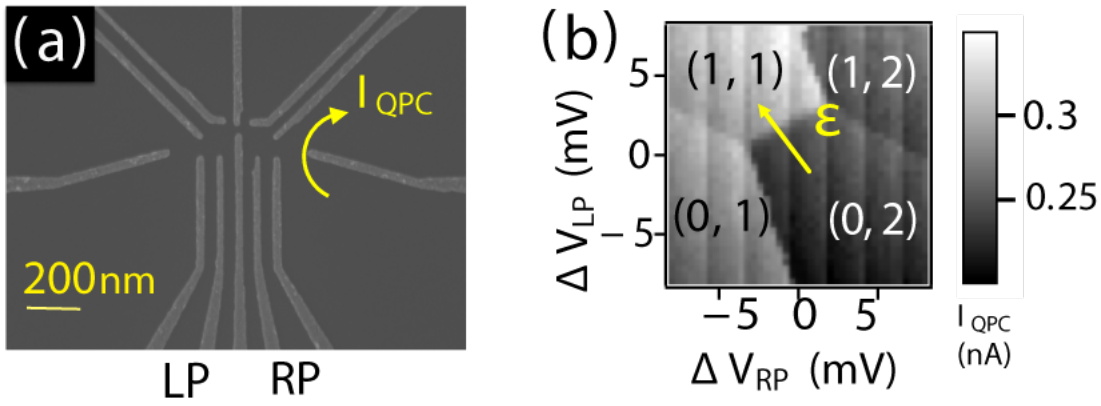

Figure 3-1: (Color online) (a) Micrograph of a double-dot device in a Si/SiGe heterostructure that is lithographically identical to the one used in the experiment [46]. (b) Stability diagram showing the electron occupations in the dots, obtained by measuring the current through the quantum point contact, I_{QPC}, at different voltages $\Delta V_{\mathrm{LP/RP}}$ applied to the left/right gates labeled in (a). The numbers in parentheses are the electron occupations of the two dots.

by the two gates. For different LP and RP gate voltages, the double quantum dots bear different stable charge states. By measuring the current through the quantum point contact (QPC), indicated by the yellow arrow, the charge occupation of each dot can be determined, as shown in the charge stability diagram in Fig. 3-1(b). The number of electrons on each dot is shown on the diagram.

While the charge state $(1, 1)$ allows both singlet and triplets to exist, due to the Pauli exclusion principle, only singlet is allowed for the charge states $(0, 2)$. Therefore, the spin blokage regime is suitable for state preparation and projective measurment and the $(1, 1)$ charge state regime can serve as a qubit manipulation regime. The yellow arrow in Fig. 3-1(b) indicates a pulse from the state preparation regime to state manipulation regime.

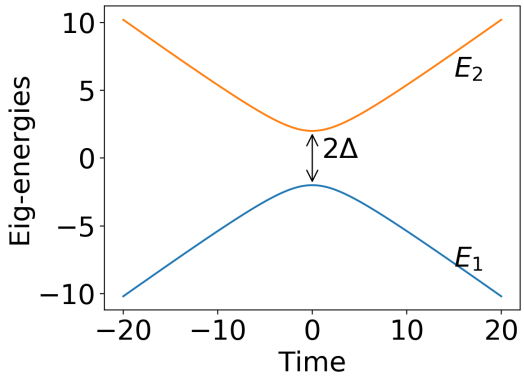

Figure 3-2: Energy diagram of a two-level system for a standard Landau-Zener Hamiltonian (3.3) as a function of time. Here the anti-crossing width $\Delta = 2$ and sweeping velocity is $v = 1$.

3.2 Landau-Zener interferometric measurements

3.2.1 Landau-Zener transitions

Here we deviate for a moment to introduce a more general process of a time-dependent two-level system. Figure 3-2 shows the energy diagram of a two-level system as a function of time t that can be given by the following time-dependent Hamiltonian

$$H = \begin{pmatrix} \varepsilon(t)/2 & \Delta \\ \Delta & -\varepsilon(t)/2 \end{pmatrix}, \tag{3.3}$$

where $\varepsilon = vt$ and v is the sweeping velocity. If the system starts from the lower energy state $|0\rangle = (1,0)^T$ at $t = -\infty$, an adiabatic change of ε will keep the system in its ground state all the time. In the opposite limit when v is very large compared to the squared gap Δ^2, the system neglects the gap and go straight into the state $|1\rangle = (0,1)^T$ at $t \gg 0$. For an intermediate sweep velocity, that the transition probability is given by[47, 48]

$$P_{\mathrm{LZ}} = \exp\left(-\frac{\pi\Delta^2}{2v}\right) \tag{3.4}$$

It can be understood that the anti-crossing acts as a beam-splitter and the state

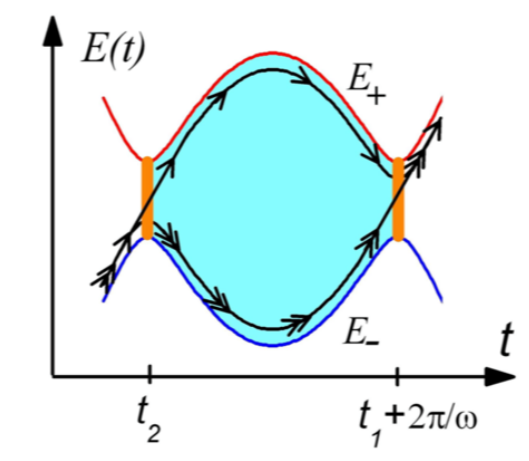

Figure 3-3: Energy diagram of a two-level system as a function of time that forms a Landau-Zener interferometry.

after a single passage through it is a superposition state of $|0\rangle$ and $|1\rangle$. Since P_{LZ} is a continuous function of v between 0 and 1, a propertly choosen velocity can result in equal superposition of the two computational states.

3.2.2 Landau-Zener-Stückelberg interferometry

Now consider a slightly different situation. After passing through an anti-crossing, we allow the system to stay at a finite separation between two levels. Each component of the superposition state accumulates its dynamic phase for some some finite duration of time. Then the system is pushed through another anti-crossing. The process is shown in Fig. 3-3. The phases accumulated by the two states get interfere with each other and the final probability on the original state depends both on the Landau-Zener transition probability and the relative phase between the two levels. Explicitly, it is given by[49–56]

$$\begin{aligned} P_{+} &= 4P_{\mathrm{LZ}}\left(1-P_{\mathrm{LZ}}\right)\sin^{2}\Phi_{\mathrm{St}}, \\ \Phi_{\mathrm{St}} &= \zeta_{2}+\widetilde{\varphi_{\mathrm{S}}}, \\ \zeta_{2} &= \frac{1}{2}\int_{t_{2}}^{t_{1}+2\pi/\omega}\Omega(t)\mathrm{d}t, \\ \widetilde{\varphi}_{\mathrm{S}} &= \varphi_{\mathrm{S}}-\frac{\pi}{2}, \end{aligned} \tag{3.5}$$

where P_{LZ} is the Landau-Zener probability through a single passage, $\Omega(t) = \sqrt{\Delta^2 + \varepsilon(t)^2}$ and $\varphi_{\mathrm{S}} = \frac{\pi}{4} + \delta(\ln\delta - 1) + \arg\Gamma(1 - \mathrm{i}\delta)$ with $\delta = \frac{\Delta^2}{4v}$.

One quick observation is that, when $P_{\mathrm{LZ}} = 1/2$, P_+ can be as large as one [57–59]. Therefore, if we repeat the same process but with varying manipulation time between two anti-crossings, we should get an oscillatory pattern as a function of the manipulation time. The amplitude of this oscillation, usually referred to as *visibility* in the singlet-triplet coherent control context, can in principle be as large as one as long as we find a proper sweeping velocity such that an equal superposition of two states are gotten after a single passage through the anti-crossing.

3.2.3 Landau-Zener-Stückelberg interferometry measurements in a double-quantum-dot

The coherent control of a singlet-triplet qubit mimics the Landau-Zener interfering process described above. For the specific experiment of Xian, the device is fabricated with a micromagnet that induces a magnetic field difference between the dots, δB, and also a uniform magnetic field that, combined with an external magnetic field plus the magnetic fields from nuclear spins, gives rise to a Zeeman splitting between the triplet states. The transverse component of δB induces an anticrossing between the singlet state $\left|S\right\rangle$ and spin-polarized triplet $\left|T_-\right\rangle$. Fig. 3-4(a) shows the schematic energy diagram of the double quantum dot along the detuning direction, indicated by the yellow arrow in Fig. 3-1(b). The left inset is a blowup of the region near the $S - T_-$ anticrossing.

The pulse sequence used in the experiment is shown in Fig. 3-4(b). The detuning is ramped from a negative value through the $S - T_-$ anticrossing to a large positive value, where it is held for a manipulation time τ_s, and then it is ramped back to the initial value, where it is held long enough for the spin state to be measured and reset. The ramp rate is essentially 'sweep velocity' we mentioned in Sec. 3.2.1. When the ramp rate is appropriate, the first ramp leads to occupation of both states with a relative phase that accumulates at large detuning during the manipulation time,

and ramping back to (2,0) gives rise to Landau-Zener-Stückelberg (LZS) oscillations. The probability of being in the singlet state at the end of the sequence oscillates as a function of τ_s, as shown in the inset of Fig. 3-5 by a red solid line. These data were taken with a ramp time of $\tau_r \simeq 45$ ns, which corresponds to a ramp rate of $\sim$4.4 μeV/ns. The coherence time extracted from the oscillations is quite long ($\sim 1.7\ \mu$s), but the visibility is only about 0.24, much less than the value of 1 expected for LZS oscillations in the absence of decoherence. In the experiment, the ramp rate was varied, yielding a peak in the visibility, as indicated by the red circles in the main panel of Fig. 3-5. Here, the data in the inset correspond to a point near the top of the peak.

3.3 Model

Since we are mainly interested in the singlet-triplet $S - T_-$ subspace, we first reduce the full five-level system to two levels, as described in Appendix A. The resulting qubit Hamiltonian can be written as a 2×2 matrix:

$$\hat{H}^{(1)}_{S-T_-} = \begin{pmatrix} -E_S & \frac{h}{2} \\ \frac{h}{2} & E_{T_-} \end{pmatrix}, \tag{3.6}$$

where the singlet and triplet energies are given by $E_S = \sqrt{(\varepsilon/2)^2 + t_c^2}$ and $E_{T_-} = -(\varepsilon/2 + g\mu_B B)$. As in Ref. [46] we assume that the tunnel coupling between the quantum dots, $t_c = t_{c0}\exp(-\varepsilon/\varepsilon_0)$, varies exponentially with the detuning ε, and $\varepsilon_0 \simeq 125\ \mu$eV. Here, g is the gyromagnetic ratio, μ_B is the Bohr magneton, B is the average total magnetic field on the two dots, and the detuning is defined such that $\varepsilon = 0$ at the charge degeneracy point. In Eq. (3.6), the transverse magnetic field gradient causes hybridization of the S and T_- states through the parameter $h = \sqrt{2}h_x \cos(\theta/2)$, where $h_x = g\mu_B \delta B_x$ and $\theta = \arccos(\varepsilon/2E_S)$; see Appendix A for details.

We now apply a unitary transformation

$$\hat{U} = \exp(i\hat{\sigma}_y\phi/2), \quad \phi = \arccos\left(-\frac{E_{T_-} + E_S}{\Delta}\right). \tag{3.7}$$

with $\Delta = \sqrt{(-E_S - E_{T_-})^2 + h^2}$, to diagonalize the instantaneous Hamiltonian, Eq. (3.6), and obtain

$$\begin{aligned} \hat{H}^{(2)}_{S-T_-} &= \hat{U}\hat{H}^{(1)}_{S-T_-}\hat{U}^\dagger - i\hat{U}\dot{\hat{U}}^\dagger \\ &= \frac{E_{T_-} - E_S}{2}\hat{1}_{2\times 2} + \frac{\Delta}{2}\hat{\sigma}_z - \frac{\dot{\phi}}{2}\hat{\sigma}_y. \end{aligned} \tag{3.8}$$

Here, $\hat{1}_{2\times 2}$ is the two-dimensional identity matrix, and $\hat{\sigma}_{y,z}$ are Pauli matrices. Note that E_{T_-} and E_S are functions of time during the ramping pulse, resulting in the time dependence of ϕ. There are two major noise sources in the double quantum dots: nuclear magnetic field fluctuations [44, 60–64] and charge noise [65–68]. Here, We disregard the nuclear magnetic field fluctuations, based on arguments given below. Charge noise is included by incorporating fluctuations in the detuning ε [69], so that $\varepsilon \to \varepsilon + \delta\varepsilon$ is a sum of a controlled gate detuning ε and a fluctuating component $\delta\varepsilon$. In the original five-dimensional basis, the noise takes the diagonal form $\hat{V}^{(0)} = (\delta\varepsilon/2)\mathrm{diag}(1, -1, -1, -1, -1)$. After applying the transformation $\hat{W}$ given by Eq. (A.2), in the qubit subspace, the noise contribution to the Hamiltonian takes the form $\hat{V}^{(1)} = -(\delta\varepsilon/2)\mathrm{diag}(\cos\theta, 1)$. We then apply transformation $\hat{U}$, Eq. (3.7), obtaining

$$\hat{V}^{(2)} = \frac{\delta\varepsilon}{2}(\sin\phi\hat{\sigma}_x + \cos\phi\hat{\sigma}_z)\sin^2\frac{\theta}{2}, \tag{3.9}$$

omitting a term proportional to the identity. The $\hat{\sigma}_x$ term in Eq. (3.9), which causes transitions between the ground and the first excited states, affects the evolution of the density matrix during the ramp across the magnetic anticrossing. The $\hat{\sigma}_z$ term in Eq. (3.9) is diagonal but vanishes at the magnetic anticrossing when $\phi = \pi/2$; This term gives rise to fluctuations of the phase difference between the ground and first excited states. Below, we discuss the effects of these two terms on the system dynamics, showing that the former explains the low visibility, while the latter gives

rise to dephasing that is consistent with the experiment. In this way, we obtain a self-consistent description of the experimental data in Figs. 3-5 and 3-6.

We now apply the Bloch-Redfield (BR) approximation [70–72] introduced in Chapter 2 to describe the dynamics of the double quantum dot in the presence of detuning noise $\hat{V}^{(2)}$. Within this theory, the dynamics are described in terms of transition rates between energy eigenstates in the $S - T_-$ subspace. The detuning fluctuations are characterized by the spectral function $S(\omega) = \int d\tau \langle \delta\varepsilon(t)\delta\varepsilon(t+\tau)\rangle e^{-i\omega\tau}$, where ω is the frequency and $\langle \dots \rangle$ denotes an average over noise realizations. Here, we assume that the noise spectrum for detuning fluctuations has spectral density

$$S(\omega) = \alpha/\omega^{0.7}, \tag{3.10}$$

where α is a constant, as consistent with experiment measurements on recent experimental quantum dot qubits [69]. We then calculate transition rates between eigenstates induced by the noise using Fermi's golden rule, obtaining the master equations for the qubit density matrix ρ describing the hybridized $S - T_-$ two-level system:

$$\dot{\rho}_{00} = \frac{\dot{\phi}}{2}(\rho_{01} + \rho_{10}) - \Gamma\rho_{00} + \Gamma\rho_{11} \tag{3.11a}$$

$$\dot{\rho}_{01} = -\frac{\dot{\phi}}{2}(\rho_{00} - \rho_{11}) - \frac{i}{\hbar}\rho_{01}(\Delta + Z\delta\varepsilon) - \Gamma\rho_{01} \tag{3.11b}$$

$$\dot{\rho}_{11} = -\frac{\dot{\phi}}{2}(\rho_{01} + \rho_{10}) + \Gamma\rho_{00} - \Gamma\rho_{11}\ , \tag{3.11c}$$

and $\rho_{10} = \rho_{01}^*$, where $Z = \sin^2(\theta/2)\cos(\phi)$, and $Z\delta\varepsilon$ is the noise contribution from the $\hat{\sigma}_z$ term in Eq. (3.9). Here, 0 and 1 refer to the instantaneous eigenstates of Eq. (3.6).

The transition rate Γ in Eq. (3.11) characterizes the rate of excitation from the ground state to the excited state and the rate of relaxation of the excited state. To estimate Γ, we assume the delta epsilon noise distribution to be classical because the transition rates between S and T_- are only non-negligible near the $S-T_-$ anticrossing, where the energy separation between the levels is h, which is very small compared to the temperature. In the BR theory we therefore obtain the following form for the

relaxation rate:

$$\Gamma(\varepsilon) = \frac{\pi}{2\hbar^2} \sin^2\phi \sin^4\left(\frac{\theta}{2}\right) S(\Delta(\varepsilon)/\hbar) \ . \tag{3.12}$$

Charge noise and other sources of relaxation give rise to $T_1 \sim 10$ μs, as measured in experiments.[46] Since T_1 is much larger than the ramp time ($10 \sim 100$ ns) in our experiment, we ignore it in our visibility calculations.

3.4 Effect of charge noise

3.4.1 Oscillation Visibility

We now compare the results of our numerical simulations of the differential Eq. (3.11) to experimental measurements of Landau-Zener-Stückelberg interferometry. The experiments presented here use the procedures and methods presented in Ref. [46]. The simulations use the measured values for the average magnetic field (obtained from the period of the LZS oscillations), $g\mu_B B = 0.17$ μeV, and the tunnel coupling at zero detuning $t_{c0} \approx 3.4$ μeV [46]. We ignore the term $Z\delta\varepsilon$ in Eq. (3.11b) during the forward and backward ramps because it vanishes at $\phi = \pi/2$ and is only important for long times, as we explain below, in Sec. 3.4.2. The parameters h and α are not well determined from the experiment, and we adjust them here to optimize the fit to the visibility data shown in Fig. 3-5. For the plots shown in this paper, we use

$$h = 0.042 \ \mu\text{eV}, \qquad \alpha = 47 \ \text{ns}^{-1.7}. \tag{3.13}$$

We note that if one takes the low and high frequency cutoffs of the noise spectrum to be 0 Hz and $1/T_2^*$ with $T_2^* \simeq 1700$ ns respectively, this value of α yields a standard deviation of the detuning fluctuations of 5.7 μeV, which compares well to the experimental estimate of 6.4 μeV [46]. Moreover, we expect the magnetic energy difference h_x to be in the range of $0.01 \sim 0.1$ μeV, since the $S - T_0$ experiment reported for the same device in Ref. [46] indicates a value of $h \simeq 0.061$ μeV for a slightly different

magnetic field configuration. Hence, the fitting result for h obtained above appears to be quite reasonable.

Using these results, we can plot the theoretically determined relaxation ration using Eq. (3.12). As shown in Fig. 3-7(b), the transition rates are strongly peaked at the $S - T_-$ anticrossing. Moreover, we note from Eq. (3.12), the transition rates are large only if the $S - T_-$ anticrossing is not too far from the charge anticrossing.

3.4.2 Oscillation Decay

To account for dephasing during the manipulation period τ_s, which occurs at large detuning $\varepsilon_2 \gg t_c$ far away from charge degeneracy point, we follow Refs. 73, 74. The $\hat{\sigma}_z$ term in Eq. (3.9) gives rise to fluctuations of the phase difference between the qubit eigenenergy states. The amplitude of this term is largest when the detuning is to the left of the magnetic anticrossing, where both $\phi \simeq \pi$ and $\theta \simeq \pi$. However, this part of the system evolution does not influence the LZS interference pattern [45], since during the forward part of the process, the system remains in the ground state, while for the reverse process, a projective measurement to the ground state is performed. Here we discuss dephasing produced by the charge noise at large positive detuning, which is far to the right of the magnetic anticrossing. This part of the cycle dominates the dephasing because the system is held at large detuning ε_2 for a long manipulation time, τ_s.

The phase difference $\delta\varphi$ accumulated due to fluctuations of the detuning ε is

$$\begin{aligned} \delta\varphi(\tau_s) &= Z|_{\varepsilon=\varepsilon_2} \int_0^{\tau_s} \mathrm{d}\tau \delta\varepsilon(\tau) \\ &= Z|_{\varepsilon=\varepsilon_2} \left[\frac{\sin(\omega\tau_s)}{\omega} \xi_\omega^x - \frac{1-\cos(\omega\tau_s)}{\omega} \xi_\omega^y \right], \end{aligned} \tag{3.14}$$

where, $\delta\varepsilon(\tau) = \xi_\omega^x \cos(\omega t) + \xi_\omega^y \sin(\omega t)$, and ξ_ω^x and ξ_ω^y are the two components of the fluctuating Gaussian fields. We can compute the average of ρ_{01} with respect to fluctuation of $\delta\varepsilon$ in Eq. (3.11b) yielding $\rho_{01}(\tau_r + \tau_s) = \rho_{01}(\tau_r)\exp(-\chi(\tau_s))\exp(-\Gamma(\varepsilon_2)\tau_s)$ (see also Refs. 73, 74), where $\exp(-\chi(\tau_s)) = \langle \exp(-i\delta\varphi(\tau_s)) \rangle$ is evaluated by

$$\chi(\tau_s) = Z^2|_{\varepsilon=\varepsilon_2} \int \mathrm{d}\omega \frac{S(\omega)}{4} \left(\frac{\sin(\omega\tau_s/2)}{\omega/2} \right)^2 . \tag{3.15}$$

Taking the noise spectral power Eq. (3.10) with parameter $\alpha = 47$ ns$^{-1.7}$ obtained by fitting Fig. 3-5, one is able to calculate the time-dependence of the LZS oscillations. Multiplying the factor $\exp(-\chi(\tau_s))$ by the amplitude of the return probability P_s obtained in Eqs. (3.11) automatically takes into account both of the dephasing factors Γ and χ, yielding a theoretical prediction for LSZ oscillations under charge noise, that is in good agreement with the experiment, as shown in Fig. 3-6. We note that the parameters used to generate these oscillations are the same as those used in Fig. 3-5.

Figure 3-5 and 3-6 indicate that the numerical results for the oscillation visibility as a function of ramp rate including only charge noise agree well with the experimental data; the visibility as a function of ramp rate, the coherence time of the oscillations, and the long-time limit of the decay curve can all be described by a single set of the parameter values α and h given in Eq. (3.13). The system exhibits both low visibility and long coherence times because the transition rates induced by the charge noise depend strongly on the detuning ε. While these transitions suppress the visibility at the magnetic anticrossing, their effect is very weak at the large detuning values where phase is accumulated, so the coherence time is affected mainly by dephasing, caused by the $\hat{\sigma}_z$ term in Eq. (3.9).

The above theory predicts that the visibility of the LZS oscillations can be increased by increasing the tunnel coupling, as shown in Fig. 3-7(a). This improvement occurs because increasing the tunnel coupling increases the difference in detuning between the charge and magnetic anticrossings; when the anticrossings are well-separated, $\sin^4(\theta/2)$ and $\sin^2(\phi)$ in Eq. (3.12) cannot be large simultaneously.

In conclusion, we expect that the noise models described here could also apply to other types of qubits that exhibit low visibility and long decoherence time[75]. We also expect these results to be of interest to other experimentalists because they predict that the visibility of LZS oscillations can be increased substantially by increasing the interdot tunnel coupling. This chapter exhibits an example of using Bloch-

Redfield equations to describe the a single-qubit system dynamics with a known noise spectrum. The BR equations incorporates the transition rates between eigenenegies induced by the noise and thus explains the visibility reduction.

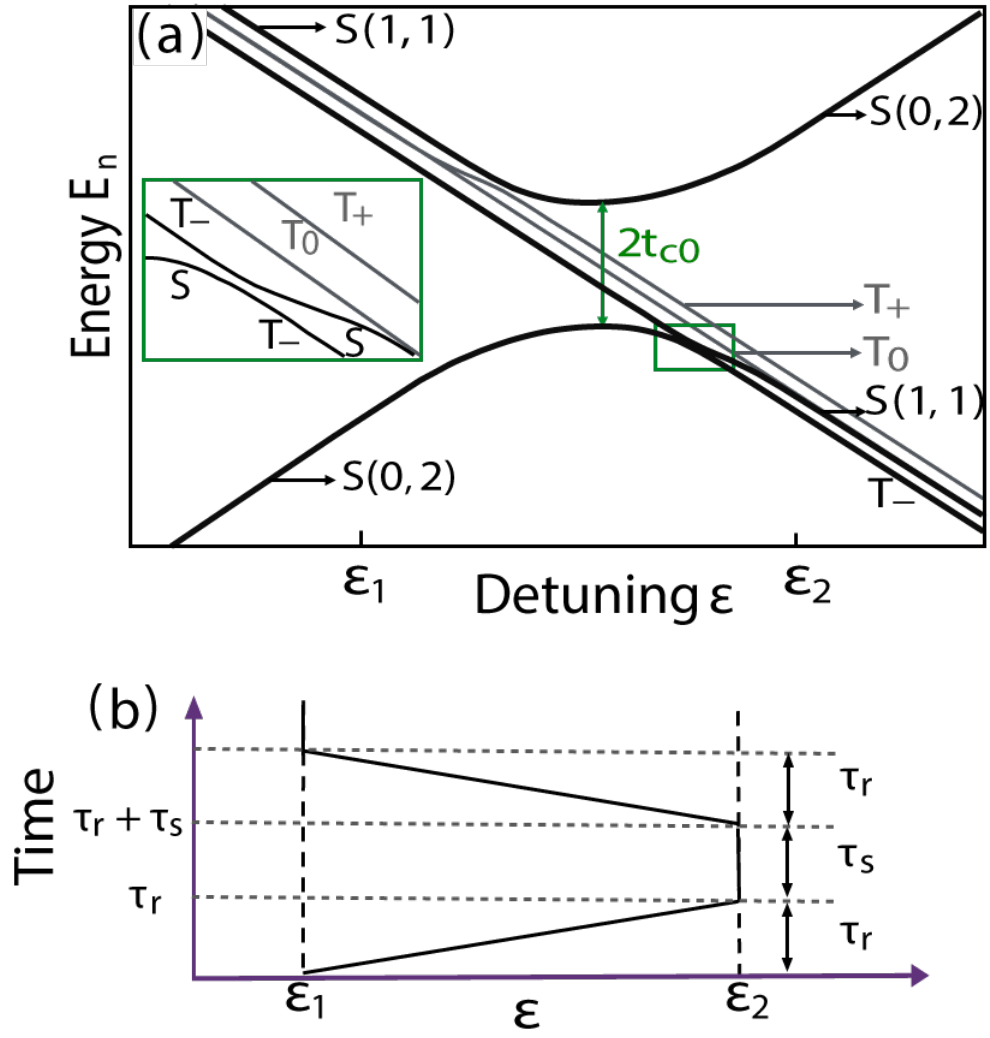

Figure 3-4: (a) Schematic energy diagram of the full five-level system. A small transverse magnetic field gradient causes an anticrossing to occur between the singlet and triplet states $S(1,1)$ and T_-. The left inset is an expanded view of the region in the small green box in the main figure. (b) a schematic of the pulse applied to the detuning ε as a function of time t. The system is ramped from a negative detuning ε_1 to a large positive detuning ε_2 over a ramp time τ_r, held at ε_2 for a manipulation time τ_s, and then ramped back to ε_1 over the time τ_r. The pulse sequence passes through the $S - T_-$ anticrossing twice, giving rise to Landau-Zener-Stückelberg oscillations.

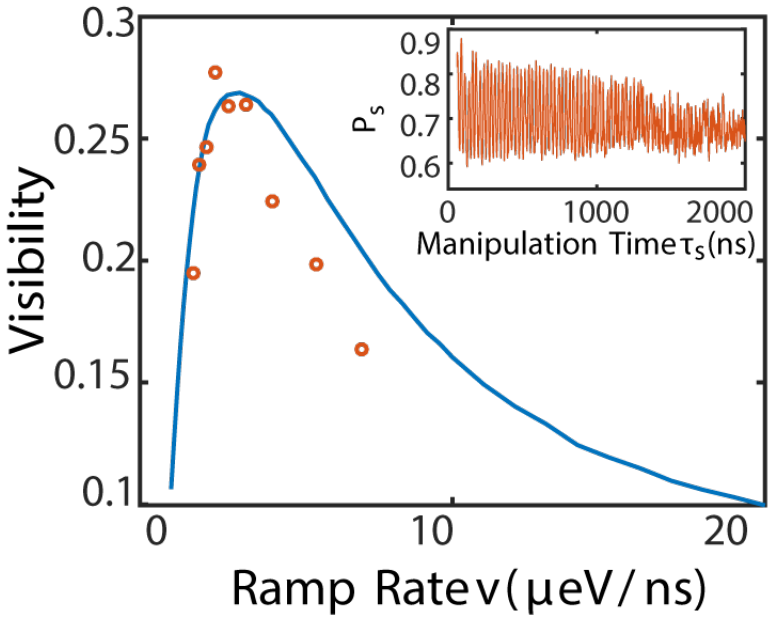

Figure 3-5: (Color online) Visibility of LZS oscillations as a function of ramp rate v, where v is defined as the slope $\mathrm{d}\varepsilon/\mathrm{d}t$ of the initial ramp in the pulse sequence of Fig. 3-4(b). The red dots are experimental data, and the blue line shows the results of theoretical simulations incorporating charge noise with a $\alpha/\omega^{0.7}$ spectrum [69]. No magnetic fluctuations are included in the model. The tunnel coupling at zero detuning used in the calculation is the same as measured in the experiment, $t_{c0} = 3.4$ μeV. The adjustable parameters used to obtain the theoretical results are α, which determines the noise amplitude and yields detuning fluctuations consistent with experimental estimates [46], and h, which describes the transverse magnetic field gradient and determines the optimal ramp rate. The inset shows the experimental return probability P_s measured as a function of manipulation time τ_s.

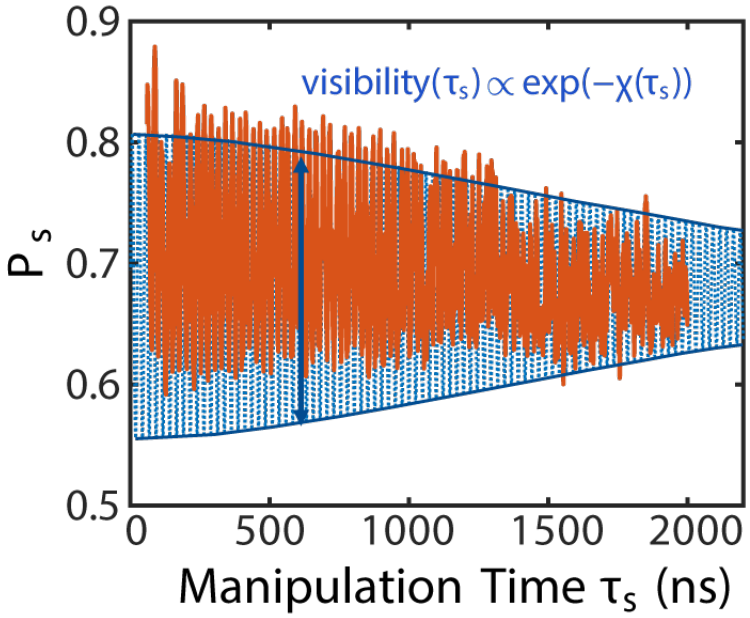

Figure 3-6: (Color online) Return probability P_s measured in the experiment (red solid line) as a function of manipulation time τ_s (this is the same data as the inset of Fig. 3-5). A Gaussian fit to the oscillation envelope yields a decoherence time of ~ 1.7 μs [46]. The maximum visibility, or oscillation amplitude, is about 0.24. The blue dashed line corresponds to our theoretical prediction for the LZS oscillations, obtained using the same parameters as Fig. 3-5 at a ramp rate of $v = 4.4$ μeV/s, which is the same as the experimental ramp rate. The blue solid lines indicate the envelope of the theoretical LZS oscillations, whose amplitude decays as $\exp(-\chi(\tau_s))$, as discussed in the main text.

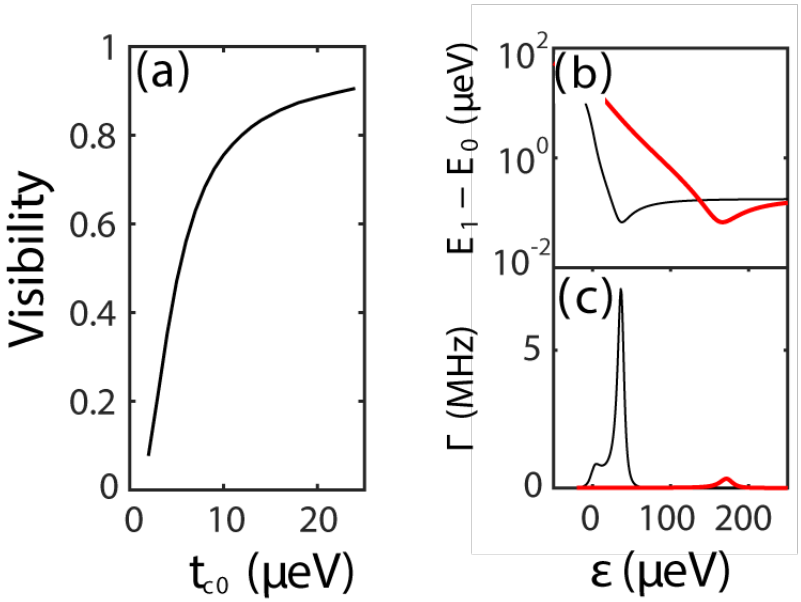

Figure 3-7: (a) Visibility of LZS oscillations at the optimum ramp rate as a function of tunnel coupling t_{c0}. (b) Semilog plot of the energy difference between the ground state $|0\rangle$ and first excited state $|1\rangle$ as a function of detuning; the dips of these curves occur at the magnetic anticrossings. (c) Transition rates Γ as a function of detuning. The thin black lines in (b) and (c) are obtained for the tunnel coupling $t_{c0} = 3.4$ μeV while the thick red lines are obtained for $t_{c0} = 20$ μeV. Increasing the tunnel coupling can be seen to move the magnetic anticrossing farther from the charge anticrossing, causing a decrease in the transition rates.

Chapter 4

Superconducting qubit

4.1 Circuit QED

The interaction between an atom and light is probably one of the most fundamental processes in nature. The difficulty in investigating the effects lies in the fact that the interactin between a single atom and light is usually weak. This difficulty motivated the development of the field of cavity electrodynamics (CQED). The solution is to confine the light in a high-quality cavity such that the light can interact with a single atom many times before it leaks out.

A cavity, in the context of optics, is often an arrangement of mirrors that can bounce light back and forth. Besides a combination of mirrors, it can also manifest as other forms, for example, a coplanar waveguide transmission line in an electric circuit which confines microwave range of electromagnetic wave for a long time before it decays out. Then, to mimic the interaction between an atom and light in cavity QED in a circuit, the remaining part is to find an 'atom'.

When we refer to the word 'atom', what really should come to mind is a discrete-level (quantum-mechanical) system that embeded with a dipolar coupling with electromagnetic wave. A capacitor with different number of charges on its two sides can acts as an electric dipole, and a combination of a capacitor and an inductor forms a electromagnetic harmonic oscillator that has discrete energy levels. However, a harmonic oscillator has equally-spaced energy levels, which differs from an atom. This

difference is crucial because it is the unique frequency of a transition in an atom that generates the Rabi oscillation: a process of energy absorbed in and given out periodically. Introducing non-linearity to the oscillator should be one solution, and in fact, it is now a standard solution. The non-linearity is introduced by Josephson junctions, which can be modeled as a nonlinear inductance shunted by a linear capacitor.

By incorporating the Josephson element as an artificial atom in an electric circuit, similar effects of the interaction between an atom and light can be observed and described using the language of CQED. To further analyze a circuit with more complex geometry and topology and more electric capactive and inductive elements in a regime that quantum effects dorminant, it is necessary to quantize the circuit.

A more detailed introduction of the quantization of a circuit can be found in Ref. 76. More systematically, this can be done in the language of graph theory, which can be found in Ref. 77. Here, we list a simple version of recipe to quantize a circuit:

- Write down the equation of motion of the circuit. Usually node flux is used as the variable for convenience and it has the role of position in mechanical system.
- Based on the equation of motion, write down the Langrangian of the circuit and find the conjugate momentum, which turns out to be the charge, of the node flux.
- Imposing commutation relation between flux and charge so that these two quantity are 'upgraded' as operators.
- Write down the Hamiltonian of the system in terms of flux operator and charge operator.

4.1.1 Two-qubit gates

With the a chosen superconducting qubit, no matter it is a charge qubit, phase qubit or a transmon, the dipolar coupling between this artificial atom and the electromagnetic field will provides a natural way to coherently manipulate the qubit state by controlling the corresponding field, i.e., single qubit gates should be well within reach

once a good superconducting qubit is built. In fact, high-fidelity single qubit gates have been experimentally realized quite a long time ago[78]. Therefore, we will skip the discussion on single-qubit gates and jump right into two-qubit gates for superconducting qubit in this dissertation.

One approach for two qubit gates was proposed for frequency tunable qubits by Strauch et al. [79]. This approach was demonstrated for transmon-like qubits [80–82] and more recently for gatemons [83].

However, our final goal is to build a scalable quantum computer. As the number of qubits increases, their energy spectrum becomes very dense, making two-qubit gates based on frequency tuning a hardly scalable solution. Another approach is to use microwave drive or SFQ pulse sequence, which we'll discuss in more detail in Chapter 5. This approach also assumed fixed-coupling between neighboring qubits, which inevitably introduce crosstalk. In the sense of scalability, a preferable approach that can evade both frequency crowding and crosstalk would be to use tunable couplers between qubit pairs. And this will be the focus of the rest of this chapter.

The idea of a CZ gate using a tunable coupler is quite natural and straightforward. The standard CZ gate takes the form of $\mathrm{diag}\{1, 1, 1, -1\}$. When drive is absent, the interacting two qubits evolve freely under the Hamiltonian H_t, giving an evolution operator of the following form

$$W(t) = \mathrm{diag}\{e^{-i\phi_{00}}; e^{-i\phi_{01}}; e^{-i\phi_{10}}; e^{-i\phi_{11}}\}, \tag{4.1a}$$

$$\phi_m(t) = \tilde{E}_m t/\hbar. \tag{4.1b}$$

The interaction provides a non-zero value for the CZ gate rate[Book:QCnQI2000, Strauch2003]

$$\zeta_0 = (\tilde{E}_{11} + \tilde{E}_{00} - \tilde{E}_{01} - \tilde{E}_{10})/\hbar, \tag{4.2}$$

so that after time $t = \pi/|\zeta_0|$, the evolution operator is equivalent to the ideal CZ gate $U_{\mathrm{CZ}} = \mathrm{diag}\{1; 1; 1; -1\}$ with the phase shifts $\phi_{10} - \phi_{00}$ and $\phi_{01} - \phi_{00}$ to be factored out by single qubit Z gates U_{z1} and U_{z2}[Ghosh2013].

4.2 Superconducting qubit designs: transmon

For a single Josephson junction, the above quantization process can be done in a much simpler way given the Josephson effects. Here instead using the charging operator $\hat{Q}$ and flux operator $\hat{\Phi}$, we use two dimensionless quantities, which are the cooper pair number difference N and phase operator δ for convenience. The DC Josephson effect says

$$I_J = -2e\frac{dN}{dt} = I_0 \sin\delta, \tag{4.3}$$

where I_J is the current through the junction and I_0 the junction critical current, which is the maximum current that allows the metal to remain in its superconducting phase. And the AC Josephson effect is

$$\frac{d\delta}{dt} = \frac{2eV}{\hbar} = \frac{4e^2N}{\hbar C}, \tag{4.4}$$

Then we can write the above equation in the form of Hamilton's equations as follows

$$\begin{aligned} \frac{dN}{dt} &= -\frac{I_0}{2e}\sin\delta = -\frac{1}{\hbar}\frac{\partial H}{\partial \delta} \\ \frac{d\delta}{dt} &= \frac{4e^2N}{\hbar C} = \frac{1}{\hbar}\frac{\partial H}{\partial N} \end{aligned} \tag{4.5}$$

From the above two equations, one can infer the form of Hamiltonian for the Josephson junction:

$$H = E_C N^2 - E_J \cos\delta \quad ; \quad E_C = \frac{2e^2}{C} \quad , \quad E_J = \frac{\hbar I_0}{2e} \tag{4.6}$$

It is obvious that the above Hamiltonian differs from that of a harmonic oscillator. It resembles one only when we take up to the second order of δ for the second term. In numerical modeling, one can still represent the Hamiltonian in Harmonic oscillator basis and treat the higher order terms in δ as perturbation terms. Then instead of charge and flux operators, one can move to the frame of linear combinations of them such that the new operators bear the physical meaning of creator/annihilator of the oscillation mode in the Harmonic oscillator basis.

The states of this anharmonic oscillator can be written in either phase represen-

tation or charge representation. In terms of which representation is better, we need to figure out which quantity is a good quantum number. The answer depends on the relative magnitude of E_C and E_J. Here we list two limiting cases:

- $E_C \ll E_J$: the fluctuation of phase operator δ is small, thus it is well defined while the cooper pair number is fuzzy.

- $E_C \gg E_J$: the fluctuation of phase operator is large while the cooper pair number difference across the Josephson junction is well defined.

When we use this anharmonic oscillator as a qubit, or more precisely, we use the lowest two energy levels as a qubit[1], correspondingly the qubit state can be defined in phase representation or charge representation. When the system is in the regime where the phase (charge number) is well defined, the eigenstates of the qubit, out of which we define state $\left|0\right\rangle$ and $\left|1\right\rangle$, can be identified by their phase (charge number), therefore it is called a phase (charge) qubit.

4.2.1 Transmon

Besides charge qubit and phase qubit for the above two limiting cases, one can also choose the regime between the two. By taking the advantage of the fact that the charge dispersion reduces exponentially in E_J/E_C, while the anharmonicity only decreases algebraically with a slow power law in E_J/E_C[84], a new type of qubit called transmon, is introduced in [85] and is now becoming one of the favorite superconducting qubits[80, 86–88].

A schematic device design and corresponding circuit diagram is shown in Fig. 4-1. It can be proved [85] that the Hamiltonian of a transmon can be written in the same form as that of a cooper pair box:

$$\hat{H} = 4E_C \left(\hat{n} - n_g\right)^2 - E_J \cos\hat{\varphi}, \tag{4.7}$$

[1] A qubit does not necessarily to be defined in the subspace that consists of two energy eigenstates.

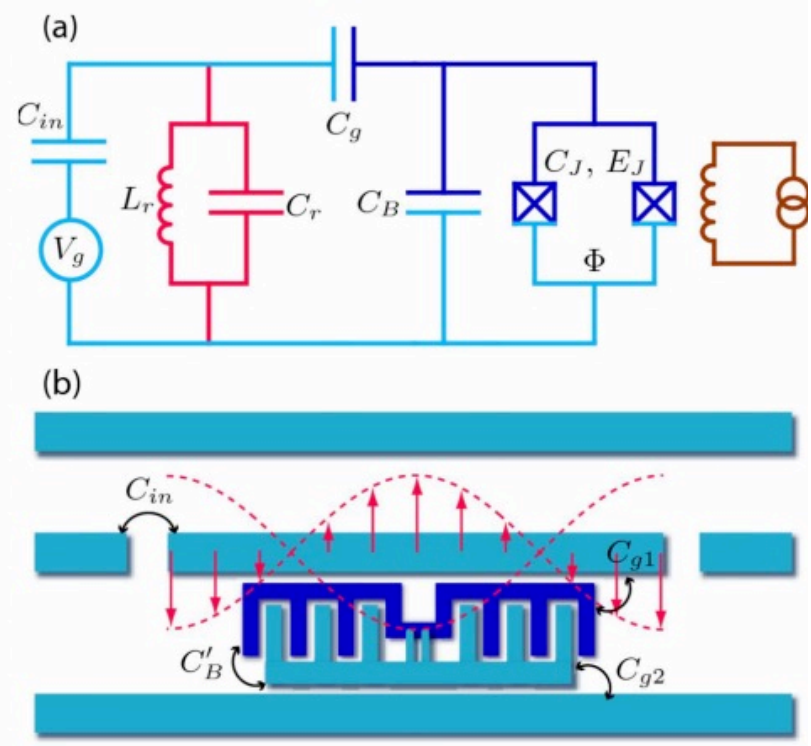

Figure 4-1: (a)Effective circuit diagram of the transmon qubit and (b) simplified schematic of the transmon device design (not to scale). Reproduced from Ref. [85].

where we use charge number operator $\hat{n} = 1/2\hat{N}$ instead of cooper pair number, but the physics remains the same.

For anharmonic oscillators, harmonic basis (also called LC basis) is usually used in numerical simulations. The anharmonicity can then be treated as perturbations. However, this approximation is not necessary for transmon. Since the static Schrödinger equation

$$\left[4E_C\left(-i\frac{d}{d\varphi}-n_g\right)^2-E_J\cos\varphi\right]\psi(\varphi)=E\psi(\varphi) \tag{4.8}$$

does have analytical solutions, which are Mathieu's functions[84, 85, 89] in the following form

$$\psi_m(\varphi)=\frac{\exp\left(in_g\varphi\right)}{\sqrt{2}}me_{-2[n_g-k(m,n_g)]}\left(-\frac{E_J}{2E_C},\frac{\varphi}{2}\right) \tag{4.9}$$

where

$$\begin{aligned}k\left(m,n_g\right)=&\sum_{\ell=\pm1}\left[\text{int}\left(2n_g+\ell/2\right)\bmod 2\right]\\&\times\left\{\text{int}\left(n_g\right)+\ell(-1)^m[(m+1)\,\text{div}\,2]\right\}\end{aligned} \tag{4.10}$$

and the eigenvalues are

$$E_m\left(n_g\right)=E_Ca_{2[n_g+k(m,n_g)]}\left(-E_J/2E_C\right), \tag{4.11}$$

where $a_\nu(q)$ denotes Mathieu's characteristic values. Depending on the accuracy of a certain calculation, one can choose either to use the LC basis or Mathieu's basis to represent the operators in numerical calculations. In the following sections of this chapter, transmons are modeled in the LC basis since we only need to accurately model the lowest several levels. However, in Chapter 6, the analytical solution is used since we are in the regime where higher levels might come into play and affect the dynamics of a readout process.

4.3 Two-qubit gates with semiconductor junction

A spectacular solution to scaling up system was found in conventional classical computers where successful simultaneous control of over a trillion transistors comes from

the marvels of semiconductors. The transistor is the key element of this technology as it can switch on and off conductivity of a nanoscale region of a semiconductor chip by applying local nanosecond-scale voltage pulses. It is therefore tempting to explore an approach where highly-scalable gate-control of semiconductors can be incorporated into superconducting devices. A nanowire-based gatemon is a transmon whose tunnel Josephson junction is replaced with a hybrid super/semi–conductor junction. This junction can be formed by InAs nanowires in epitaxial contact with Al leads [83, 90–95]. The Josephson energy E_J of such junctions is tuned by a side electric gate that controls the transmission of conducting channels in the semiconductor. The ability to tune the Josephson energy introduces Z gates for single qubit operations [83], permits additional reconfigurability of multiqubit systems to address frequency crowding and brings options for scaling quantum processor to a large number of qubits, by analogy with the operation of conventional transistor of classical processors.

Inspired by this idea, we propose a realization of a controlled–Z gate achieved by an electrically tuned semiconductor junction connecting two transmon qubits, see Fig. 4-2 for an illustration. This approach is similar to the two qubit gates in g-mon systems [96, 97], but in our case, the inductive coupling is controlled by the transparency of a semiconductor junction connecting two superconducting qubits.

We assume that the connector can be completely closed by a proper negative voltage applied to a nearby gate. When the gate voltage is removed, an Andreev bound state (ABS) forms in the connector and its energy depends on the difference in phases of superconducting order parameters on the transmon superconducting islands. When the coupling between transmons through the junction is turned on, the additional Josephson energy associated with the ABS introduces effective interaction between two qubits and changes energy spectrum of the two qubit system. This change allows one to perform a controlled–Z gate (CZ), similar to frequency-tunable CZ gates [79]. The great advantage of this electro-statically controlled gate is that the interaction between the qubits can be turned off and thus completely decouple qubits. At the same time, the interaction can reach strong magnitude during the two-qubit gate operation necessary for a realization of fast high-fidelity CZ gates.

Since the semiconductor junction is turned off during single qubit operations, we do not expect that these junctions will degrade significantly coherent properties of the qubit system.

In this chapter, we have specifically discussed three qubit configurations:

Transmon [Fig. 4-2(a)] is current favorite among superconducting qubits due to its reduction in sensitivity to charge noise relative to the Cooper pair box and increase in the qubit-photon coupling [80, 85–88]. We analyze the CZ gate characteristics for two transmons coupled by an electrically-controlled epitaxial semiconductor junction. This configuration will take advantage of coherence of conventional Al/AlO_x/Al transmons and electrically tunable interaction between them, see Sec. 4.3.1.

Gatemon [Fig. 4-2(b)] is a form of transmon, where the tunnel junction is replaced by a semiconductor Josephson junction [83, 91–95]. The configuration of two gatemons coupled by a semiconductor junction has a benefit as this system has all-semiconductor system without AlO_x tunnel junctions. However, always "on" semiconductor Josephson junction of a gatemon may reduce coherence of the individual qubits. We discussed this configuration in Sec. 4.3.2.

H-pair [Fig. 4-2(c)] is a system of two gatemon-like qubits with their Josephson junctions combined into a single H-shaped four-terminal junction which is lithographically patterned as epitaxial super/semi Josephson junctions [93]. The H-pair may simplify the fabrication process of coupled qubits. This junction also shows interesting physical structure of the Andreev bound states and was a focus of recent theoretical studies [90, 98–102]. We describe properties of an H-pair in Sec. 4.3.3.

We demonstrate that the proposed CZ gate realization for all three configurations can reach fidelity above 99.99% for 50 ns gate time.

4.3.1 Two coupled transmons

We consider two transmon qubits coupled by a semiconductor junction. When the junction is open, the transmons are decoupled. Each transmon is characterized by the charging, $E_{C,\alpha}$, and Josephson, $E_{J,\alpha}$, energies, where $\alpha = 1, 2$. To suppress effects of charge noise on qubit, transmon capacitances C_α are chosen large and the charging

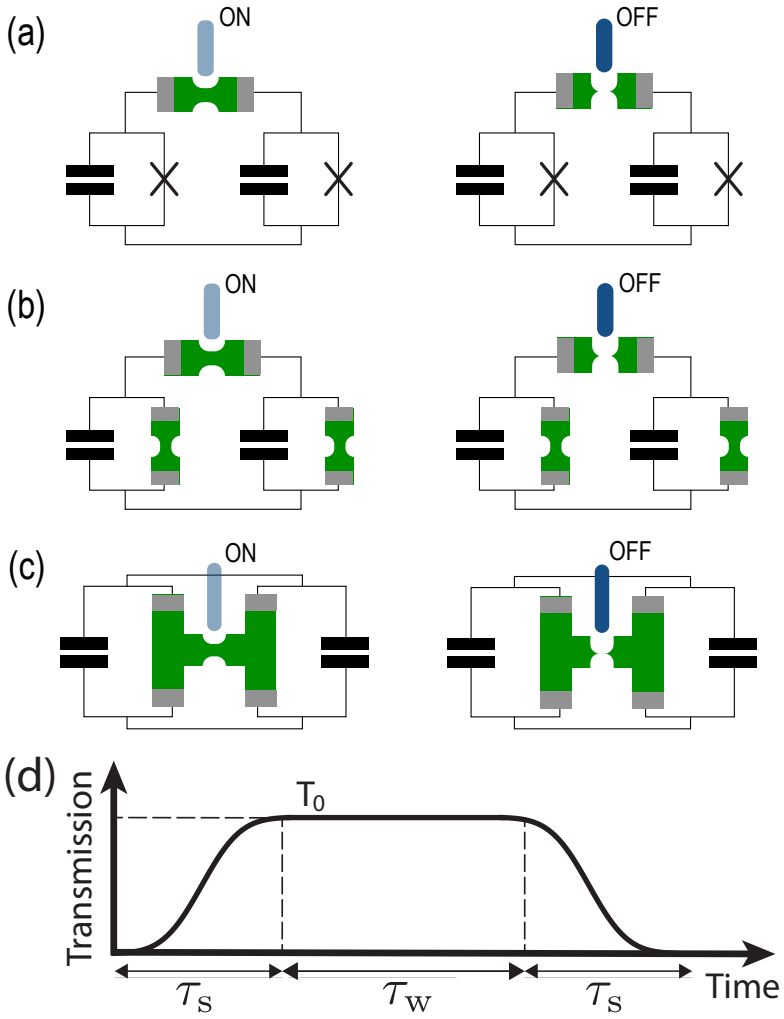

Figure 4-2: A schematic picture of two qubits connected by an epitaxial semiconductor junction (green bar). The three configurations presented here are: (a) two transmons formed by tunnel Josephson junctions, (b) two gatemons, where the Josephson elements are formed by other epitaxial semiconductor junctions, (c) two gatemon-like qubits, where their Josephson junction are combined into an H-shaped four-terminal epitaxial junction. The voltage on the gate (vertical bar) switches connection between two qubits on (left column) and off (right column). (d) The connector transmission T_c as a function of time. The transmission changes according to Eqs. (4.23) during time τ_s for switching on and off and is maintained at constant value T_0 during waiting time τ_w.

energy $E_{C\alpha} = e^2/2C_\alpha$ are much smaller than the Josephson energy, $E_{C\alpha} \ll E_{J\alpha}$. The Hamiltonian of a transmon contains both charging and Josephson energies [85] and can be written in the form

$$H_\alpha^{(0)} = 4E_{C,\alpha}\hat{n}_\alpha^2 + E_{J,\alpha}\left(\frac{\hat{\theta}_\alpha^2}{2} - \frac{\hat{\theta}_\alpha^4}{24}\right). \tag{4.12}$$

Here, the electron number operator, $\hat{n}_\alpha$, and the superconducting order parameter phase operator, $\hat{\theta}_\alpha$, do not commute, $[\hat{n}_\alpha, \hat{\theta}_\alpha] = i$. The energy spectrum of the three lowest energy states of a transmon is characterized by the transition frequency ω_{10} between the ground and first excited states and the anharmonicity β:

$$\hbar\omega_{10}^{(\alpha)} = E_1^{(\alpha)} - E_0^{(\alpha)}, \tag{4.13}$$

$$\hbar\beta^{(\alpha)} = E_2^{(\alpha)} - E_1^{(\alpha)} - \hbar\omega_{10}^{(\alpha)}. \tag{4.14}$$

These parameters are approximately given by the following expressions in terms of the Josephson and charging energies[85]:

$$\hbar\omega_{10}^{(\alpha)} \approx \sqrt{8E_{J,\alpha}E_{C,\alpha}} - E_{C,\alpha}, \quad \beta^{(\alpha)} \approx E_{C,\alpha}/\hbar. \tag{4.15}$$

While the condition $E_{J,\alpha} \gg E_{C,\alpha}$ is necessary to reduce transmon sensitivity to charge noise, this same condition results in weak anharmonicity of transmons and imposes certain constraints on time dependence of control pulses, including the CZ gate.

In the discussion below, we assume that the Josephson energies of both transmons are equal, $E_{J,\alpha} = E_J$, but the charging energies $E_{C,\alpha}$ are different to provide distinguishable frequencies $\omega_{10}^{(\alpha)}$ by about 3%, which requires $E_{C1}/E_{C2} \simeq 0.94$. In particular, we take

$$\frac{E_J}{h} = 20.55 \text{ GHz}, \frac{E_{C,1}}{h} = 240 \text{ MHz}, \frac{E_{C,2}}{h} = 255 \text{ MHz}. \tag{4.16}$$

The qubit energies and anharmonicities for this choice of qubit parameters are presented in Table 4.1. The energy spectrum of two non-interacting qubits is such that

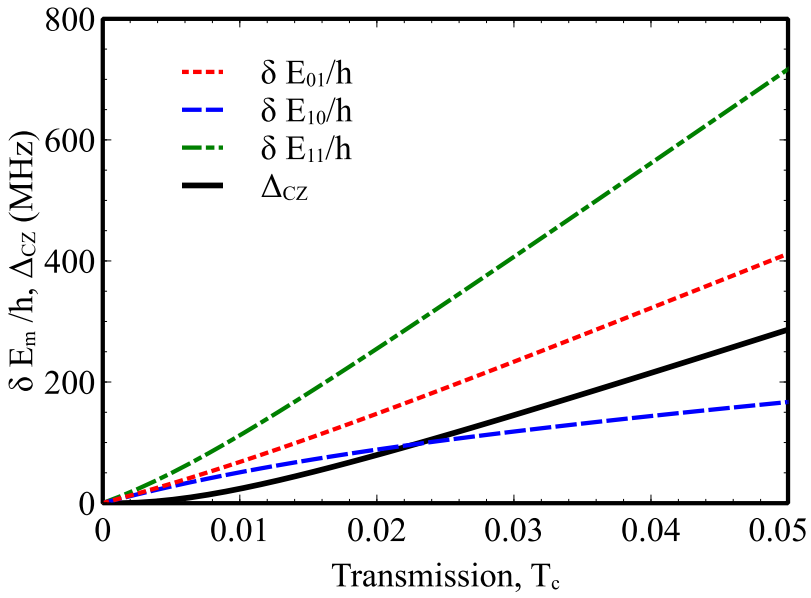

Figure 4-3: (Color online) Energy shifts on eigenenergies, $\delta E_m = \tilde{E}_m - E_m$, of the two-qubit systems as a function of transmission T_c. Only three out of four states in computational subspace are depicted. For both qubits, the Josephson energy $E_J/h =$ 20.55 GHz, and the charging energies $E_{C1}/h = 240$ MHz and $E_{C2}/h = 255$ MHz.

computational state $|11\rangle$ is above both non-computational states $|20\rangle$ and $|02\rangle$. This order of energy states happens when the frequency separation between two qubits is smaller than the qubit anharmonicities. A counter example is considered in Sec. III for the case of two gatemons, where the anharmonicity is reduced and the computational state $|11\rangle$ is between states $|20\rangle$ and $|02\rangle$.

When the connecting junction acquires non-zero transmission T_c, the interaction energy between the transmons is given by the energy of the Andreev bound state

	Transmon, GHz	Gatemon, GHz	H-junction, GHz
$\omega_{10}^{(1)}/h$	6.02	6.22	6.17
$\omega_{10}^{(2)}/h$	6.20	6.41	6.36
$\beta^{(1)}/2\pi$	-0.294	-0.063	-0.066
$\beta^{(2)}/2\pi$	-0.315	-0.067	-0.070

Table 4.1: Eigenenergies for non–interacting ($T_c = 0$) two transmons, two gatemons and H-junction qubit systems. The Josephson energy $E_J/h = 20.55$ GHz for both transmon and gatemon qubits and $E_J/h = 20.24$ GHz for H-junction qubits, the charging energy for qubit one $E_{C1}/h = 240$ MHz and qubit two $E_{C2}/h = 255$ MHz. All the eigenenergies are written in reference to the ground state energy.

(ABS)[103]

$$\delta E_{\rm ABS} = \Delta\sqrt{1 - T_c \sin^2\left(\frac{\hat{\theta}_1 - \hat{\theta}_2}{2}\right)}, \tag{4.17}$$

where $\hat{\theta}_{1,2}$ are superconducting phases of the transmons and Δ is the superconducting energy gap. Assuming that the phase fluctuations of both transmons are small, $\theta_{1,2} \ll 1$, we expand Eq. (4.17) to quartic terms in the qubit phases:

$$V_{\rm int} \simeq \frac{T_c\Delta}{8}\left((\hat{\theta}_1 - \hat{\theta}_2)^2 - \frac{1}{12}(\hat{\theta}_1 - \hat{\theta}_2)^4\right). \tag{4.18}$$

Here we consider small transmission coefficient $T_c \ll 1$ of the connecting junction, sufficient for high-fidelity CZ gate. This interaction modifies the instantaneous eigenstates $\widetilde{|m\rangle}$ and energies $\tilde{E}_m$ of the full system Hamiltonian

$$H = H_1 + H_2 + V_{\rm int}. \tag{4.19}$$

As the transmission coefficient T_c increases, the distance between neighboring energy states increases as a consequence of energy level repulsion.

Below, we identify states $\widetilde{|m\rangle}$ by their adiabatic evolution as a function of T_c from the non-interacting case, $T_c = 0$, *i.e.* index m is composed of two integers $m \to (n_1, n_2)$, representing n_αth excited state of non-interacting transmon $\alpha = 1, 2$. We evaluate the relative energy shifts $\delta\tilde{E}_m = \tilde{E}_m - E^{(1)}_{n_1} - E^{(2)}_{n_2}$ of computational subspace eigenstates, $m = \{00; 01; 10; 11\}$ as a function of transmission coefficient T_c, represented in Fig. 4-3.

The evolution operator in the computational subspace in the eigenstate basis $\widetilde{|m\rangle}$ has the form

$$W(t) = \mathrm{diag}\{e^{-i\phi_{00}}; e^{-i\phi_{01}}; e^{-i\phi_{10}}; e^{-i\phi_{11}}\}, \tag{4.20a}$$

$$\phi_m(t) = \tilde{E}_m t/\hbar. \tag{4.20b}$$

The interaction provides a non-zero value for the CZ gate rate[79, 104, 105]

$$\Delta_{\mathrm{CZ}} = (\tilde{E}_{11} + \tilde{E}_{00} - \tilde{E}_{01} - \tilde{E}_{10})/h, \tag{4.21}$$

so that after time $t = 1/(2\,|\Delta_{\mathrm{CZ}}|)$, the evolution operator is equivalent to the ideal CZ gate $U_{\mathrm{CZ}} = \mathrm{diag}\{1; 1; 1; -1\}$ with the phase shifts $\phi_{10} - \phi_{00}$ and $\phi_{01} - \phi_{00}$ to be compensated by single qubit Z gates U_{z1} and U_{z2}. The dependence of Δ_{CZ} on T_c is shown in Fig. 4-3 by a solid thick line. We demonstrate below that the energy shift Δ_{CZ} is sufficient for performing gate operation over time of $(2\,|\Delta_{\mathrm{CZ}}|)^{-1} \lesssim 50\mathrm{ns}$.

With tunable coupler between two qubits, CZ gate can be realized by simply switching interaction on over time τ_s, waiting time $\tau_w \approx 1/(2\,|\Delta_{\mathrm{CZ}}|)$ and switching interaction off over time τ_s. The total gate time is

$$\tau_g = 2\tau_s + \tau_w. \tag{4.22}$$

First, we analyze the phase accumulation and transition probabilities during switching processes. In particular, we demonstrate that the relatively small separation of the computational state $\widetilde{|11\rangle}$ from the leakage states $\widetilde{|20\rangle}$ and $\widetilde{|02\rangle}$ results in non-negligible leakage of the system state from the computational subspace due to transitions during switching on and off. Then, we describe the overall gate performance that combines the evolution of the system during switching on and off processes and waiting for τ_w at fixed T_c.

Switching interaction on/off

We now consider the process of switching on and off interaction between the transmon qubits which is realized by electrically changing the transparency of the connector by tuning the voltage on the gate. Specifically, we assume that the connector transmis-

sion $T_c(t)$ during the switching on and off processes is

$$T_c^{(\mathrm{on})}(t) = T_0 \frac{\mathrm{erf}(4t/\tau_s - 2) + 1}{2}, \tag{4.23a}$$

$$T_c^{(\mathrm{off})}(t) = T_c^{(\mathrm{on})}(\tau_s - t). \tag{4.23b}$$

During the switching on and off of the interaction between qubits, care is needed to avoid transitions from $\big|11\big\rangle$ state to double excited states $\big|20\big\rangle$ and $\big|02\big\rangle$, as well as transitions between states $\big|01\big\rangle$ and $\big|10\big\rangle$. We take τ_s to be longer than the inverse anharmonicities $1/\beta^{(1,2)}$ or qubits detuning, $1/|\omega_{10}^{(1)} - \omega_{10}^{(2)}|$ to suppress these transitions.

The evolution operator of the two-qubit system during the switching of interaction is a solution to the Schrodinger equation

$$i\hbar\partial_t U(t) = H(t)U(t), \tag{4.24a}$$

$$H(t) = \sum_{\alpha=1,2} H_\alpha^{(0)} + V_{\mathrm{int}}(t), \tag{4.24b}$$

where the interaction $V_{\mathrm{int}}(t)$, see Eq. (4.18), changes in time in response to the changing connector transmission $T_c(t)$. The evolution operators $U_{\mathrm{on/off}}(\tau_s)$ at the end of switching on and off processes are used below to compose the evolution operator for the whole gate and to evaluate the gate fidelity.

In particular, the operators $U_{\mathrm{on}}(\tau_s)$ define the phase shifts $\varphi_m^{(\mathrm{on})}$ of instantaneous eigenstates $\widetilde{\big|m\big\rangle}$ of the full Hamiltonian $H(t)$ that are utilized later to work out timing for the full CZ gate. We numerically evaluate $U_{\mathrm{on/off}}(\tau_s)$ by solving Eq. (4.24a) in a 10×10 Hilbert space in the basis of a harmonic oscillator wave functions and make sure that the low energy states are evaluated accurately for the actual Hamiltonian $H(t)$ of the system, Eq. (4.24b). Then, we analyze the 4×4 matrix $[U_{\mathrm{on}}^{(\mathcal{Q}_2)}]_{mm'} = \widetilde{\big\langle m\big|}U_{\mathrm{on}}(\tau_s)\big|m'\big\rangle$ in the computational subspace $\mathcal{Q}_2$ of two qubits. Matrix $[U_{\mathrm{on}}^{(\mathcal{Q}_2)}]_{mn}$ defines the evolution of a state from the non-interacting computational subspace, $T_c = 0$, to a final state, projected to the dressed computational subspace at $T_c = T_0$, where $m, n = \{00, 01, 10, 11\}$. The diagonal elements of this matrix determine

the phase factor accumulated by state $\widetilde{|m\rangle}$ during the switching process, $\varphi_m^{(\mathrm{on})} = \arg\{[U_{\mathrm{on}}^{(\mathcal{Q}_2)}]_{mm}\}$. We obtain the relative phase difference relevant for the CZ gate

$$\delta\Phi_{\mathrm{CZ}}^{(\mathrm{on})} = \varphi_{11}^{(\mathrm{on})} + \varphi_{00}^{(\mathrm{on})} - (\varphi_{10}^{(\mathrm{on})} + \varphi_{01}^{(\mathrm{on})}), \tag{4.25}$$

which we utilize $\delta\Phi_{\mathrm{CZ}}^{(\mathrm{on})}$ in the next subsection to evaluate the full gate time.

In the rest of this subsection, we evaluate the probabilities of transitions between pairs of instantaneous eigenstates since these transitions reduce the gate fidelity. We compute $[U_{\mathrm{on}}^{(\mathcal{Q}_2)}]_{mn}$ and determine the probability of transition $P_{m,n} = |\widetilde{\langle m|}U(\tau_s)|n\rangle|^2$ for a system of two transmons from state $|n\rangle$ to state $\widetilde{|m\rangle}$. The result of this calculation is shown in Fig. 4-4 by dashed and dotted lines for the transitions from state $\widetilde{|11\rangle}$ to its neighboring states $\widetilde{|02\rangle}$ and $\widetilde{|20\rangle}$. The probability of transitions between pairs of energy states decreases fast as the energy difference increases. For the energy spectrum of the two transmons analyzed here, the dominant leakage happens from $\widetilde{|11\rangle}$ to $\widetilde{|02\rangle}$. The transition probabilities also decrease fast as the switching time τ_s increases and drop below 10^{-3} for $\tau_s \gtrsim 20$ns.

To better understand the transition probabilities between the states during the switching on and off processes, we perform the perturbation theory analysis following Ref. 105. In our case the bare level spacing is fixed and the interaction strength changes in time, while in Ref. 105 the interaction was fixed and individual qubit spectrum was changing. Denoting a dressed state of interest by $\widetilde{|m(t)\rangle}$, we can write $\widetilde{|m(t)\rangle} = \sum_n C_n(t)\exp(i\vartheta_n(t))\widetilde{|n(t)\rangle}$, where $\vartheta_n(t) = -\int_0^t \tilde{E}_n(t')\,\mathrm{d}t'/\hbar$ and $\tilde{E}_n(t)$ is an eigenenergy of instantaneous eigenstate $\widetilde{|n(t)\rangle}$ at time t. The coefficients $C_n(t)$ are obtained as solutions to the Schrödinger equation

$$\begin{aligned}\dot{C}_m(t) = &- C_m(0)\widetilde{\langle m(t)|}\left[\frac{\partial}{\partial t}\widetilde{|m(t)\rangle}\right] \\ &- \sum_n C_n(t)e^{i(\vartheta_n-\vartheta_m)}\frac{\widetilde{\langle m(t)|}\dot{H}(t)\widetilde{|n(t)\rangle}}{\tilde{E}_n(t)-\tilde{E}_m(t)},\end{aligned} \tag{4.26}$$

where $H(t)$ is the time-dependent Hamiltonian (4.24b) of the system.

Here we only provide perturbative analysis for the leakage from $|11\rangle$ and $\widetilde{|02\rangle}$, as

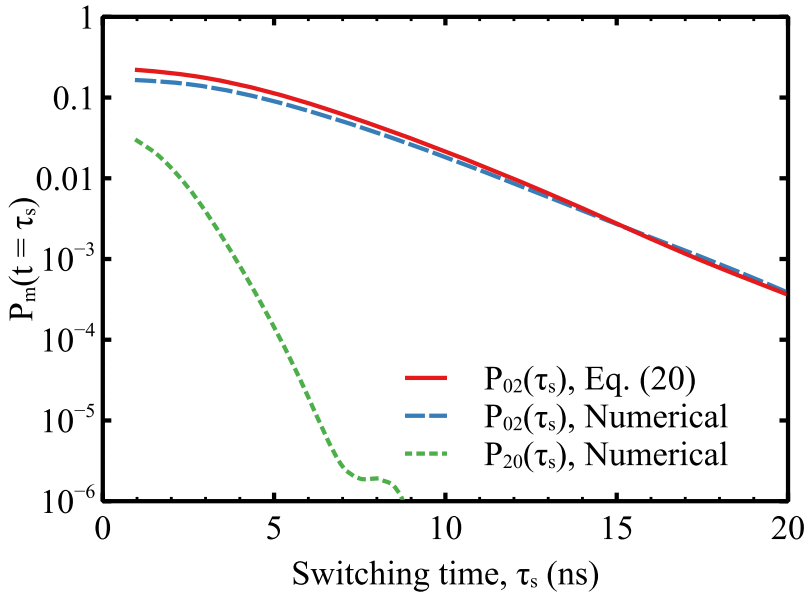

Figure 4-4: Leakage probability from state $|11\rangle$ to $|02\rangle$ and $|20\rangle$ during the switching on of transmission T_c of a junction connecting two transmons as a function of switching time τ_s for the final transmission $T_0 = 0.015$. This leakage implies the worst case of gate performance since the transition from $|11\rangle$ to $|02\rangle$ is the dominant undesired transition.

these two states have the closest energy separation. Other pairs of neighboring states can be evaluated using the expressions obtained below with corresponding values for the instantaneous energy states and matrix elements of the interaction. The resulting transition probability from the initial state can be taken as the sum of probabilities of transitions to nearby states, provided that all these probabilities are small. We reduce our problem to the analysis of a two-level system formed by states $|11\rangle$ and $|02\rangle$:

$$H_{2L}(t) = \begin{pmatrix} E_{11}(t) & J(t) \\ J(t) & E_{02}(t) \end{pmatrix}. \tag{4.27}$$

The time derivative of H_{2L} is given by that of transmission T_c, which in general results in the time-dependence of the energies $E_{11/02}(t)$ and the interaction $J(t)$.

Starting from initial state $|11\rangle$, we take $C_{11}(t = 0) = 1$ and assume that the $C_{11}(t) \approx 1$ throughout the switching process. The equation for $C_{02}(t)$ takes the form

$$\dot{C}_{02}(t) = -e^{i\chi(t)}\mathcal{M}(t). \tag{4.28}$$

Here

$$\chi(t) = \int_0^t \sqrt{(E_{11}(t') - E_{02}(t'))^2 + 4J^2(t')}\, \mathrm{d}t' \tag{4.29}$$

and the matrix element of the time-derivative of the Hamiltonian can be cast in the form

$$\begin{aligned} \mathcal{M}(t) &= \frac{\widetilde{\langle 02(t)|}\dot{H}(t)\widetilde{|11(t)\rangle}}{\tilde{E}_{11}(t) - \tilde{E}_{02}(t)} \\ &= \frac{\dot{J}(t)(E_{11}(t) - E_{02}(t)) - (\dot{E}_{11}(t) - \dot{E}_{02}(t))J(t)}{(E_{11}(t) - E_{02}(t))^2 + 4J^2(t)}. \end{aligned} \tag{4.30}$$

The transition probability $P_{02}(t)$ after time t is determined by the integration of Eq. (4.28) over time with the initial condition $C_{02}(t=0) = 0$:

$$C_{02}(t) = \int_0^t \dot{C}_{02}(t')dt', \quad P_{02}(t) = |C_{02}(t)|^2. \tag{4.31}$$

The perturbative analysis of the transition probability from $|11\rangle$ to $\widetilde{|02\rangle}$ is then accomplished by a numerical integration of Eq. (4.28). The result is shown in Fig. 4-4. Solid line in Fig. 4-4 represents $P_{02}(\tau_s)$ at the end of the switching on the connector transmission to $T_0 = 0.015$ during time τ_s. Estimate (4.31) captures the main features of the full numerical solution, to improve quantitative agreement between the curves, we would have to expand the above analysis to include multiple energy states into account. The structure of Eq. (4.31) reveals that the suppression of $P_{02}(\tau_s)$ as a function of switching time is due to the fast oscillating factor $\exp(i\chi(t))$ in Eq. (4.28) for $\dot{C}_{02}(t)$, while $\mathcal{M}(t)$ is a smooth function of time.

Controlled–Z gate

Now we analyze the dynamics of quantum states when the connector transmission is fixed, $T_c = T_0$, during time τ_w. The phase difference combination for the CZ gate is given by $2\pi\Delta_{\mathrm{CZ}}\tau_w$ and the waiting time τ_w is found from the condition

$$\frac{2\delta\Phi_{\mathrm{CZ}}^{\mathrm{on}}}{2\pi} + \Delta_{\mathrm{CZ}}\tau_w = \frac{1}{2}, \tag{4.32}$$

where the phase difference $\delta\Phi_{\mathrm{CZ}}^{\mathrm{on}}$ was introduced in Sec. 4.3.1. To evaluate fidelity of the full gate, we numerically calculate the evolution operator U for the process that is described by switching on transmission of the connector in the form of Eq. (4.23), maintaining $T_c(t) = T_0$ for waiting time τ_w and switching off T_c as a time-reversed process as illustrated in Fig. 4-2(d).

For numerical evaluations, the corresponding evolution operator $U = U_{\mathrm{off}} U_w(\tau_w) U_{\mathrm{on}}$ is defined as the product of evolution operators U_{off} and U_{on}, discussed in Sec. 4.3.1 and the evolution operator $U_w(\tau_w) = \exp(-iH_w\tau_w/\hbar)$, where H_w is the Hamiltonian in Eq. (4.19) with $T_c = T_0$. Then, the fidelity is calculated by comparing matrix $[\hat{W}]_{nm} = \langle n|U|m\rangle$ in computational 2×2 subspace, $n, m = \{00, 01, 10, 11\}$, to the ideal CZ gate, U_{CZ}, using the following expression for the fidelity [106]:

$$F = \frac{1}{20}\left[\mathrm{Tr}\left(\hat{W}\hat{W}^{\dagger}\right) + \left|\mathrm{Tr}\left(\hat{U}_{z1}\hat{U}_{z2}\hat{W}\hat{U}_{\mathrm{CZ}}\right)\right|^2\right], \tag{4.33}$$

where $\hat{U}_{z1}$ and $\hat{U}_{z2}$ are single qubit gates such that

$$\hat{U}_{z1}\hat{U}_{z2} = \mathrm{diag}\{1, e^{i(\phi_{01}-\phi_{00})}, e^{i(\phi_{10}-\phi_{00})}, e^{i(\phi_{10}+\phi_{01}-2\phi_{00})}\},$$

and ϕ_m are the phases of the diagonal elements of matrix $\hat{W}$.

The gate errors of this voltage-controlled CZ gate, defined as $1-F$, are calculated as a function of T_0, as shown in Fig. 4-5(a). The error increases as T_0 becomes larger because for fixed switching time $\tau_s = 15$ ns, larger T_0 means the energy levels are shifted faster, which results in greater transition error, see Fig. 4-4. The benefit of larger transmission T_0 is the shorter gate time because it requires less time for Eq. (4.32) to be achieved, as shown in Fig. 4-5(b). The trade-off between the gate fidelity and time determines the optimal value for T_0. The kink of the red solid line, located at $T_0 \simeq 0.013$, happens because the relative phase accumulated during the switching on and off processes equals $-\pi$, i.e., $\tau_w = 0$. Further increasing T_0 means the relative phase during the switching processes exceeds $-\pi$. To satisfy the phase condition (4.32), a finite-time interacting plateau is needed to complete another 2π

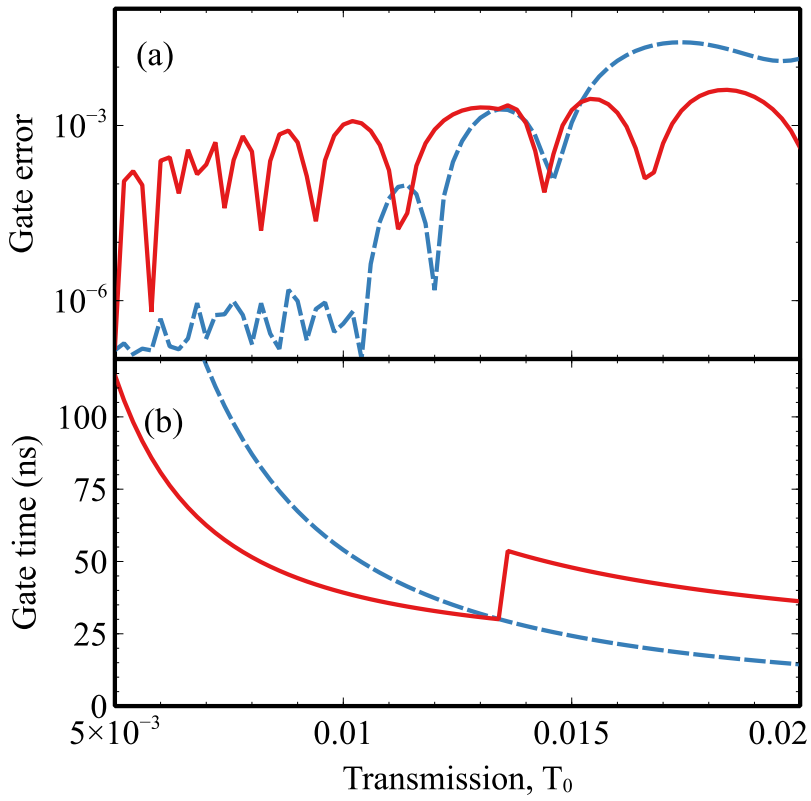

Figure 4-5: (a) (Color online) Error for the CZ gate and (b) corresponding gate time as functions of "on"-transmission T_0. The solid red lines are calculated assuming a pulse shape with an interacting plateau, so the gate time is $\tau_w + 2\tau_s$. Here, we take $\tau_s = 15$ ns. The dashed blue lines assumes the transmission is turned off right after it arrives its maximum value T_0, thus $\tau_w = 0$, and the gate time is $2\tau_s$, which is determined by the phase condition Eq. (4.32).

rotation. The blue dashed lines represent the gate error and time of pulses whose interacting plateau is absent, $\tau_w = 0$, and the gate time $\tau_{\text{gate}} = 2\tau_s$. The time-averaged $T_c(t)$ is smaller for $\tau_w = 0$ pulses, therefore longer gate times are required. At the same time, longer switching times allow for smaller gate errors. We observe that for small T_0 (≤ 0.01), the error can be reduced below 10^{-6} while the gate time is shorter than 100 ns.

4.3.2 Two coupled gatemons

Replacing the insulating tunnel barrier between superconducting electrodes by semiconductor allows one to easily tune the Josephson Energy by using a electrostatic

gate. [91] This type of transmon is thus named as gatemon for its gate tunable feature. With higher transparency between the tunnel barrier and the superconducting electrodes, expanding the ABS energy to the first order of T_α no longer well approximates the ABS energy, where $\alpha = 1, 2$ denotes the qubit index. Here, we consider single channel tunnel barriers with transmission T_α of gatemon $\alpha = 1, 2$. Then the Josephson energy of a qubit to the quartic order in θ_α is

$$\begin{aligned} H_{J\alpha} &= -\Delta\sqrt{1 - T_\alpha \sin^2\left(\frac{\hat{\theta}_\alpha}{2}\right)} \\ &\simeq -\Delta\left(1 - \frac{T_\alpha}{8}\hat{\theta}_\alpha^2 + \frac{T_\alpha}{96}\left(1 - \frac{3T_\alpha}{4}\right)\hat{\theta}_\alpha^4\right). \end{aligned} \tag{4.34}$$

The anharmonicity of gatemon is suppressed [95] by $(1 - 3T_\alpha/4)$ in Eq. (4.34), which can usually be ignored in transmon systems with tunnel junctions containing many weakly transparent channels, $T_\alpha \ll 1$. We choose the parameters of the gatemon and transmon system to be identical and they are to be given by Eq. (4.16). The Josephson energy E_J of a gatemons' single channel junctions corresponds to $T_{\alpha=1,2} = 1$. The energy spectrum, including their anharmonicities are different for transmons and gatemons, see Table 4.1, due to the difference in coefficients of $\hat{\theta}_\alpha^4$ terms in Eqs. (4.12) and (4.34).

The connecting junction between two qubits, once acquires non-zero transmission, $T_c \neq 0$, introduces an interaction between two qubits the same way as in transmon systems (see Sec. 4.3.1). With reduced anharmonicity, the state $\widetilde{|02\rangle}$ has higher energy than its counterpart in transmon qubits. State $\widetilde{|11\rangle}$ is therefore sandwiched between $\widetilde{|02\rangle}$ and $\widetilde{|20\rangle}$ in this case. We also make a plot of the relative energy shift Δ_{CZ} as a function of T_c for the gatemon, shown in Fig. 4-6. As discussed in Sec. 4.3.1, the non-zero Δ_{CZ} enables the realization of CZ gate by switching on and off T_c, which inevitably introduces transition error. The most probable transition, the same as in transmon qubits, still happens between states $\widetilde{|11\rangle}$ and $\widetilde{|02\rangle}$ since this transition has smaller energy gap and larger interaction than other transitions involving computational basis.

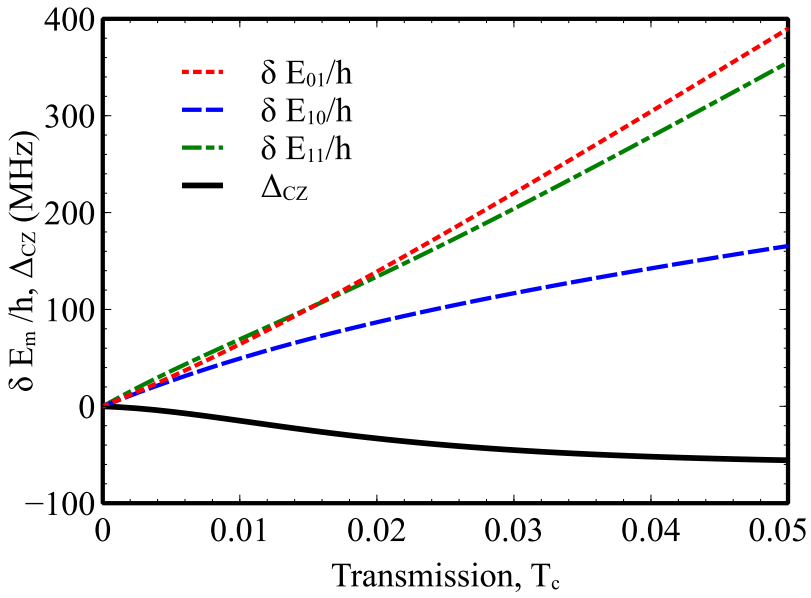

Figure 4-6: (Color online) Energy shifts on eigenenergies, $\delta E_m = \tilde{E}_m - E_m$, of the two-gatemon system as a function of transmission T_c. Only three out of four states in computational subspace are depicted. The shift δE_{00}, omitted for a clearer view, can be calculated using the relative shifts $\Delta_{CZ} = (\tilde{E}_{11} + \tilde{E}_{00} - (\tilde{E}_{10} + \tilde{E}_{01}))/h$, shown as thick black solid line. The parameters are the same as the transmon system, as listed in Eq. (4.16).

To see how much the transition between states with smallest energy separation can reduce the gate fidelity during switching processes, we start from state $\widetilde{|11\rangle}$ and calculate the transition probability during switching-on process by (i) numerically calculating the evolution operator and (ii) approximating the system by a 2-level model and using Eq. (4.31). The 2-level approximation has been discussed in Sec. 4.3.1.

As shown in Fig. 4-7, the transition probability from state $|11\rangle$ to state $\widetilde{|02\rangle}$ drops fast as the switching time increases. Specifically, the transition probability to state $\widetilde{|02\rangle}$ can be smaller than 10^{-3} when the switching time is larger than 20 ns.

The relatively smaller shift of Δ_{CZ} in Fig. 4-6 indicates longer CZ gate time for gatemon than transmon qubits for the same T_c. And the decrease in anharmonicity results in potentially smaller fidelity for other qubit operations not discussed in this chapter, since it makes the qubit transition frequencies among computational basis less distinguished from other undesired transitions involving levels out of the computational basis. Fig. 4-8 shows both the gate error and gate time as functions of

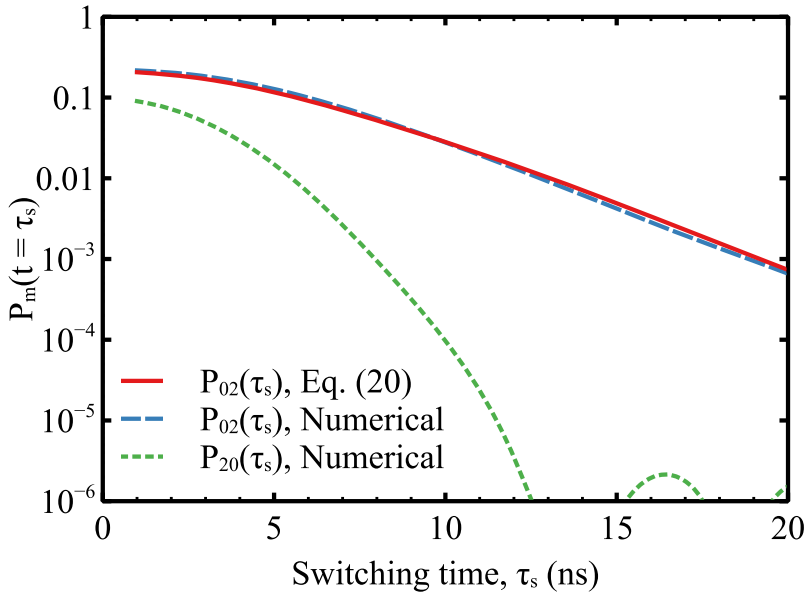

Figure 4-7: Leakage from state $|11\rangle$ to state $|02\rangle$ and $|20\rangle$ during the switching on of transmission T_c of a junction connecting two gatemon qubits as a function of switching time τ_s for $T_0 = 0.015$.

transmission T_0 for gatemon qubits. The solid lines are the gate error and gate time when finite-τ_w pulses are applied while the dashed lines correspond to $\tau_w = 0$ pulses.

Figure 4-8(a) does not show an obvious suppression in fidelity compared to the transmon qubits due to the reduced anharmonicity since the error in this CZ gate mainly comes from the transition error between states $|\widetilde{11}\rangle$ and $|\widetilde{02}\rangle$ during switching processes and no coherent drive is applied. The oscillations are a result of interference between states $|\widetilde{11}\rangle$ and $|\widetilde{02}\rangle$ during the gate. Fig. 4-8(b) shows that the gate time can be well below 50 ns when $T_0 > 0.01$.

4.3.3 Two qubits formed by a 4-terminal junction

Josephson energy

We formulate a model for a system of two gatemon qubits connected through lithographically formed multiterminal junctions, such as an H–junction shown in Fig. 4-9. We assume that the junction is short, its scattering matrix $\hat{S}$ is energy independent and each terminal has only one conduction channel. Two terminals are connected to

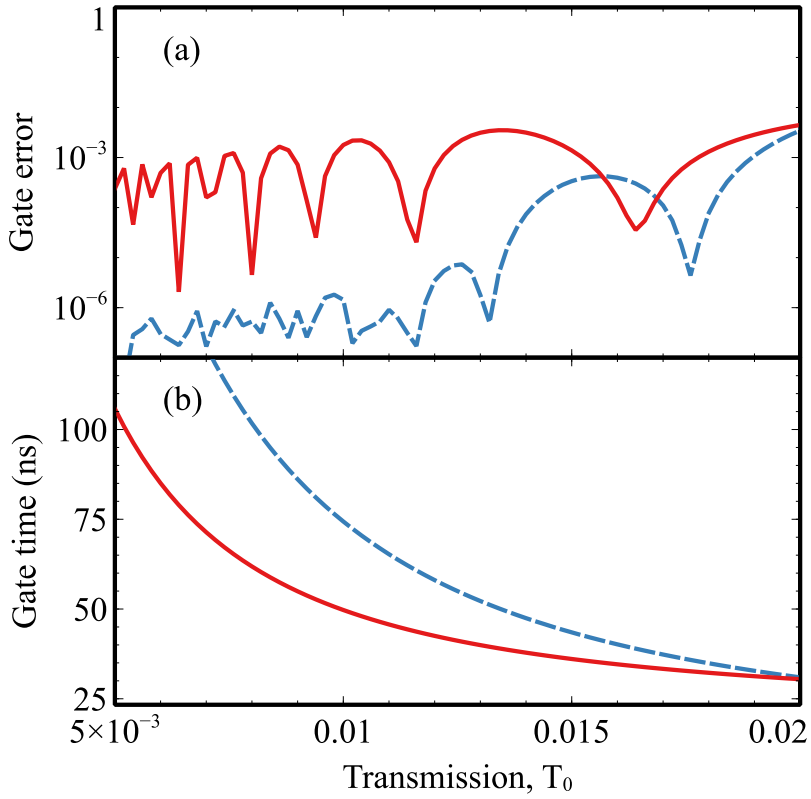

Figure 4-8: (a) (Color online) Error for the CZ gate on gatemon qubits and (b) corresponding gate time as functions of "on"-transmission T_0. The solid red lines are calculated assuming a pulse shape with an interacting plateau, so the gate time is $\tau_w + 2\tau_s$. Here, $\tau_s = 15$ ns. The dashed blue lines assumes $\tau_w = 0$.

the superconducting ground lead, while the other two terminals are connected to the gatemon capacitor plates, see Fig. 4-9.

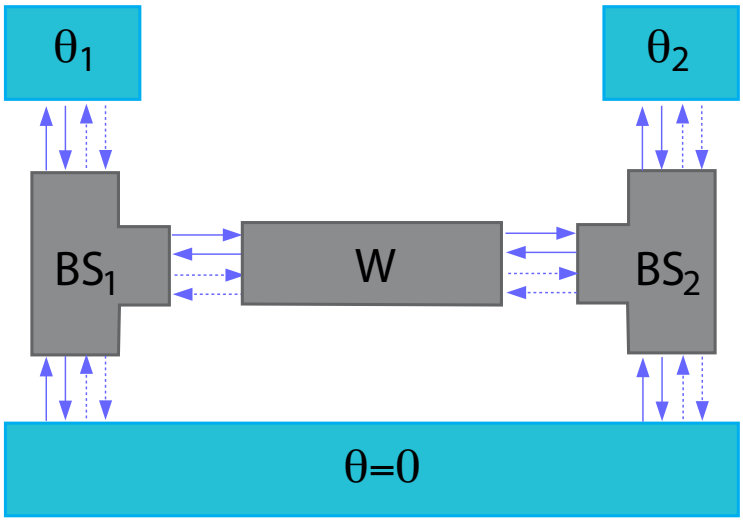

Figure 4-9: H-junction consists of two semiconductor beam splitters, $BS_{1,2}$, connected by a short wire (W). The other two terminals of each beam splitter are attached to the ground superconducting strip and to the superconducting plates of the transmon–like qubit, with superconducting phase $\theta_{1,2}$.

A set of localized sub-gap Andreev bound states are formed in the junction. These states are spin-degenerate which is guaranteed by Kramer's theorem. The energies of Andreev bound states are determined by the eigenvalue equation [103]

$$\det\left[1 - e^{-2i\chi}\hat{S}e^{i\hat{\theta}}\hat{S}^{*}e^{-i\hat{\theta}}\right] = 0, \tag{4.35}$$

where the phase factor $\chi = \arccos(\epsilon/\Delta)$ captures Andreev electron-hole reflection at the superconductor-normal interface, Δ is the superconducting gap in the leads, and $e^{i\hat{\theta}}$ is a diagonal matrix that assigns the superconducting phase θ_i to each channel, $\hat{\theta} = \mathrm{diag}\{\theta_1, \theta_2, \theta_3, \theta_4\}$. $\hat{S}$ is the scattering matrix of size 4×4 for the H-junction, which is a combination of two three terminal junctions with two terminals connected by a short wire with transmission T_c; see the supplementary information. Since the phases of channels coupled to the ground superconducting lead can be fixed to zero, the Josephson energy is defined by Eq. (4.35) in terms of only two phase variables $\theta_{1,2}$.

The Andreev energy states of the H-junction are [101]

$$\varepsilon(\boldsymbol{\theta}) = \pm\sqrt{\frac{A(\boldsymbol{\theta}) + 4 \pm \sqrt{A^2(\boldsymbol{\theta}) - 4B(\boldsymbol{\theta}) + 8}}{8}}, \tag{4.36}$$

where $\boldsymbol{\theta} \equiv (\theta_1, \theta_2)$ and the A- and B-functions take the form

$$A(\boldsymbol{\theta}) = A_0 + \sum_{\alpha=1}^{2} A_\alpha \cos\theta_\alpha + A_{12}\cos(\theta_1 - \theta_2), \tag{4.37a}$$

$$\begin{aligned} B(\boldsymbol{\theta}) = {} & B_0 + \sum_{\alpha=1}^{2} B_\alpha \cos\theta_\alpha + B_{12}^{-}\cos(\theta_1 - \theta_2) \\ & + B_{12}^{+}\cos(\theta_1 + \theta_2). \end{aligned} \tag{4.37b}$$

In terms of the matrix elements of $\hat{S}$ the coefficients in Eqs. (4.37a) and (4.37b) read

$$\begin{aligned} A_0 &= 2|S_{14}|^2 + \sum_{\beta=1}^{4} |S_{\beta\beta}|^2, \quad A_{12} = 2|S_{23}|^2, \\ A_\alpha &= 2\left(|S_{1,\alpha+1}|^2 + |S_{\alpha+1,4}|^2\right), \end{aligned} \tag{4.38}$$

and

$$\begin{aligned} B_0 = {} & 2\left(|S_{12}S_{24} - S_{14}S_{22}|^2 + |S_{13}S_{34} - S_{14}S_{33}|^2\right) \\ & + \sum_{\alpha<\beta} \left|S_{\alpha\alpha}S_{\beta\beta} - S_{\alpha\beta}^2\right|^2, \\ B_1 = {} & |S_{13}S_{23} - S_{12}S_{33}|^2 + |S_{14}S_{24} - S_{12}S_{44}|^2 \\ & + |S_{12}S_{14} - S_{11}S_{24}|^2 + |S_{24}S_{33} - S_{23}S_{34}|^2, \\ B_2 = {} & |S_{12}S_{23} - S_{13}S_{22}|^2 + |S_{14}S_{34} - S_{13}S_{44}|^2 \\ & + |S_{13}S_{14} - S_{11}S_{34}|^2 + |S_{23}S_{24} - S_{22}S_{34}|^2, \\ B_{12}^{-} = {} & |S_{12}S_{13} - S_{11}S_{23}|^2 + |S_{24}S_{34} - S_{23}S_{44}|^2 \\ & + |S_{14}S_{23} - S_{12}S_{34}|^2 + |S_{14}S_{23} - S_{13}S_{24}|^2, \\ B_{12}^{+} = {} & |S_{13}S_{24} - S_{12}S_{34}|^2. \end{aligned} \tag{4.39}$$

The Josephson energy of an H-junction has a series expansion to the fourth order in the superconducting phases $\theta_{1,2}$:

$$H_{\rm JJ}(\theta_1,\theta_2)=\Delta\sum_{i,j=0}^{4}K_{ij}\theta_1^i\theta_2^j, \tag{4.40}$$

where coefficients K_{ij} are obtained from the expansion of Eq. (4.36) to the forth order in $\theta_{1,2}$, and we take $K_{ij}=0$ for $i+j>4$ to avoid higher order terms. For $T_c=0$, the two qubits do not interact and

$$H_{\rm JJ}(\theta_1,\theta_2)=\Delta\left(K_{20}^{(0)}\theta_1^2+K_{40}^{(0)}\theta_1^4+K_{02}^{(0)}\theta_2^2+K_{04}^{(0)}\theta_2^4\right). \tag{4.41}$$

The full Hamiltonian of the system is similar to the Hamiltonian of a transmon Hamiltonian, Eq. (4.12) with $E_{J,1}=2\Delta K_{20}^{(0)}$, $E_{J,2}=2\Delta K_{02}^{(0)}$ and a modified anharmonicity. When the wire acquires finite transmission, $T_c\neq 0$, the interaction between the qubits develops with the interaction term given by

$$V_{\rm int}=\Delta\sum_{i,j=0}^{4}\delta K_{ij}\theta_1^i\theta_2^j,\quad \delta K_{ij}=K_{ij}-K_{ij}^{(0)}. \tag{4.42}$$

The scattering matrix for the H-junction, Fig. 4-9, can be constructed in terms of the scattering matrices for each beam splitter and the connecting wire, see the Appendix. We use Eqs. (4.36)-(4.39) to characterize the qubit system, called H-pair, and evaluate the CZ gate fidelity for a particular choice of parameters for the beam splitters. We demonstrate that this system is sufficient for control of energy splitting of individual qubits and fast switching the interaction between qubits.

Controlled–Z gate

For the H-pair, state $\widetilde{|11\rangle}$ is close to leakage states $\widetilde{|20\rangle}$ and $\widetilde{|02\rangle}$. To reduce the excitations to non-computational states, we keep the interaction strength below the anharmonicity level, $\sim E_C$, and imply that the transmission of the connector is small, $T_c\lesssim\sqrt{E_c/\Delta}\ll 1$. Here we allow for the wire transmission to have larger

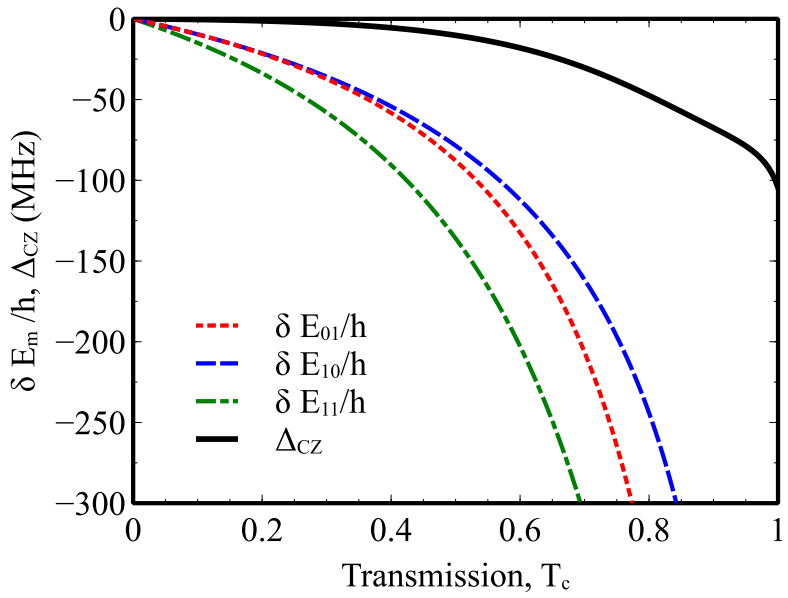

Figure 4-10: Energy shifts on eigenenergies, $\delta E_m = \tilde{E}_m - E_m$, of the two-qubit systems. The charging energies $E_{c1}/h = 240$ MHz and $E_{C2}/h = 255$ MHz for qubit one and qubit two respectively, the same as the values given in Eq. (4.16). $K_{02,20} = 0.123$, corresponding to Josephson energy $E_J/h = 20.24$ GHz.

values $T_c \simeq 1$, but we choose such parameters of the Y-junction that the resulting conductance of the H-junction between the qubits is small. The Josephson energy, Eq. (4.40), acquires terms with small $K_{ij} \neq 0$ for both $i, j \neq 0$, resulting in interaction between the qubits. In particular, the coefficient K_{11} is the dominant term describing the coupling between the qubits.

The anharmonicity of the H-pair is reduced by a numerical factor as compared to conventional AlO_x oxide tunnel Josephson junction [95], as we also discussed in Sec. 4.3.2, but this reduction is not significant and still permits high-fidelity gates for two qubits coupled by the nanowire. We still choose the charging energies of each gatemon to be $E_{c1} = 255$ MHz and $E_{c2} = 240$ MHz, as shown in Eq. (4.16). Below we choose parameters for beam splitters so that $K_{20,02} \simeq 0.1$. For the specific case $K_{20,02} = 0.123$, the qubit transition frequencies and anharmonicities are listed in Table 4.1. For non-ideal transmission of conduction channels, the qubit frequency is smaller, but additional conduction channels in the junction can help adjust this frequency to a desirable value.

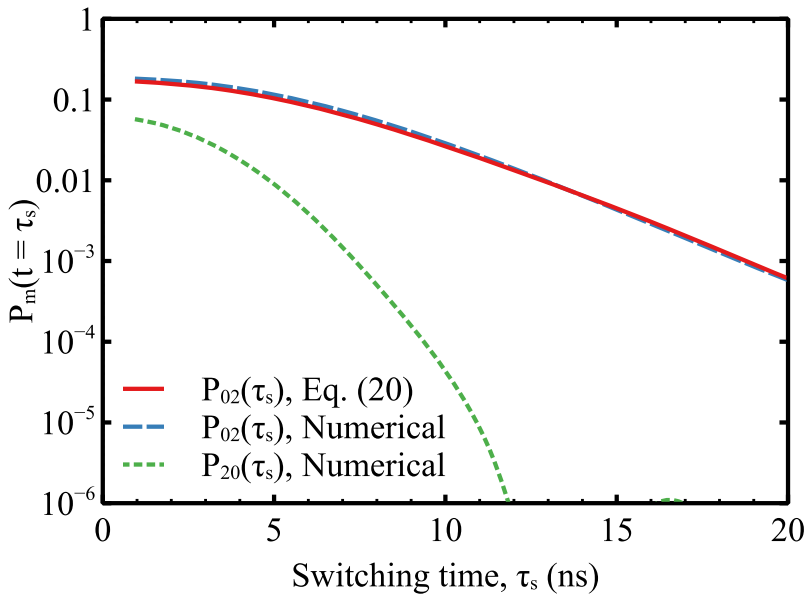

Figure 4-11: Transition probability to from state $|11\rangle$ to state $|02\rangle$ and $|20\rangle$ as a function of switching time for the H-junction qubits. "On"-transmission $T_0 = 0.6$. Charging energies and superconducting gap are the same as the transmon qubits and gatemon qubits. For our choice of parameters, $K_{02,20} = 0.123$, corresponding to Josephson energy $E_J/h = 20.24$ GHz.

Due to relatively large connectivity of the individual qubit junction, the absolute value of anharmonicities are suppressed so that the state $\widetilde{|11\rangle}$ is sandwiched between states $\widetilde{|02\rangle}$ and $\widetilde{|20\rangle}$. As expected from previously discussed two qubit systems, the non-zero transmission gives rise to finite Δ_{CZ}, shown by a thick solid line in Fig. 4-10, enabling the construction of CZ gate by switching T_c.

In absence of decoherence, the gate error comes from the transitions to levels outside the computational basis during switching on/off interactions. Taking $T_0 = 0.6$ for the connecting wire, we investigate how transition probability decreases as switching time τ_s increases. As shown in Fig. 4-11, the transition error can be readily reduced to 10^{-3} for switching time longer than 20 ns.

The relatively small change of Δ_{CZ} in Fig. 4-10 in transmission from $T_c = 0$ to $T_c = 0.8$ indicates a quite flexible tunable coupler for the H-pair. For a fixed switching time, smaller 'on'-interaction, which corresponds to smaller T_0, can prevent transitions during switching, but requires longer time to accomplish CZ gate. In contrast, larger interaction is good for gate time, though it acquires larger transition

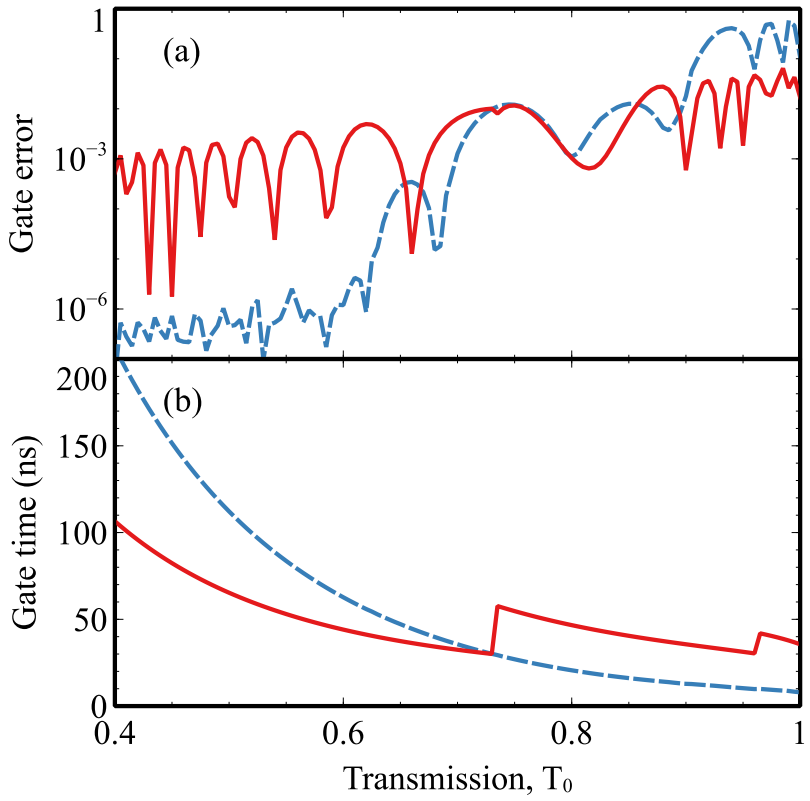

Figure 4-12: (a) (Color online) Error for the CZ gate and (b) corresponding gate time as functions of "on"-transmission T_0 of an H-pair. The solid red lines are calculated assuming a pulse shape with an interacting plateau, so the gate time is $\tau_w + 2\tau_s$. Here, we take $\tau_s = 15$ ns. The dashed blue lines assumes the transmission is turned off right after it arrives it's maximum value T_0, thus the gate time is $2\tau_s$.

error. Truncating unpractical ranges for 'on'-transmission T_0, we make plots of gate error and time as functions of T_0, as shown in Fig. 4-12. Figure 4-12 shows that for a large range of wire transmission, the worst case error can be smaller than or on the order of 10^{-2} with the gate time shorter than 200 ns for this parameter set.

4.4 Summary

We compared three kinds of qubits, namely a pair of transmons or gatemons as well as an H-pair by theoretically realizing a CZ gates through tuning inter-qubit interaction and taking a look at their gate fidelity and gate time as functions of experimentally practical transmission range. The evolution of the three systems are

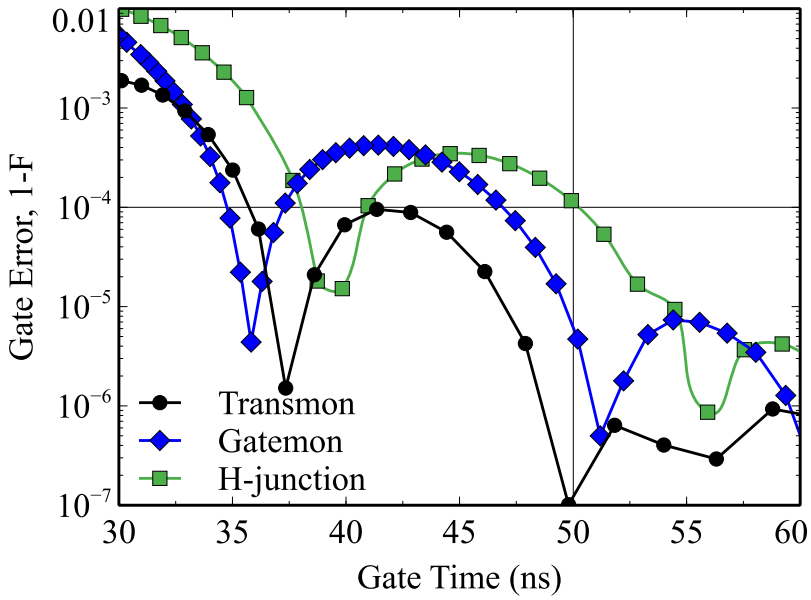

Figure 4-13: Error as a function of gate time for qubit systems analyzed above with waiting time $\tau_w = 0$. The charging energies are the same as what we used in previous figures. The Josephson energy $E_j = 20.55$ GHz for transmons and gatemons, and $E_j = 20.24$ GHz for qubits in H-pair. The corresponding qubit frequencies are listed in Table. 4.1. For gate time about 50 ns, all three qubit configurations allow for gate errors at the order of or less than 10^{-4}.

simulated by solving time-dependent master equations without decoherence for a general discussion. In general, decoherence can be included as Lindblad terms in the Lindblad equation (see Chapter 2) but the physics and rates can be very different depending on different physical realizations of superconducting qubits. The error we present in this chapter are intrinsic errors of the CZ gate realized by a tunable coupler due to a time-dependent Hamiltonian. For all three systems, fidelity and gate time are generally not positively correlated and optimal transmission needs to be chosen to ensure reasonable gate time and error. Fortunately, numerical analysis show the existence of this optimal regime of transmission for all three systems, as shown in Fig. 4-13.

In general, a transmon has larger anharmonicities than a gatemon or H-pair. This explains the different relative positions of states $\widetilde{|11\rangle}$ and $\widetilde{|02\rangle}$ for transmon system and the other two in this chapter. For other choices of charging energies, this difference may not manifest as the obvious different energy configurations, but depending on

different ways of realizing qubit gates, the transmon with larger anharmonicity may have a better fidelity as it distinguishes transitions among its computational basis from other transitions better than small anharmonicity system.

gatemon, it inherits the freedom of tuning qubit frequencies. Therefore, even with slightly longer gate time and potential operation error compared to traditional transmon, it allows for easy control of the energy scales and interactions, thus both single qubit gates and two-qubit entangling gates can be easily realized with little error coming from cross-talk or frequency crowding.

The CZ gate can be realized in systems with always-on interaction by shifting qubits' spectrum in resonance to temporarily enhance the interaction between two qubits, *e.g.* by bringing energies of states $|11\rangle$ and $|20\rangle$ to the same value [79, 105]. But even for the "off" configuration of qubits, the phase difference $\propto \Delta_{CZ}$ continuously accumulates and reduces gate fidelities of single qubits. Such error accumulation becomes especially crucial for large scale qubit systems. Also, changing qubit frequency in the crowded spectrum of a large interacting system will cause numerous level crossing that will cumulatively result in large gate errors. Therefore, a tunable coupler between the qubits is a necessary element for a scalable quantum processor. The previous realization of inductive tunable coupler was utilized in g-mon systems[96, 97, 107], where the coupling is controlled by the flux bias. In this chapter we demonstrated that an inductive tunable coupling can also be controlled by electrostatic gate voltages by utilizing the epitaxial semiconductor Josephson junctions.

Chapter 5

Digital control of quantum circuits

Using the microwave pulses to coherently control superconducting qubits is natural in the superconducting circuits. Although it is experimentally demonstrated that both high-fidelity single-qubit gates and two-qubit gates are feasible using microwave drive, the pulse generation and routing requires immense overhead with devices that is hard to be incorporated into low-temperature qubit environment.

One possible solution is to consider using rapid single flux quantum (SFQ) logic, which is a rather mature superconducting technology and can be easily incorporated into the same temperature stage as the qubits. The use of SFQ circuits in controlling Josephson devices were suggested in [108–110] and a few experiments focusing on controlling the qubit system parameters using SFQ [111, 112] or qubit readout [113–115] have been taken.

It is until more recently that direct excitations of superconduting qubit using SFQ pulses in place of microwave drive is proposed[116] and realized in transmon qubit with high fidelity [117].

In this chapter, we will first follow the proposal[116] to briefly describe how SFQ pulses can be used to coherently control a superconducting qubit. Then we will discuss the possibility of implementing two-qubit gates, specifically CNOT and CZ gates with SFQ pulses.

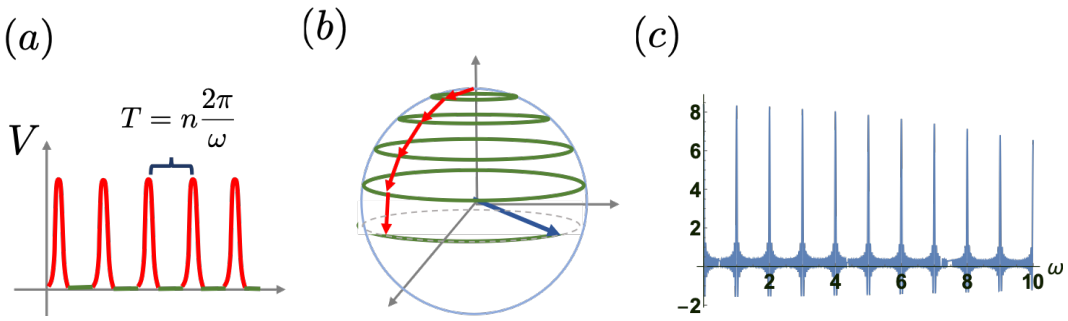

Figure 5-1: (a) SFQ pulse sequence in time domain. (b) The coherent control of SFQ pulses over a two-level system. (c) SFQ pulse sequence in frequency domain when there are 20 pulses. The original pulse sequence has a period of 1 (arbitrary unit) and Guassian shape with width of 0.1.

5.1 SFQ pulses for coherent control of a qubit

The technology of SFQ pulse generations is based on storage and transimission of classical bits in the form of fluxons, which are time integral of voltages. Let us denote the flux quantum by $\Phi_0 = \int V(t)dt$, where the integral is taken over the pulse duration time (about 2 ps). Regular SFQ pulses are usually generated and transmitted equally-spaced in time, as shown in Fig. 5-1 (a). $T = \frac{2\pi}{\omega}$ is the time interval between two neighboring pulses. Since the duration of each pulse is much less than the time intervals, SFQ pulses can usually be modeled as delta functions such that $V(t) = \Phi_0\delta(t)$. Unlike sinusoidal microwave drives which continuously drive the qubit from one state to the other, these delta pulses induce sudden small rotations that get add up coherently by matching the qubit frequency with the pulse frequency, as shown in Fig. 5-1(b).

Another way to see why SFQ pulses work as driving forces for a two-level system is to look at its distribution on frequency domain. While single delta pulse corresponds to a trivial and boring constant pattern, equally-spaced delta sequence can have very narrow equally-spaced peaks in the frequency domain. Figure 5-1 (c) shows the Fourier transform of a sequence of only 20 narrow Gaussian functions. The width of these Guassians are one tenth of the pulse interval. When SFQ pulses are used to control a real qubit, there can be more higher energy levels hanging around. Generally speaking, the larger the width of each peak in the frequency domain is, the

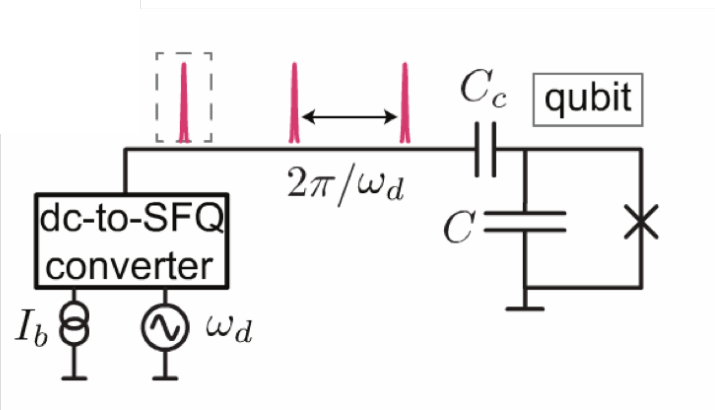

Figure 5-2: Reproduced from [117]. Circuit diagram of SFQ pulse controlled transmon. The transmon is capacitively coupled with the SFQ pulse train, which is generated by micorwave drive of the same frequency via a dc-to-SFQ converter.

more probable that leakage will be introduced to the system during the qubit control. Depending on the frequency resolution requirement, one can adjust the length of the pulse sequence. It is numerically estimated that the leakage can be below 0.1% for a pulse sequence of only 20 ns [116], which suggests that SFQ pulses is indeed a promising candidate for coherent control over superconducting qubits.

Figure 5-2 is a schematic circuit showing a transmon is controlled by SFQ pulses via a coupling capacitance reproduced from [117]. The rotation angle induced by each pulse is

$$\delta\theta = C_c\Phi_0\sqrt{\frac{2\omega_{10}}{\hbar C}}, \tag{5.1}$$

where C_c is the coupling capacitance and C is the capacitance of the transmon. ω_{10} is the qubit frequency.

Both Figure 5-1(b) and (c) intuitively suggest that the frequency of the pulse does not need to be exactly the same as the qubit frequency. It can be instead at a subharmonic of the qubit frequency $\omega_d = \omega_{10}/n$, where n is an integer larger than 1. The experiments in [117] shows that larger choice of n does not really affect the fidelity that much. For $n = 3$, the fidelity ranges from 94% to 97% and for $n = 41$, the fidelity is 95%.

5.2 Two-qubit gates realization using SFQ sequence

We have seen that single qubit coherent control by SFQ pulses is indeed practical. In the remaining part of this chapter, we will explore the possibility of implementing high-fidelity two-qubit gates with SFQ pulses which completes the puzzle of universal operations of a multi-qubit system.

5.2.1 Formulation of entangled system and CZ gates

We consider two transmons. One has three states and the other has four. For the three-level transmon, the Hamiltonian is

$$H_1 = \begin{pmatrix} 0 & 0 & 0 \\ 0 & \omega_1 & 0 \\ 0 & 0 & \omega_1 - \alpha_1. \end{pmatrix} \tag{5.2}$$

Similarly, the Hamiltonian of the four-level transmon $H_2 = \{0, \omega_2, \omega_2 - \alpha_2, \omega_2 - \alpha_2\}$ where ω_1 and ω_2 are frequencies of the two transmons and α_1 and α_2 are anharmonicities of them respectively.

With interaction J, the total Hamiltonian for the transmon system is $H_t = H_1 \otimes H_2 + J(a + a^\dagger) \otimes (b + b^\dagger)$, where a (b) and $a^\dagger$ ($b^\dagger$) are the creator and annihilator of the 3-level (4-level) transmon.

Interacting Gate and Strauch Gate

For weak-fixed interaction, this straightforward scheme for CZ gate realization may become less practical due to long gate time, as shown by the red dashed line in Fig. C-1. In a fixed-coupling system, to reduce the two-qubit gate time, larger interaction is needed, which introduces larger cross-talk errors for single qubit gates.

Another approach was proposed by Strauch [79, 105]. While this strategy can decrease the gate time, it requires tunable qubit frequency and a careful choice of sweeping time. In addition to introducing cross-talk errors for single qubit gates

due to the fixed coupling, it also introduces tunneling to leakage states during the sweeping of qubit frequency.

5.2.2 SFQ-activated scheme

The scheme is reminiscent to the microwave-activated controlled phase (MAP) gate realized in Ref. [104]. Here we theoretically analyze how this CZ gate is realized in two different near-resonant regimes, namely, large amplitude drive and small amplitude drive. We will explain how these two mechanisms are different and how both of them can be utilized to construct CZ gates. In short, for the small amplitude drive, the SFQ drives accelerate the conditional gate rate, decreasing the gate time. This is like a modification on the interacting gate. At large amplitude regime, the SFQ drives a nearly coherent transitions between states $\widetilde{|11\rangle}$ and a auxiliary state $\widetilde{|12\rangle}$. This is more similar to what happens in a Strauch gate.

Then in the next section, Sec. 5.2.2, we numerically show that the off-resonant SFQ pulses indeed decrease the gate time for both fixed-coupled system and tunable-coupled system.

Here we start by describing the idea of this SFQ-activated scheme. The frequencies of the two qubits should be carefully designed so that the states $|03\rangle$ and $|12\rangle$ are aligned, which means the anharmonicity of transmon two should satisfy $\alpha_2 = (\omega_2 - \omega_1)/2$ to align state $|03\rangle$ and $|12\rangle$ when $J = 0$. With a weak interaction J between two transmons, these two degenerate states will be split by an amount about $\sqrt{3}J$, as shown in Fig. 5-3. The interaction will also detune the transition frequency between states $|01\rangle$ and $|02\rangle$ and transition frequency between state $|11\rangle$ and $|12\rangle$. By this way, we are be able to pick out a unique transition frequency ω_t, which is between state $\widetilde{|12\rangle}$ and $(|12\rangle - |03\rangle)/\sqrt{2}$, where we use tilde to denote the eigenstate of the total Hamiltonian. With the presence of interaction J, the interacting conditional phase accumulation rate is

$$\zeta_0 \approx 2J^2 \frac{(\alpha_1 + \alpha_2)}{(\omega_2 - \omega_1 + \alpha_1)(\omega_1 - \omega_2 + \alpha_2)}. \tag{5.3}$$

Here, the contributions from the mix between state $|11\rangle$ and $|22\rangle$ is ignored because of smaller amplitude. For system with weak coupling ($J \sim 0.01$ GHz), a CZ gate may take up to one thousand nanosecond depending on the qubit frequencies and anharmonicities.

Small amplitude limit: AC-Stark shift Applying small amplitude SFQ pulse trains with frequency ω_d that is slightly detuned from ω_t on the second transmon causes ac-Stark shift on state $\widetilde{|11\rangle}$, which can be tuned to increase the CZ gate rate. The second order perturbation theory gives an estimate of the conditional phase accumulation rate

$$\zeta = \zeta_0 + \zeta_2. \tag{5.4}$$

Here,

$$\zeta_2 \approx -\frac{8\pi^2\delta\theta^2}{\omega_d^2}\frac{3J^2}{\Delta_d(\Delta_d+\sqrt{3}J)(\Delta_d+2\sqrt{3}J)}, \tag{5.5}$$

where $\delta\theta$ is the SFQ pulse amplitude, $\Delta_d = E_{\widetilde{12}} - E_{11} - \omega_d$ is the detuning between the drive frequency and the interested transition frequency. To ensure that the second perturbative approximation is valid, we need $T\delta\theta \ll \Delta_d$ here. The conditional gate time is π/ζ. A comparison between the theoretical estimation and numerical calculation is shown in Fig. 5-4(a). The numerical curves (red solid and blue dashed lines) are based on simulation of a twelve-level system. The difference between the SFQ drive and Microwave drive can hardly be seen and they both agree well with the perturbation theory at small amplitude regime. Figure 5-4(a) shows that the conditional gate rate can be enhanced by small amplitude off-resonant drives and thus decrease the gate time. However, for weak interaction strength, when the perturbation theory is readily applicable so that the leakage from computational subspace is acceptable at time $t_g = \pi/\zeta_0$, the increase is less than twice of original accumulation rate. In the subsection below, we discuss the large amplitude limit drive and demonstrate that this drive can also be utilized to decrease the gate time and become especially useful when the interaction is small.

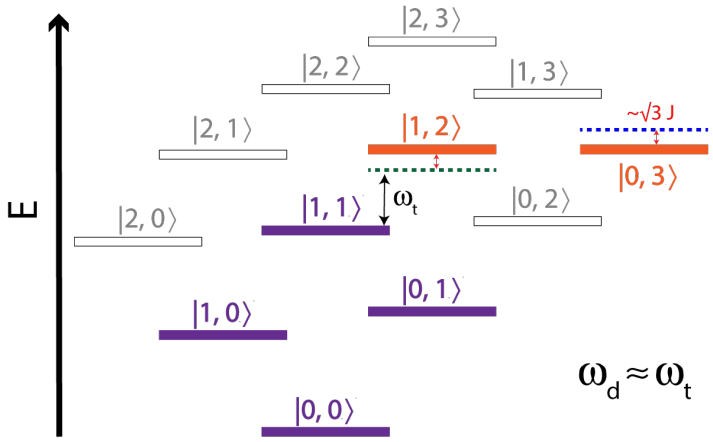

Figure 5-3: Level diagram of a two-transmon system. Purple levels are computational basis. Orange levels are auxiliary levels that are out of computational space. In the MAP scheme or SFQ-activated scheme, the auxiliary levels are carefully designed so that they are aligned when interaction is absent. The levels in computational subspace are colored purple and irrelevant levels are gray.

Large amplitude limit: near-coherent rotation

When the drive amplitude is large, perturbation theory no longer applies, and the state partially rotates between states $\widetilde{|11\rangle}$ and $\widetilde{|12\rangle}$. While a full rotation, which happens when Δ_d is negligible compared to $T\delta\theta$, results in a minus sign on state $\widetilde{|11\rangle}$, an off-resonant drive when the detuning can not be ignored gives a phase Φ_{rot} that is different from π on state $\widetilde{|11\rangle}$ when the state population is back to state $\widetilde{|11\rangle}$. At the same time, since the gate is accomplished in a finite duration of time, during which the conditional phase also gains a contribution Φ_{free} from free evolution, we can tune the pulse amplitude so that $\Phi_{rot} + \Phi_{free} = \pi$ when the population is back to state $\widetilde{|11\rangle}$. Therefore, the off-resonant large amplitude drive accompanied by the free evolution approximates a CZ gate.

In our simulation, we carefully choose a pulse amplitude by first looking at the population on state $\widetilde{|11\rangle}$, which shows Rabi oscillations due to the near-resonant drive. When the population completes one period at time T_R, we calculate the conditional phase given by the evolution operator $U(T_R)$ by projecting it onto the computational subspace. The pulse amplitude is chosen so that the conditional phase of projected $U(T_R)$ is $\pm\pi$, i.e., $U(T_R)$ is a CZ gate in the computational subspace.

Here we chose a set of parameters and present the quantum process tomography (QPT) of a SFQ-activated CZ gate in Figure 5-4(c) as an example. The gate has fidelity of compared to perfect CZ gate.

And we will show that when strong coupling is not available, or fixed weak coupling is required by high-fidelity single qubit operations, this off-resonant drive as an entangling gate will be preferable in a sense that gate time can be many times smaller with gate fidelity higher than 99%.

Fidelity

A typical dilemma in realizing quantum gates is that the interaction between qubits is necessary to entangle two qubits, and usually can construct faster two-qubit gate with higher strength, while it also introduces crosstalk, which reduces the fidelity of single qubit operations. In Sec. 5.2.2, we will first demonstrate that using this SFQ-activated CZ gate scheme, we are able to realize CZ gate even in very weak interaction regime, while still maintain short gate times and high fidelity. The weak interaction allows high-fidelity single qubit gates of a fixed-coupling system. We specifically compare the fidelities and gate times of the SFQ-activated CZ gate with interacting CZ gate, which simply utilizes the energy shift of state $\left|11\right\rangle$ compared to non-interacting eigenstate to construct a CZ gate. We then present how good our SFQ gates could be with tunable coupling and/or variable-frequency qubits, which have already been realized in experiments [96, 97, 107, 118].

The fidelity we use to measure the performance of qubit gates is the average fidelity $F = \int \left|\left\langle\psi\right|M\left|\psi\right\rangle\right|^2 \mathrm{d}V$, where the integral is taken over all possible initial states in the computational subspace of a system, $M = U_0^\dagger U_{act}$, U_0 is the ideal gate we intend to perform on the system, $U_{act} = PUP^\dagger$ is the actual gate in computational subspace realized by SFQ pulse sequence or the interacting CZ gate in our case and P is the projection operator from full space to computational subspace. It can be proven [106] that F takes the form of

$$F = \frac{1}{n(n+1)}\left[\mathrm{Tr}(MM^\dagger) + |\mathrm{Tr}(M)|^2\right], \tag{5.6}$$

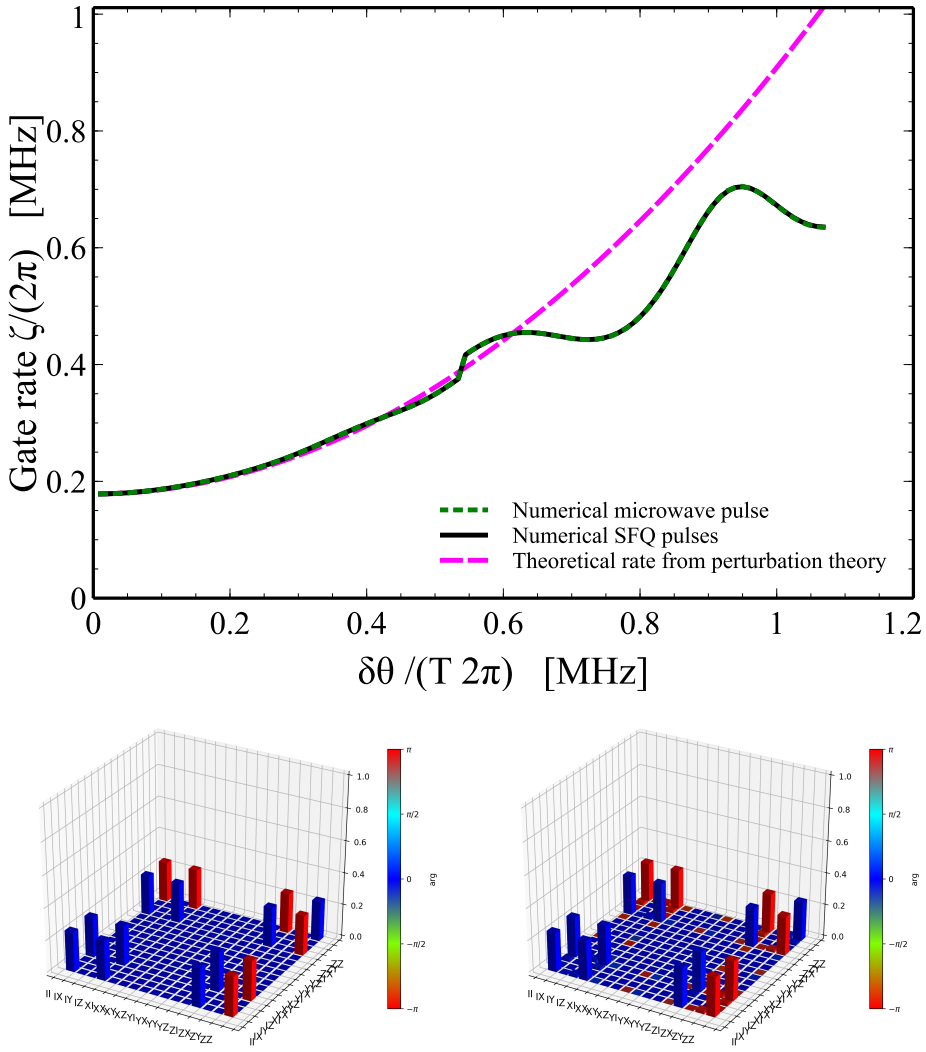

Figure 5-4: (a) The phase accumulation rate as a function of pulse amplitude. The amplitude of microwave drive is chosen so that it is equivalent to the shown SFQ amplitude, i.e., $A = T\delta\theta$. The theoretical estimate is given by Eq. (5.4). The numerical curves are based on simulation of a twelve-level system. The difference between the SFQ drive and Microwave drive is negligible and they both agree well with the perturbation theory for small amplitude drives. (b) Quantum process tomography of ideal CZ gate (left) and SFQ CZ gate (right).

where n is the dimension of the system. For two qubit gate, $n = 4$.

Fixed–coupling qubits

For a fixed-coupling system, measurements are taken with the presence of the interaction. Theoretically, this means the CZ gate realized on the eigenbasis of the interacting Hamiltonian is directly compared to the ideal CZ gate on the bare eigenbasis of non-interacting Hamiltonian. In this case, the difference between the bare states and the eigenstates of full Hamiltonian contributes errors to both interacting CZ gate and SFQ-activated CZ gate.

In Figure C-1, we present the fidelity (upper panel) and gate time (bottom panel) of CZ gates as functions of interaction strength J. The interacting CZ gate gains more error for large interacting. This is expected because stronger interaction means the transformation matrix between the bare eigenbasis and interacting eigenbasis are less likely to identity, which messes up the CZ gate on the interacting eigenbasis. For the SFQ CZ gate, the error has two sources. One is the difference between two basis, and the other is the leakage from the computational basis. The mix of two different error sources makes the trend of the error as a function of interaction more complicated.

Tunable–coupling

When the coupling is tunable, the single qubit gates are routine and is not sensitive to the frequencies of each qubit as long as they do not interact. We will focus on two-qubit gate. After CZ gate during which the state $\widetilde{|11\rangle}$ acquires a minus sign, we can adiabatically switch off the interaction so that the CZ gate on the interacting eigenstates evolves into a CZ gate on bare states.

While we can avoid the errors due to the difference between different sets of basis, the switching processes inevitably introduce transition among levels. To theoretically analyze the transitions during the switching processes, we can resort to the same method used in Sec. 4.3.1.

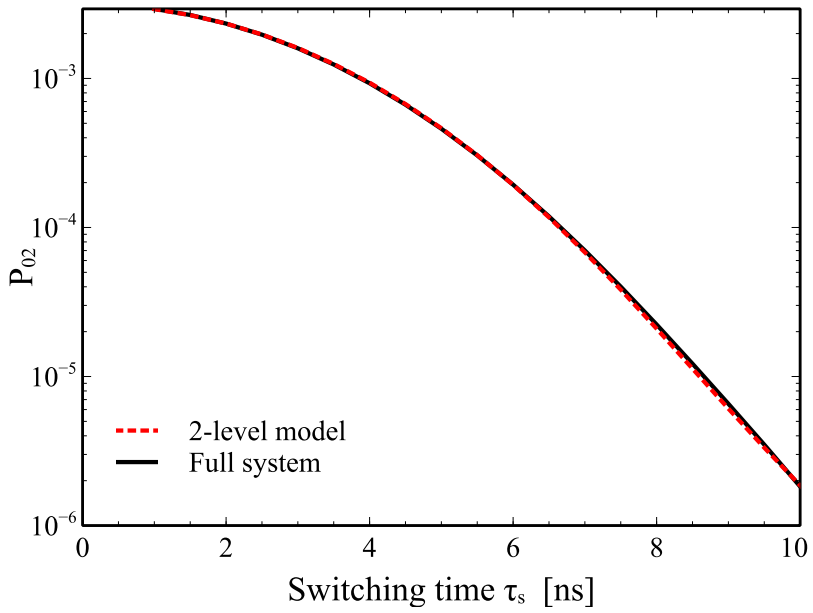

Figure 5-5: (Color online) (a) Transition probabilities to state $\left|0\tilde{2}\right\rangle$, denoted by P_{02}, as a function of switching time for CZ gate. Interaction increases linearly with time and maximizes at 0.16 GHz. the insets show transition probabilities to state $\left|\tilde{02}\right\rangle$ during a switching-on interaction process, assuming the switching time is 10 ns and . The red circles are calculated using Eq. (**??**) which takes only two levels into account and the blue diamonds are numerical transition probability in a system where we have one three level transmon and one four level transmon (the system on which CZ gate is applied).

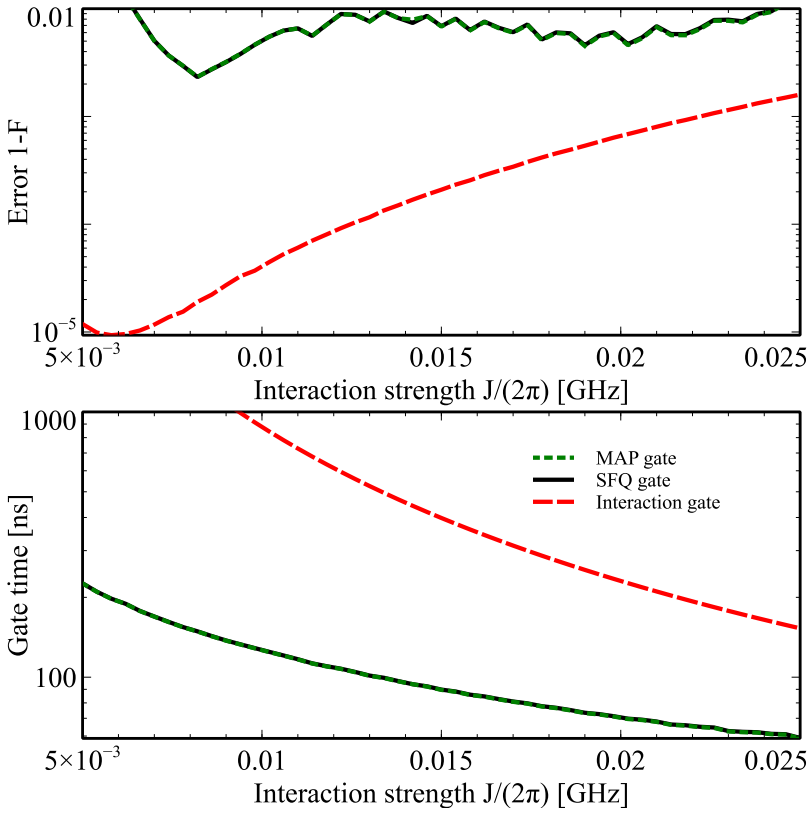

Figure 5-6: Fidelity (upper panel) and gate time (bottom panel) of CZ gates as functions of interaction strength J. The black solid line represents the data for SFQ CZ gate and red dashed line represents the interaction CZ gate. The parameters are the same as in Fig. C-1. The switching time for both switching on and switching off is 10 ns

Including the switching processes and single qubit Z gates, we make plots of the fidelity and gate time as functions of interaction strength J, as shown in Fig. 5-6.

With the switching processes, the CZ gate on the eigenbasis of interacting Hamiltonian is smoothly mapped to the CZ gate on the bare eigenbasis. The error of the interacting gate only comes from the transitions as analyzed above. For the SFQ-activated CZ gate, the error comes from both the transitions and the leakage from the computational basis when the drive is applied. Therefore SFQ gate indeed has larger errors than interacting CZ gate, as shown in the upper panel of Fig. 5-6. On the other hand, as the error is on or below the order of 10^{-2}, the gate time of SFQ CZ gates is dramatically decreased to less than a quarter of the interacting gate, which may make critical difference when decoherence are relaxations are present.

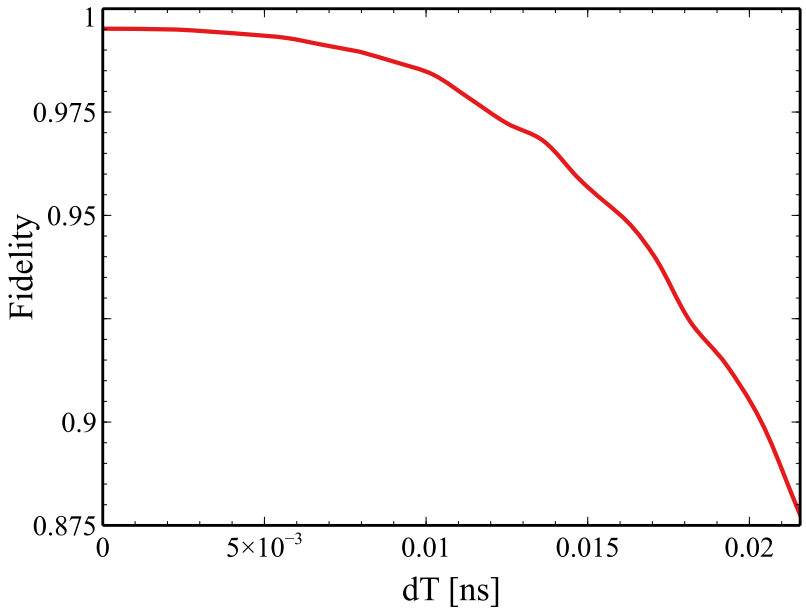

Figure 5-7: The fidelity as a function of the strength of timing jitter on an external clock. The parameters are the same as in Fig. C-1. The average drive frequency $\overline{\omega_d}$ is the same as the drive frequency in Fig. C-1.

Timing jitter

In real experiments, the arrival time of each pulse fluctuates and also results in gate errors. From Ref. [116], the average gate fidelity as a function of timing jitter magnitude dT is

$$F_{ave} = 1 - \frac{\omega_t dT^2}{6}\left(\frac{\Theta^2}{N} + 1\right), \tag{5.7}$$

where $\Theta = N\delta\theta$ and N is the total number of pulses.

In this chapter, we theoretically analyze the mechanisms of CZ gate realization using off-resonant SFQ pulse trains and show the equivalence between SFQ pulses and microwave drive. We conclude that both AC-stark shifts activated by weak drive and near-coherent rotation enabled by large drive can be utilized to construct CZ gates. We specifically investigate the large amplitude pulse regime in which the detuning between drive and the transition frequency of two interested levels are almost negligible. When the pulse-driven near-resonant rotation completes one cycle, it contributes to a phase Φ_{rot} that is near to -1. And the gap between -1 and Φ_{rot} can be filled by the phase accumulated during the finite gate time Φ_{free}. We numerically

show that this gate can be realized with fidelity generally higher than 99% in a tunable-coupler system, and decrease the gate time well below 100 ns even in very weakly coupled system. This scheme is also very useful for fixed-coupler system since it only requires weak interaction between qubits thus can avoid large cross-talk errors for single qubit gates. Unlike Strauch gate, it does not require any qubit frequency shifts, which may practically simplify the wiring of the system.

Chapter 6

Readout

In this chapter, we focus on the data extraction part of a quantum data processor (sounds like we already have one), i.e., the readout process. For superconducting qubit, this can be done by allowing the excited state to escape from a potential well [119]. Earlier design was also based on bifurcation amplifier [120, 121]. Currently, a widely used readout scheme is dispersive readout[122]. In Sec. 6.1, we will review the mechanism of this measurement scheme. Then in Sec. 6.2, we discuss how the state of a qubit is affected by the dispersive readout process, after which we move onto a more complex system – two coupled qubits, and develop a theory to intepret the non-monotonicity of the strength of crosstalk as a function of qubit-qubit detuning during a readout process, contrary to intuition. We also use quantum trajectory method that is introduced in Chapter 2 to simulate the dynamics of the two-qubit system, which gives consistent results compared to our theoretical estimate[123].

6.1 Dispersive readout

The basic idea of a dispersive readout scheme is to weakly couple a qubit with a resonator. This coupling results in a change of resonator frequency, qubit frequency and the direction of the change depends on the state of the qubit. This means the resonator has different frequencies for qubit in state $|0\rangle$ and $|1\rangle$. Extracting the frequency information allows one to infer the state of the qubit. A schematic circuit

of two coupled qubit with its readout resonator is shown in Figure 6-1. One can refer to either left half or right half of the figure as a typical simplified readout circuit for dispersive readout. Here we follow the derivation in Ref. [124] to explain the dispersive readout.

We focus our discussion on a two-level qubit for simplicity[1] When it is coupled to a resonator, the total Hamiltonian is

$$H_s = H_0 + \hbar g(a^\dagger \sigma_- + a\sigma_+), \tag{6.1}$$

where rotating wave approximation has been applied and only the Jaynes-Cummings interaction[125] is kept and H_0 is the non-interacting Hamiltonion, which takes the form

$$H_0 = \hbar\omega_R a^\dagger a + \hbar\omega_Q \frac{\sigma_z}{2}. \tag{6.2}$$

Here $a(a^\dagger)$ are annihilator(creator) of photon state in the resonator while σ_z is the Pauli Z matrix. ω_R and ω_Q are resonator frequency and qubit frequency respectively. In dispersive regime $|\Delta| = |\omega_Q - \omega_R| \gg g$, one can approximately diagonalize the above Hamiltonian H_s by [124]

$$\mathbf{D}_{\text{ Linear}} = e^{\lambda(a^\dagger\sigma_- - a\sigma_+)} \tag{6.3}$$

where $\lambda = g/\Delta$. The transformation gives an effective Hamitonian in the form of

$$\begin{aligned} H_{\text{eff}} &= \mathbf{D}^\dagger_{\text{Linear}} H_s \mathbf{D}_{\text{ Linear}} \\ &= \hbar\omega_R a^\dagger a + \hbar\left(\omega_Q + 2g\lambda\left[a^\dagger a + \frac{1}{2}\right]\right)\frac{\sigma_z}{2} + O\left(\lambda^2\right) \end{aligned}. \tag{6.4}$$

From the qubit perspective, the term $2g\lambda\left[a^\dagger a + \frac{1}{2}\right]\sigma_z/2$ is the AC Stark shift and Lamb shift to the qubit frequency due to the photons in the resonator. From the resonator perspective, this term can be understood as a modification to the resonator frequency based on the state of the qubit. Therefore the pull on the resonator fre-

[1]Qubit is by definition a two-level system. But in reality, states other than the computational basis usually exist.

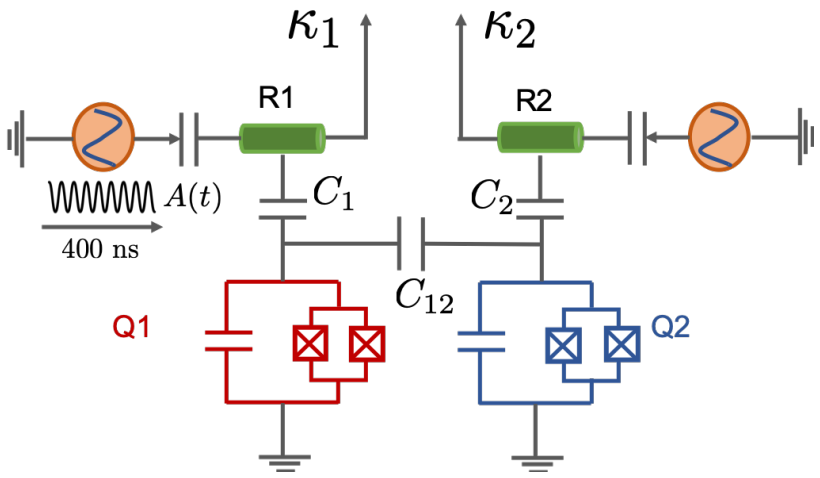

Figure 6-1: Two transmons with its readout resonator

quency is $\pm g\lambda$, where the sign depends on the qubit state.

As one expects from the second line of Equation.6.4, the effective Hamiltonian can be considered to contain only a linear term of λ requires that $\lambda \ll 1$, which is exactly the dispersive condition. It can also be translated to the condition that the number of photons should be much smaller than the critical photon number $n_{crit} = \Delta^2/4g^2$. Here we use a two-level qubit for the purpose of introducing the basic mechanism of dispersive readout. In an actual qubit, the dispersive shift could be very different due to the existence of higher energy states. One also needs to realize that this is a dissipative process since the information of the system keeps leaking out from the cavity, during which the qubit state also experience unwanted transitions due to its interaction with the readout reasonator. In the following section, we will discuss a more realistic case when a transmon is measured.

6.2 Single transmon readout

The Hamiltonian of a transmon takes the form of [126]

$$\hat{H}_Q = 4E_C\hat{n}^2 - E_J\cos\hat{\varphi}, \tag{6.5}$$

where the E_C is the charging energy, E_{J_i} is the Josephson energy, $\hat{n}$ is the cooper pair number operator and $\hat{\varphi}$ is the phase difference operator. In our numerical model, qubit Hamiltonian is written as a diagonal matrix in the Mathieu function basis, where the diagonal elements are the eigenvalues of Mathieu equation[126, 127].

In the readout circuit, a transmon qubit is coupled to a cavity which can be modeled as a harmonic oscillator. With capacitive coupling between the qubit and its readout cavity, the total Hamiltonian for a single qubit readout element is given by

$$\hat{H}_{QR} = \hat{H}_Q + \frac{\hbar\omega_R}{2}\hat{a}^\dagger\hat{a} + g\left(\hat{\Sigma}^+ + \hat{\Sigma}_i^-\right) \otimes \left(\hat{a}^\dagger + \hat{a}\right), \tag{6.6}$$

where $\hat{\Sigma}^\pm$ is the creator/annihilator of the qubit, defined in basis of the eigenfunction of Mathieu equation, $\hat{a}^\dagger(\hat{a})$ is the creator(annihilator) of the cavity photon, and ω_R is resonator frequency.

The readout drive takes the form

$$H_d = A(t)(\hat{a}^\dagger + \hat{a}), \tag{6.7}$$

where ω_d is the driving frequency and $A(t) = A\cos(\omega_d t)$ is the signal amplitude. Assuming the photon loss rate of the cavity is κ, and the relaxation rates of the qubit is γ, the system dynamics is governed by a Lindblad equation

$$\dot{\rho} = i\left[\rho, H_t\right] + \sum_k \mathcal{L}_k\rho\mathcal{L}_k^\dagger - \frac{1}{2}\left(\mathcal{L}_k^\dagger\mathcal{L}_k\rho + \rho\mathcal{L}_k^\dagger\mathcal{L}_k\right), \tag{6.8}$$

with every Lindblad operator $\mathcal{L}_k$ for each decay process and $H_t = H_d + H_{QR}$ denoting the total Hamiltonian of the system.

During this dissipative process, transitions originate from the resonator dissipation with the presence of the qubit-resonator interaction. The interaction, when written in Harmonic oscilator basis, or LC basis, only increases/decreases one LC excitation, therefore introduces the mixing among Mathieu eigenlevels. The decay operator, although acts on bare resonator photon states, causes qubit decay with the presence of the interaction, which gives rise to the Purcell decay.

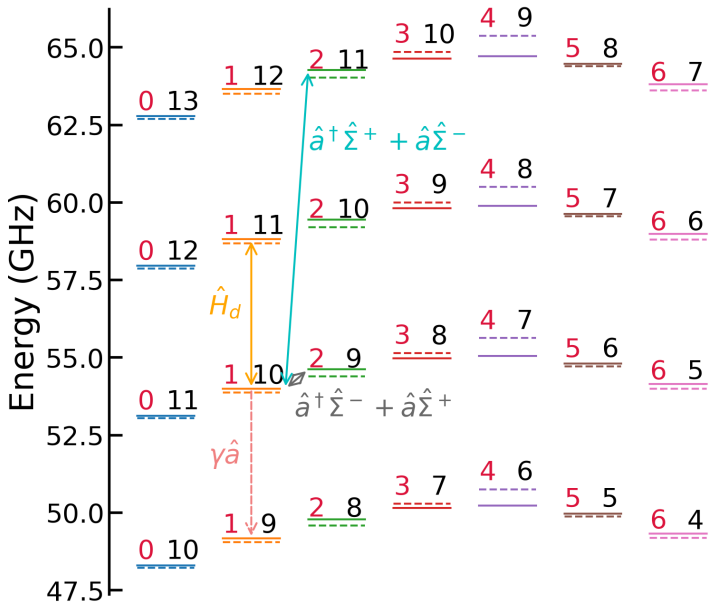

Figure 6-2: Energy diagram of single qubit-resonator system. Solid lines are non-perturbed bare energy levels for qubit and resonator while dashed lines are the eigen-levels of the total Hamiltonian, including the interaction term. The number pairs denote the qubit level (red) and the photon number in the cavity (black). Arrows represent first order transitions caused by different terms that affect the system dynamics. The qubit frequency is 5.695 GHz with 0.212 GHz anharmonicity a The readout resonator frequency is 4.83 GHz and the coupling between qubit and resonator is 0.0786 GHz.

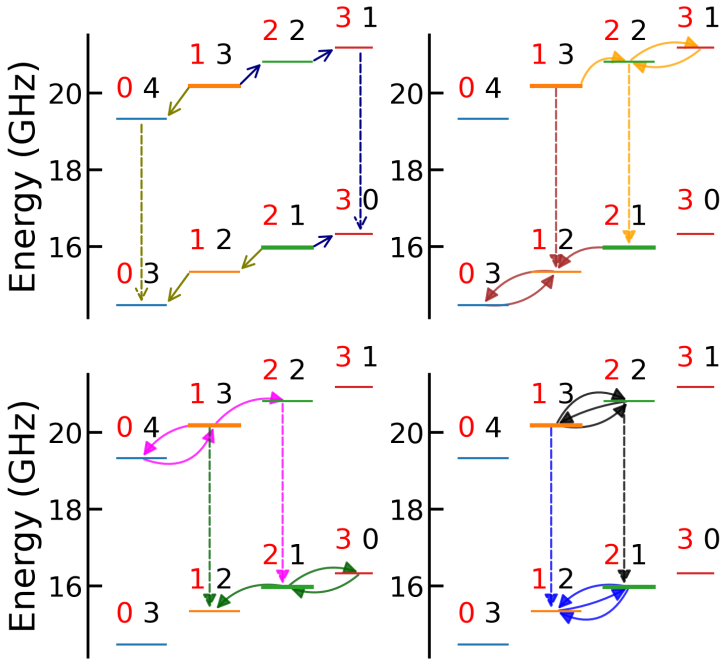

Figure 6-3: Third order transitions between state $\overline{|1,3\rangle}$ and $\overline{|2,1\rangle}$ induced by resonator dissipation during a single qubit readout process. The solid horizontal line segments are the energy levels of the product states. Each panel shows two different processes that are canceling each other. Arrows of the same color belong to the same process. Each solid arrow contribute one order of g and dashed arrows denote the relaxation process caused by resonator photon annihilator $\hat{a}$. For arrows connecting the same two states, higher arrows happen before lower ones.

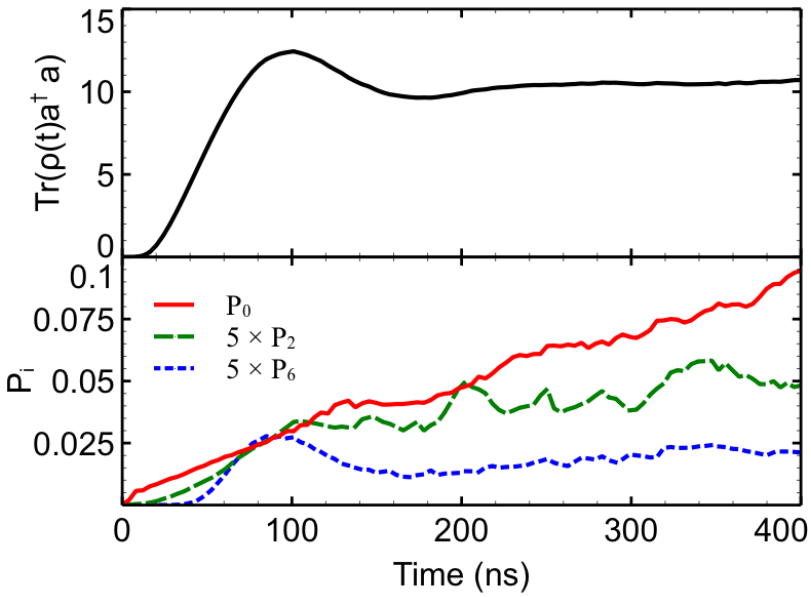

Figure 6-4: Average photon number in the readout resonator and qubit states as a function of time. The qubit frequency is 5.695 GHz with anharmonicity of 0.242 GHz, and the resonator frequency is 4.83 GHz. The interaction between the qubit and the resonator is 0.0786 GHz. The drive amplitude is $A = 15$ MHz, resulting in an average photon number of 10 for 400 ns of measurement time. The qubit is initialized in the first excited state. Only the ground state, second excited state and sixth excited state are shown in the figure since the others have negligible populations and will not be visually observable in linear scale.

Figure 6-2 shows the first order transitions due to different terms that affect the system dynamics. The RWA terms mix bare states with the same excitation numbers while the counter-rotating terms mix next-neighbor RWA ladders and should be negligible for small photon number due to the large energy separation. A closed system initialized in an interacting eigenstate will stay in its initial state. However, the decay operator decreases one excitation in the bare LC basis, which gives non-zero transition rate between eigenstates. The Purcell decay from first excited state of the qubit to the ground state is a typical example of this type of transition. A general rule of thumb for a dispersive measurement is that the quasisteady state should have photon number much less than the critical photon number $n_{crit} = \Delta^2/4g^2$[122]. For our choice of parameters, $n_{crit} \approx 30$. However, in Fig. 6-4, we applied a relatively strong drive, which results in an average photon number of 10. The qubit is initialized in the first excited state. It is shown that although the photon number is still well below the critical photon number, the transitions to other qubit states are not negligible. We do not include Purcell filter in our numerical model, but it is good to keep in mind that the Purcell decay from the first excited state to the ground state is usually well suppressed by Purcell filter and has little effect on the readout SNR, thus will not be discussed here.

Two other examples of Purcell-type of transition that need to be noticed is the qubit excitation due to both the RWA interaction term and accidental resonances between qubit levels within the computational subspace and higher qubit levels, which result in the finite population in the second excited state and sixth excited state in Fig. 6-4. Obvious as it is, the RWA interaction term not only mixes state $\left|1, n\right\rangle$ with $\left|0, n+1\right\rangle$, it also mixes $\left|1, n\right\rangle$ with $\left|2, n-1\right\rangle$, the latter of which leads to excitation of qubit at the cost of photon loss in the resonator. In Fig. 6-3, we take $n = 3$ as an example to show the the third order (in qubit-resonator interaction g) transition processes that gives rise to non-zero transition from state $\overline{\left|1, n\right\rangle}$ to state $\overline{\left|2, n-2\right\rangle}$. Arrows of the same color are of the same transition path. Arrows within the same RWA ladders (solid) are caused by qubit-resonator interaction while vertical (dashed) arrows indicate the photon loss caused by the decay operator $\hat{a}$. Pannel (a) depicts the

paths resulting from combination of the first order of one state and the second order of the other. For example, the first order perturbation gives nonzero $\left|3,0\right\rangle$ component of $\overline{\left|2,1\right\rangle}$ and the second order perturbation gives nonzero $\left|3,1\right\rangle$ component of state $\overline{\left|1,3\right\rangle}$. The decay operator $\hat{a}$ have finite matrix element connecting state $\left|3,1\right\rangle$ and $\left|3,0\right\rangle$. These processes give rise to a third order contribution to the transition from state $\overline{\left|1,3\right\rangle}$ to $\overline{\left|2,1\right\rangle}$. The corresponding arrows are colored navy. Processes in panel (b) (c) and (d) are direct transitions that happen between one state and the third order component of the other state. More detailed analysis of the magnitude of this transition can be found in the appendix. Although this higher order transitions are essentially Purcell decay, the transition frequencies can be closer to the resonator frequency than the qubit frequency. The qubit decay rate of a system with a bandpass Purcell filter is given by[128]

$$\begin{aligned}\Gamma_q =&\kappa_q \frac{g^2}{(\omega_q-\omega_r)^2},\\ \kappa_q =&\frac{|\mathcal{G}|^2}{\kappa_f}\frac{1}{1+\left[\frac{2(\omega-\omega_f)}{\kappa_f}\right]^2},\end{aligned} \tag{6.9}$$

where k_f and ω_f are the decay rate and the frequency of the Purcell filter respectively. ω is the corresponding transition frequency of the qubit and $\mathcal{G}$ is the coupling between the readout resonator and the filter. The filter frequency is usually very close to the readout resonator, which suppresses κ_q significantly in dispersive regime at the qubit frequency. However, transitions with $\omega \approx \omega_r$ won't be strongly suppressed and can survive through the Purcell filter.

In Fig. 6-2, it is shown that for our choice of parameters, when the qubit frequency is larger than the resonator frequency, the qubit state $\left|1\right\rangle$ and $\left|6\right\rangle$ within the same RWA ladder can have very similar energies. This similarity could result in non-negligible mixing between the bare qubit state $\left|1\right\rangle$ and $\left|6\right\rangle$, which, under the act of the decay operator, gives non-zero transitions from $\overline{\left|1,n\right\rangle}$ to $\overline{\left|6,n-6\right\rangle}$. Intuitively, the transitions contain the process of $\left|6,n-5\right\rangle$ relaxing to $\left|6,n-6\right\rangle$, which corresponds to the resonator frequency. This can also be confirmed by numerically calculating the

transition frequency. Numerical calculation gives about 4.7 GHz for photon number smaller than 20 for the set of parameters given in the caption of Fig. 6-2. Therefore, these transitions have frequencies that are closer to the resonator frequency than the qubit frequency, allowing them to survive with with the Purcell filter, which can potentially reduce the SNR for single qubit readout. One resolution to avoid this transition is to tune the drive power to avoid the photon number within the accidental resonance regime. In our numerical model, we choose a drive amplitude of 7 MHz, with a resonator of 6 MHz decay rate, the average resulting photon number is around 4 if we drive the resonator at the average frequency of two qubit states. This relatively weak drive allows us to avoid the accidental transitions from the qubit ground state to the sixth state, at the same time, if we assume a measurement time of $T_m = 400$ ns, the theoretical signal to noise ratio (SNR) for single qubit readout is given by [REF]

$$\mathrm{SNR} = \frac{4\kappa f^2 \chi^2 T_m}{\left(\frac{\kappa^2}{4} + \chi^2\right)^2}, \tag{6.10}$$

whose numerical value for our system is 12.75 and is considered good enough for single qubit readout. However, from similar mechanism, state $\overline{|2, n-2\rangle}$ will be populated as well, which is less likely to be avoided by properly choosing occupied photon number states.

6.3 Readout-induced transitions in a two-qubit system

6.3.1 System Hamiltonian

For a two-qubit system, we add subscript $i = 1, 2$ labels the qubits such that each qubit-resonator (QR) system Hamiltonian is written as

$$\hat{H}_{Q_i R_i} = \hat{H}_{Q_i} + \frac{1}{2}\omega_{R_i}\hat{a}_i^\dagger \hat{a}_i + g_i\left(\hat{\Sigma}_i^+ + \hat{\Sigma}_i^-\right) \otimes \left(\hat{a}_i^\dagger + \hat{a}_i\right), \tag{6.11}$$

In a multi-qubit system where two transmons are coupled capacitively, the total

Hamiltonian includes the Hamiltonians of each qubit-resonator readout element (Q-R) and the capacitive coupling terms between every neighboring qubit pair. To get some insight into the crosstalk that are happening during a measurement, we work on the minimal model of a multi-qubit system, i.e., a single qubit-resonator readout circuit with the transmon coupled to another three-level transmon. This model is sufficient as one studies the effects of measurement on a neighboring qubit when only the resonator of the measured qubit is driven. This minimal multi-qubit system Hamiltonian takes the form

$$H_s = H_{Q_1R_1} + g_{12}(\hat{\Sigma}_1^+ + \hat{\Sigma}_1^-) \otimes (\hat{\Sigma}_2^\dagger + \hat{\Sigma}_2^-) + \text{diag}\{0, \omega_{Q_2}, 2\omega_{Q_2} - \alpha_{Q_2}\}. \tag{6.12}$$

Here, ω_{Q_2} and α_{Q_2} are the qubit frequency and the anharmonicity of the second transmon respectively and g_{12} is the coupling constant between two transmons, which depends on C_{12} in Fig. 6-1.

Since we are focusing on the case when Q1 is been measured, the drive Hamiltonian is

$$H_d = A(t)(\hat{a_1}^\dagger + \hat{a_1}), \tag{6.13}$$

We will still assuming the photon loss rate of the cavity is κ, and the relaxation rates of qubits are γ_1 and γ_2, the system dynamics is described by the same Lindblad equation as Equation (6.8) except that the Hamiltonian is now $H_s + H_d$ and the drive Hamiltonian is given by Equation (6.13).

In our numerical model, we take γ_1 and γ_2 to be zero since the state-of-art with Purcell filter has much longer T_1 and T_2 time than the readout process. The resonator decay superoperator $\mathcal{L}_r = \sqrt{\kappa}\hat{a}$, where κ is the decay rate, whose value is 6 MHz in our numerical model.

6.3.2 Optimizing parameters for two-qubit system

Neighboring qubits are usually designed to be far-detuned to avoid crosstalk. However, readout drive on the cavity excites the first qubit-cavity system (Q1-R1) to non-zero photon states and cause some transitions for Q1 as we have shown above and people found in experiments[129]. Transitions among these new occupied states have different frequencies from the bare qubit frequency. Therefore, potential resonances can still exist between Q2 and Q1-R1 at large qubit-qubit detuning, causing bit flips or transitions to non-computational states of Q2.

It was observed experimentally that the transition of a qubit out of its initial state can be at the order of 10% when its neighboring qubit is measured even at the qubit-qubit detuning around 460 MHz, which is much larger than typical qubit qubit interaction of 15 MHz. And the amount of transition is a non-monotonic function of readout drive power[130, 131], implying resonances between the two transmons that are not captured by the detuning of bare qubit frequencies.

In numerical simulations, one has to keep large enough Hilbert space dimension for Q1-R1 to capture these hidden resonances, which makes solving the Lindblad equation (6.8) exactly an impractical task in reasonable time duration. We numerically solve the Lindblad equation (6.8) using quantum Monte Carlo (QMC) or quantum jump method. Although with less accuracy, the QMC computations can be easily parallelized and gives reasonably accurate results with 500 trajectories in interesting parameter regimes.

Given the final density matrix of the two-transmon system gotten from the numerical simulations, one can calculate the probability of Q2 in its initial state by

$$F(|i\rangle_2) = \left(\mathrm{Tr} \sqrt{\sqrt{\mathrm{Tr}_A\left[\rho_i\right]}\, \mathrm{Tr}_A[\rho(t)] \sqrt{\mathrm{Tr}_A\left[\rho_i\right]}} \right)^2 . \tag{6.14}$$

Figure 6-5 shows the photon number in the readout cavity and the qubit initial state probability as a function of time during the readout drive. With only four photons in the resonator after the system reaches its steady state and large qubit-qubit detuning (589 MHz), there is a 10% chance that Q1 escapes from its initial

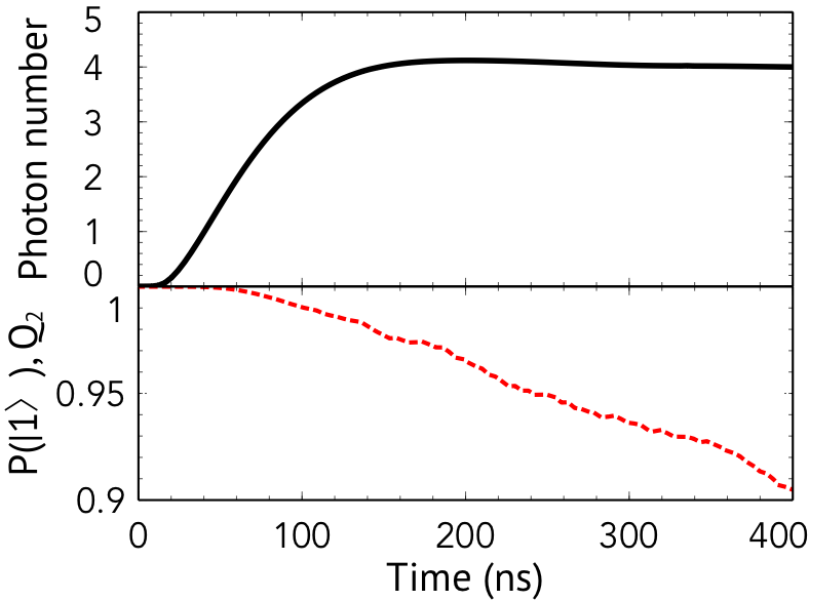

Figure 6-5: Photon number (black solid) and fidelity of Q2 with its initial state $F(|1\rangle)_2$ as functions of time during readout drive on R1. The drive amplitude is 7 MHz and resonator decay rate is 6 MHz, giving rise to about 4 photons in the readout resonator at the end of the drive. The qubit qubit detuning is 589 MHz. Q1 frequency is 5.695 GHz with 0.212 GHz anharmonicity and Q2 frequency is 6.284 GHz with 0.221 GHz anharmonicity. The readout resonator frequency is 4.83 GHz and the coupling between Q1 and R1 is 0.0786 GHz and coupling between Q1 and Q2 is 0.093 GHz.

state.

While this potentially implies much larger qubit qubit detuning is needed to avoid crosstalk, numerical simulations at other qubit-qubit detunings show that even with smaller qubit-qubit detuning, crosstalk can be much less, as shown in Figure 6-6 and 6-7. It is apparent that the relation between transition probability and qubit-qubit detuning is non-monotonic and a better analysis of the potential resonances is thus needed.

6.3.3 Theoretical analysis of crosstalk strength

In this section, we demonstrate a method of analysis on the spectrum of the qubit-resonator systems and the matrix elements of qubit-qubit interaction term that gives an estimate of the overall transition probability, which we call crosstalk strength. This analysis is not intended to give an accurate value for the transition probability, but it reproduce non-monotonicity of crosstalk at the qubit-qubit detuning that agrees well with our numerical simulations, thus can be useful as a guidance to optimize neighboring qubit-qubit detuning to reduce the crosstalk during readout processes. Although we take the qubit-qubit interaction as capacitive form and specifically investigate two-transmon system, we expect this analysis to be a general method that can be used to analyze crosstalk strength with different form of interactions and different qubit systems.

When a qubit is capacitively coupled to another qubit-resonator readout element, the first order transitions happen between levels that are connected by the interaction Hamiltonian, which explicitly takes the form,

$$H_{Q_1Q_2} = g_{12}(\hat{\Sigma}_1^+ + \hat{\Sigma}_1^-) \otimes (\hat{\Sigma}_2^+ + \hat{\Sigma}_2^-). \tag{6.15}$$

Equivalently saying, we can use the first order perturbation theory to approximately quantify the transitions that could happen between qubit two initial state and other final states. For these two-qubit system, given the dimension of Q1-R1, all states with the form of $\overline{|Q_1, R_1\rangle} \otimes |Q_{2,i}\rangle$ that is resonant with another state $\overline{|Q_{1,f}, R_{1,f}\rangle} \otimes |Q_{2,f}\rangle$

can act as a channel for Q2 to escape from its initial state $\left|Q_{2,i}\right\rangle$ to some final state $\left|Q_{2,f}\right\rangle$. For one of the channels, denoting the initial state as $|i\rangle = \overline{\left|Q_{1,i}, R_{1,i}\right\rangle} \otimes \left|Q_{2,i}\right\rangle$ and the final state as $|f\rangle = \overline{\left|Q_{1,f}, R_{1,f}\right\rangle} \otimes \left|Q_{2,f}\right\rangle$. Assuming the corresponding energies are E_i and E_f respectively, there could be a significant transition contribution from one channel if the corresponding matrix element of $H_{Q_1Q_2}$ is comparable to the bare energy difference of the final state and initial state $\Delta E = E_f - E_i$ as long as the initial state of this channel is populated. On average, the transition probability contributed by one channel that consists of initial state $|i\rangle$ and final state $|f\rangle$ is

$$P_{i,f} = \frac{1}{2} \sin^2 \theta_{i,f}, \tag{6.16}$$

where

$$\theta_{i,f} = \arctan \frac{2t}{\Delta E} \tag{6.17}$$

and $t = \langle f | H_{Q_1Q_2} | i \rangle$.

Since the diagonalization of single Q-R system Hamiltonian is a relatively quick calculation, in order to catch all significant transition channels, we diagonalize Q1-R1 Hamiltonian and Q2-R2 Hamiltonian, where the second resonator has frequency 4.6 GHz and the coupling strength between Q2 and R2 is 0.0786 GHz. Adding the second resonator will normalize the qubit frequency slightly but the modification should be small compared to the three level system since we will assume Q2 is always initialized in the ground state or the first excited state with zero photons in R2. Given a Q2 initial state, resonant channels are identified by finding all states of Q1-R1 and Q2-R2 such that the sum of energies of state $\overline{\left|Q_{1,i}, R_{1,i}\right\rangle}$ and state $\overline{\left|Q_{2,i}, 0\right\rangle}$ is close to the sum of energies of state $\overline{\left|Q_{1,f}, R_{1,f}\right\rangle}$ and state $\overline{\left|Q_{2,f}, R_{2,f}\right\rangle}$ compared to the corresponding matrix element of $H_{Q_1Q_2}$.

With multiple resonant channels identified, we can calculate the squared overlap between the final state after the readout drive and states that could easily leak to other levels due to resonance and non-negligible couplings (referred as 'dangerous' state in the following text). Since we expect the Q2 is only weakly coupled to Q1, although there is a non-negligible transition probability for Q2, Q1-R1 system is considered

as a reservoir and only weakly affected by the coupling with Q2. This assumption allows us to use single qubit-resonator dynamic simulations once we filtered out all dangerous states of system Q1-R1 that can induce transitions for Q2. Here we will also assume the that the system spends the majority of time at its steady state in readout process. This assumption, although can introduce some errors, allows us to use the final state density matrix to approximate the time-averaged density matrix along the readout process, thus simplifies the calculation while as we will show later, provide sufficient accuracy for optimizing system parameters.

Adding up the contributions from all the dangerous channels gives an estimate of the transitions probability for Q2 from its initial state as the following form

$$\mathcal{C} = \sum_{\left|i\right\rangle_1 \in \{\left|d\right\rangle\}} \sin^2(\theta)\ {}_1\langle i|\rho_1(t=t_f)|i\rangle_1, \tag{6.18}$$

where $\{\left|d\right\rangle\}$ is the subspace which contains all dangerous initial states. The subscript 1 indicates that we only need to look at dangerous states for Q1-R1 system and $\rho_1(t=t_f)$ is the density matrix of Q1-R1 system at the end of the readout drive.

In Fig. 6-6 and Fig. 6-7, we calculated $\mathcal{C}$ as a function of qubit-qubit detuning for initial state $\overline{\left|0,0\right\rangle} \otimes \left|1\right\rangle$ and $\overline{\left|1,0\right\rangle} \otimes \left|1\right\rangle$ respectively. ρ_1 is the density matrix of Q1-R1 after 400 ns of a 7 MHz readout drive. We reiterate that it should only be considered as a rough estimate for the transition probability that gives a sense of relative strength of the transitions since it does not take into account the time-dependence of the state of the system during the drive and possible coherence between channels. The Figure. 6-6 shows that the detuning of 589 MHz is at the second highest peak, indicating a large amount of transitions for Q2 at this detuning.

Our numerical calculations are shown as blue dots in the two figures, with error bars indicating the deviation introduced by the Monte Carlo sampling method. They are qualitatively consistent with the theoretical estimates. In addition, the theoretical estimate, although with only one dynamic simulation of single Q-R system and simple diagonalization of Q-R Hamiltonian, it predicts the non-trivial non-monotonicity at the same qubit-qubit detuning as the full numerics. Therefore, we argue that it can

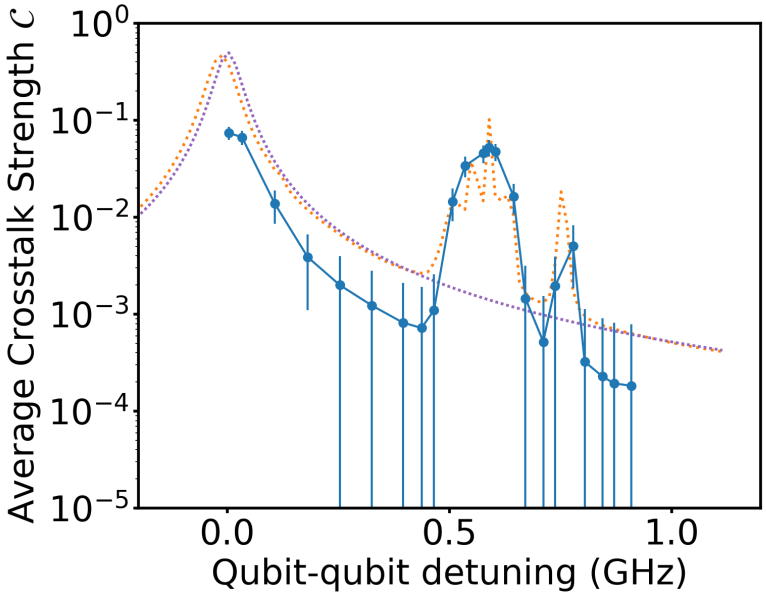

Figure 6-6: Orange line is the average crosstalk strength estimate for 400 ns of resonator drive with amplitude of 7 MHz as a function of qubit-qubit detuning. The first qubit is initialized in the ground state and the second qubit in the first excited state. The lavender dotted line is the estimate for transition before readout drive is applied to the measured qubit, which gives a baseline for how much the transition for a neighboring qubit if only the qubit frequency resonance (transition between the ground state and the first excited state for each qubit) is taken into account. The scattered points are numerical results of infidelity of the second qubit (Q2) compared to its initial state after the readout drive on the first qubit (Q1) at several different qubit detunings close to the regime of the secondary peak of the yellow curve.

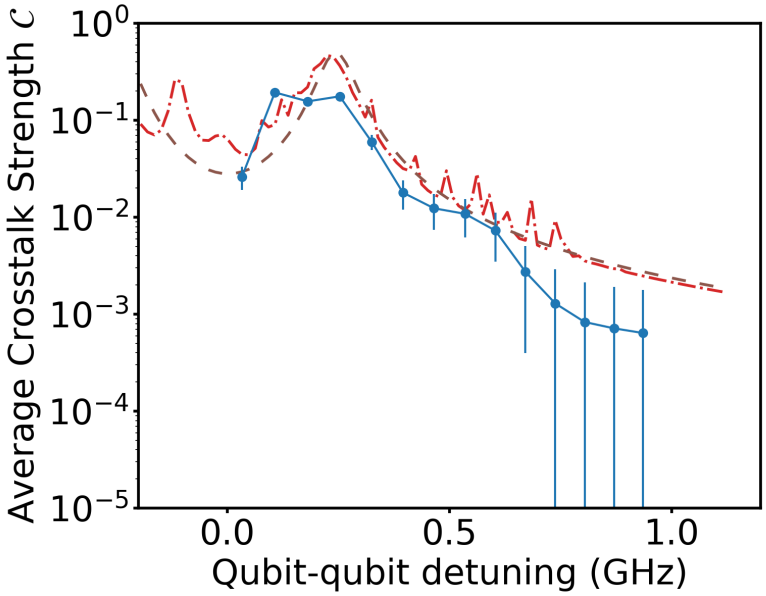

Figure 6-7: Average crosstalk strength estimate for 400 ns of resonator drive with amplitude of 7 MHz as a function of qubit-qubit detuning. Both qubits are initialized in the first excited states. The brown dashed line is the estimate for transition before readout drive is applied to the measured qubit, which gives a baseline for how much the transition for a neighboring qubit if only the qubit frequency resonance (transition between the ground state and the first excited state for each qubit) is taken into account. The blue dots are numerical results of infidelity of the second qubit (Q2) compared to its initial state after the readout drive on the first qubit (Q1) at several different qubit detunings.

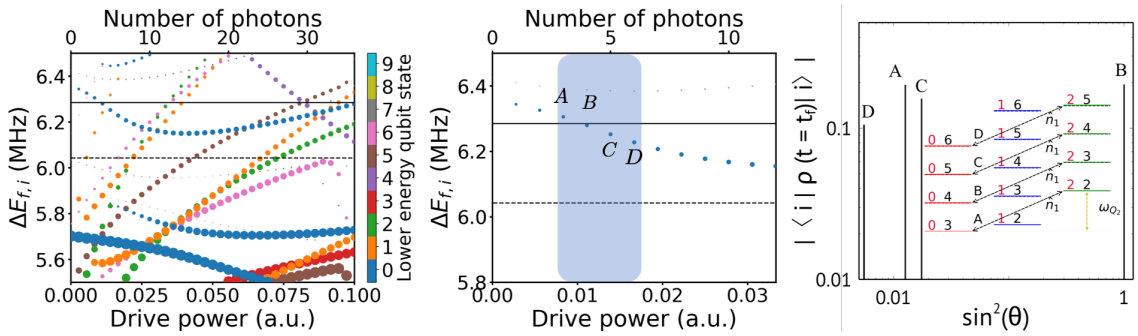

Figure 6-8: (a)A complete transition map plot showing all possible transitions for Q1-R1 system. Each dot represents a possible transition for Q1-R1 induced by the capacitive qubit-qubit coupling Hamiltonian. The dots are sized by the matrix element of (6.15). The vertical axis is the transition frequency between initial state and final state. In principle, all intersections between horizontal lines and significant sized dots can contribute to the crosstalk if the corresponding initial states are populated. The solid black horizontal line is located at the frequency of Q2 and the dashed black horizontal line is located at the transition frequency $\Delta E_{f,i}$ from the first excited state to the second excited state of Q2. The qubit-qubit detuning of 589 MHz. (b) A zoom-in diagram of the resonance area for the two-qubit system. Only transitions that end up at $\overline{|2,n\rangle}$ for Q1-R1 is presented here for a clear view. Four tansitions that are close to the qubit two transition frequency are labeled by A, B, C, D. A represents the transition from $\overline{|0,3\rangle}$ to $\overline{|2,2\rangle}$, B for $\overline{|0,4\rangle}$ to $\overline{|2,3\rangle}$, C for $\overline{|0,5\rangle}$ to $\overline{|2,4\rangle}$ and D for $\overline{|0,6\rangle}$ to $\overline{|2,5\rangle}$. Since they intersect with Q2 transition line from the ground state to the first excited state, they are all associated with excitation of Q2 from the ground state to its first excited state. (c)The squared overlap between the final state of the Q1-R1 system after readout drive and dangerous states defined by a large $\sin^2\theta$, where θ is defined in (6.17) for different qubit-qubit detunings. The labels on the top of each bar represents different corresponding transitions for Q1-R1 system.

be used as a handy guide to optimize the qubit-qubit detuning to reduce the crosstalk.

6.3.4 Readout optimization

Since the transitions happen through resonance between the initial state and some final state, it is important to identify possible resonances and avoid state distribution over these resonant states either by changing the system parameters or drive amplitude. For fixed frequency qubit systems, knowing how to choose proper system parameters to avoid potential crosstalk can also be useful for quantum processor design.

The crosstalk strength estimate plot shown in Section 6.3.3 is useful for optimizing

the qubit-qubit detuning. However, it provides little intuition about what resonances cause the secondary peak and is not convenient for optimizing the readout power, on which people usually have more control in experiments. Here we demonstrate that by overlapping the lines of qubit frequencies of Q2 and an transition map plot of Q1, we can easily identify dangerous states that can experience significant transitions.

An example is shown in Fig. 6-8. In (a), each dot represents a relaxation that can be caused by the interaction Hamiltonian on Q1-R1 from some initial eigenstate $\overline{|Q_{1,i}, R_{1,i}\rangle}$ to some final eigenstate $\overline{|Q_{1,f}, R_{1,f}\rangle}$. The size of the dots is proportional to the magnitude of the matrix elements of (6.15) between initial state $\overline{|Q_{1,i}, R_{1,i}\rangle}$ and final state $\overline{|Q_{1,f}, R_{1,f}\rangle}$. The overlapped two horizontal lines correspond to Q2 frequency between its ground and first excited states (solid black) and between its first and second excited states (dashed black). Assuming Q2 is initially at the ground state, then the dots that are close to the solid black line imply dangerous transitions for Q1-R1 system from $\overline{|Q_{1,i}, R_{1,i}\rangle}$ to $\overline{|Q_{1,f}, R_{1,f}\rangle}$ while exciting Q2 from the ground state to the first excited state. The inverse process can also happen if Q2 is initialized in its first excited state.

The blue-shadowed regions in plots (b) are populated photon state regime after the drive. With the 7 MHz drive amplitude for 400 ns, the average photon number in the readout resonator is around four, as shown in Fig. 6-5. We use a blue shadow to indicate the occupied photon states region. The upper-case-letter-labeled dots are transitions that contribute the most to the transitions, i.e., states with relatively large $\sin^2(\theta)$ and their overlap with the final density matrix of Q1R1 appear as high bars in Fig. 6-8(c). When the labeled states are well covered by the blue shadow in the transition map plots, it suggests strong transitions since the dangerous transition channels that are resonant with the Q2 frequency are populated.

Although less quantitatively, the transition map provides an intuitive visualization of when strong resonances happen and can act as a guidance for the optimization of both readout drive power and neighboring qubit-qubit detuning. Practically, given control on both qubit frequency and readout drive power, we can optimize the qubit-qubit detuning to avoid strong resonance channels. In the transition map plot, it

means we should minimize the intersection between the transition bands of the measured qubit and the qubit frequency lines of a neighboring qubit. Completely avoiding the intersection is almost impossible, preference to steep intersections at transition channels with smaller matrix elements (smaller dot size) should be taken. With controls over the readout drive power, occupied photon states of the system can be optimized such that these states has minimum overlap with the intersections between measured qubit transition bands and neighboring qubit frequencies.

6.4 Conclusion

We have simulated the dynamics of a dissipative two-qubit system driven by a readout drive by QMC method. We showed that non-trivial resonances between higher photon states and a neighboring qubit can happen during a dispersive readout process, causing bit flips or transitions from the initial state of a neighboring qubit. The numerics also showed that these resonances lead to a non-monotonic relation between crosstalk strength and qubit-qubit detuning, i.e., smaller detuning can lead to weaker crosstalk in some regime.

We estimated the transition probability of the neighboring qubit with much simpler calculation than full numerical simulation of the two-qubit system dynamics. Our theoretical estimate qualitatively agrees with the full numerical calculations and predicts the correct qubit-qubit detuning at which strong resonances can happen, providing with a convenient guide to optimize qubit-qubit detuning to reduce the crosstalk.

We also demonstrated that using the transition map plot, we can easily view all possible strong resonances. Optimization of qubit-qubit detuning can be used to avoid strong resonances, thus reducing the crosstalk by decreasing transition channels. At the same time, optimization of drive power can be used to minimize the overlap between the system occupied states and the dangerous initial states that open up strong transition channels thus reducing the crosstalk.

Chapter 7

Concluding Remarks

The goal of building a scalable quantum computer is no doubt a challenging one. Serious efforts need to be made in every aspect of the workflow of a computer. Data input, processing, storage and extraction are all necessary parts of this workflow. In this thesis, we have touched the last three topics in two qubit systems – single-triplet semiconductor qubit and superconducting qubits, both of which are promising candidates as building blocks for practically useful quantum computers.

For singlet-triplet qubit, we focused on the decoherence problem observed in experiments during a coherent manipulation when charge noise is around. After understanding that nuclear fluctuations alone can not explain the low visibility and long decoherence time, we used Bloch-Redfield equations to describe the dynamics of the system and characterize the decoherence with relaxation rate and dephasing with fluctuations in eigenenergies induced by charge noise. The model not only fit well with the experimental data, it also predicts that the low visibility can be easily improved by tuning the tunnel coupling.

For the data processing part of superconducting qubit system, we specifically looked at how high-fidelity two-qubit gates can be implemented by either a tunable coupler or SFQ pulse sequence. Using electrostatically controlled gate to tune the transparency of short semiconductor wire as a tunable coupler connecting two qubits is proposed. This approach will benefit from the mature semiconducting technologies and in principle can reduce crosstalk during single qubit operations and readouts,

which improves scalability of a qubit system.

Another approach for two-qubit control is to use SFQ pulse sequence in place of Microwave drive to coherently control the qubit state. SFQ pulse generators can be better incorporated into superconducting qubit circuits thus is considered as a better solution to scalability in this sense. Before this thesis, both theory and experiment have shown that single qubit gates can indeed be done with SFQ pulses. In this thesis, we explored the possibility of implementing two-qubit gates with SFQ pulses. The numerical simulations were done by solving time-dependent Schrodinger equations (it is written in Lindblad introduced in section 2.2 form in the code without collapse terms).

For the qubit readout, we aimed at understanding of physical processes of the dispersive readout in a multi-qubit system. Single-qubit reaodut process can be done with high fidelity but it remains a challenge to scale this process to a system consisting more qubits. Especially for the case when the interaction between qubits are fixed, crosstalk during qubit readout can change the states of neighboring qubits and introduce errors. Although detuning neighboring qubits far away seem to be a straightforward solution, it is not a scalable solution and it fails to capture some important resonances that do not belong to the computational basis. One brute force method to optimize the system parameters in terms of reducing the crosstalk during single qubit readout is to simulate the system dynamics with different parameters and find the optimal regimes based on the results. Apparently the work load is not quite practical if the system contains a large number of qubits. In this thesis, we provided with a much simpler approach to optimize system parameters that catches the most important crosstalk channels and identify less obvious resonances based on single-qubit simulation calculation and spectral analysis. In this problem, two-level approximation for qubit is not sufficient to include relevant errors during the multi-qubit readout process. But accurately solving a large dimensional system will be time and resource consuming. Therefore,, we applied quantum trajectory (or QMC as introduced in 2.3) method to simulate the dynamics of a two-qubit system with readout resonator during a readout process and confirmed that our theory can be act

as a good guidance to tune the system parameters and reduce crosstalk during qubit readouts. QMC allows one to horizontally scale the calculation and thus can be easily parallelized for a complicated system.

Appendix A

Reduction of the five–level system to a qubit subspace

In this Appendix, we show that the experimental system is well-described by a two-level Hamiltonian by explicitly reducing the five level system to a two-dimensional subspace.

The full five level system, shown in Fig. 3-4 of the main text, is described by the Hamiltonian

$$\hat{H}_0^{(0)} = \begin{pmatrix} \frac{\varepsilon}{2} & t_c & 0 & 0 & 0 \\ t_c & -\frac{\varepsilon}{2} & \frac{h_x}{\sqrt{2}} & h_z & -\frac{h_x}{\sqrt{2}} \\ 0 & \frac{h_x}{\sqrt{2}} & -\frac{\varepsilon}{2} - Ez & 0 & 0 \\ 0 & h_z & 0 & -\frac{\varepsilon}{2} & 0 \\ 0 & -\frac{h_x}{\sqrt{2}} & 0 & 0 & -\frac{\varepsilon}{2} + E_z \end{pmatrix}, \tag{A.1}$$

where we use the standard basis states, given by the $(2,0)$ singlet, the $(1,1)$ singlet and the T_-, T_0 and T_+ $(1,1)$ triplets. Here, ε is the detuning, $E_z = g\mu_B B$ is the Zeeman splitting of triplet states produced by the average magnetic field at two dots, while off-diagonal matrix elements $h_x = g\mu_B \delta B_x$ ($h_z = g\mu_B \delta B_z$) originate from the gradient of magnetic field between the dots in the direction perpendicular to (along) the averaged field B and $t_c(\varepsilon) = t_{c0}\exp(-\varepsilon/\varepsilon_0)$ is the tunnel coupling,

which depends on ε, where $\varepsilon_0 = 125\ \mu$eV is obtained from the experiment [46]. In this theoretical model, as in the experiment, we assume the following energy scale hierarchy: $t_c \gg E_z \gg h_x$.

We first apply a unitary transformation $\hat{W}$ defined by the matrix

$$\hat{W} = \begin{pmatrix} e^{i\sigma_y \frac{\theta}{2}} & \mathbf{0}_{2\times 3} \\ \mathbf{0}_{3\times 2} & \mathbf{1}_{3\times 3} \end{pmatrix}, \quad \theta = \arccos\left(\frac{\varepsilon}{2E_S}\right), \tag{A.2}$$

where $E_S = \sqrt{(\varepsilon/2)^2 + t_c^2}$. This transformation diagonalizes the Hamiltonian (A.1) in the singlet subspace. It is important to note here that the detuning parameter is a function of time, as shown in Fig. 3-4(b). In the transformed frame, we work in the adiabatic, time-dependent basis. The Hamiltonian then becomes:

$$\begin{aligned} \hat{H}_0^{(1)} =& \hat{W}\hat{H}_0^{(0)}\hat{W}^\dagger - i\hat{W}\dot{\hat{W}}^\dagger \\ =& \begin{pmatrix} E_S & i\dot{\theta} & \frac{h_x}{\sqrt{2}}\sin\frac{\theta}{2} & h_z\sin\frac{\theta}{2} & -\frac{h_x}{\sqrt{2}}\sin\frac{\theta}{2} \\ i\dot{\theta} & -E_S & \frac{h_x}{\sqrt{2}}\cos\frac{\theta}{2} & h_z\cos\frac{\theta}{2} & -\frac{h_x}{\sqrt{2}}\cos\frac{\theta}{2} \\ \frac{h_x}{\sqrt{2}}\sin\frac{\theta}{2} & \frac{h_x}{\sqrt{2}}\cos\frac{\theta}{2} & -\frac{\varepsilon}{2} - E_z & 0 & 0 \\ h_z\sin\frac{\theta}{2} & h_z\cos\frac{\theta}{2} & 0 & -\frac{\varepsilon}{2} & 0 \\ -\frac{h_x}{\sqrt{2}}\sin\frac{\theta}{2} & -\frac{h_x}{\sqrt{2}}\cos\frac{\theta}{2} & 0 & 0 & -\frac{\varepsilon}{2} + E_z \end{pmatrix}, \end{aligned} \tag{A.3}$$

where the term $\hat{W}\dot{\hat{W}}^\dagger$ originates from time dependence of the transformation $\hat{W}$ and results in $\dot{\theta}$ terms in $\hat{H}_0^{(1)}$. The time derivative of the transformation angle θ is

$$\dot{\theta} = -2\frac{t_c(\varepsilon) - \varepsilon(\partial t_c(\varepsilon)/\partial\varepsilon)}{\varepsilon^2 + 4t_c^2(\varepsilon)}v, \tag{A.4}$$

where $v = \mathrm{d}\varepsilon/\,\mathrm{d}t$. Below, we assume the longitudinal field $h_z = 0$, in which case the T_0 state decouples from the other four states. We define the qubit states $|0\rangle$ as the ground state and $|1\rangle$ as the lowest excited state of the Hamiltonian. In the limit of $h_x \to 0$, these eigenvectors are the low energy singlet and triplet T_- states with energies $-E_S$ and $E_{T_-} = -\varepsilon/2 - E_z$, respectively. The minimal energy gap

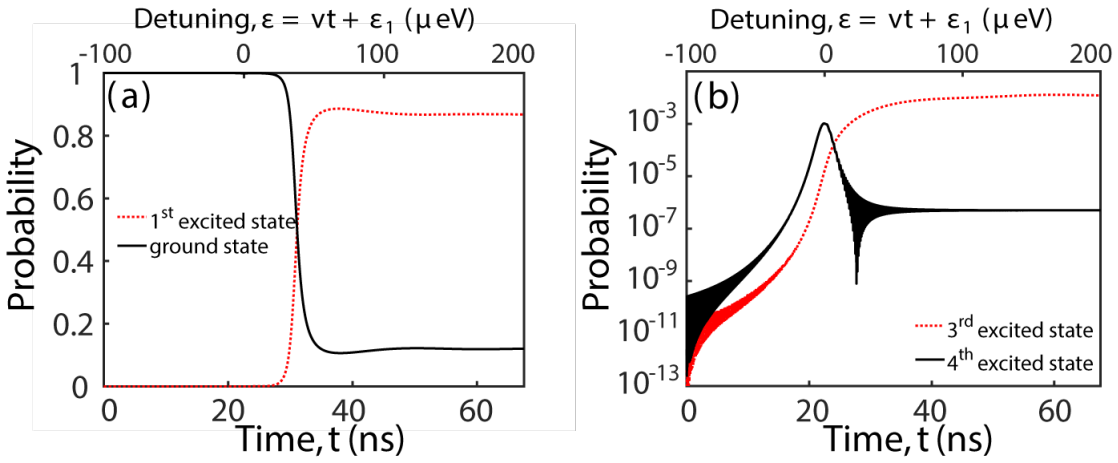

Figure A-1: (a) shows the probability of the ground state $|0\rangle$ and the first excited state $|1\rangle$ of a five-level system through a one-directional ramp, starting from the ground state at detuning $\varepsilon_1 = -100$ μeV. The ramp rate is $v = \mathrm{d}\varepsilon/\,\mathrm{d}t = 4.4$ μeV. Parameters $t_{c0} = 3.4$ μeV, $h = 0.042$ μeV and $g\mu_B B = 0.17$ μeV are the same as for Fig. 3-5 in the main text. Charge noise is not included in this calculation. The occupations of the other three states are too small to be visible in (a). (b) shwows the probability of the third and fourth excited states. The second excited state is not coupled to the other states given that $h_z = 0$, and the probability being in this level remains zero throughout the ramp. Because only two of the energy levels have significant occupation at any time during the evolution, the dynamics can be described using the two-state Hamiltonian (Eq. (3.6) in the main text).

between $\left|1\right\rangle$ and $\left|0\right\rangle$ is $h = h_x\sqrt{2}\cos(\theta(\varepsilon)/2)$ evaluated at the detuning ε^* such that $E_S(\varepsilon^*) = \varepsilon^*/2 + E_z$. This small energy splitting makes it possible to observe the LZS oscillations at relatively low detuning ramp rates $v \lesssim 10$ μeV/ns. These values of the ramp rate are too small to cause transitions out of the qubit subspace, justifying our approximation of a two-level system.

We have tested our approximation of a two-level system by performing simulations on a full five-level system, obtaining the results shown in Fig. A-1(a) and A-1(b). The population of the third excited state (the T_+ state) is found to be of the order of 10^{-2}, and the fourth excited state (the higher energy singlet) is of the order of 10^{-5}. The simulations begin in the initial $(2,0)$ singlet state, which corresponds to the lowest energy state at $\varepsilon_1 = -100\mu$eV. We also assume a ramp rate of $v = (d\varepsilon/dt) = 4.4$ μeV/ns.

Appendix B

Scattering matrix for the H-junction

We construct the scattering matrix $\hat{S}$ for the H-junction as shown in Fig. 4-9. The short-wire scattering matrix $\hat{W}$ takes the form

$$\hat{W} = \begin{pmatrix} r & t \\ t & r' \end{pmatrix}, \tag{B.1}$$

with $r = \sqrt{1-T}e^{i\vartheta}$, $r' = \sqrt{1-T}e^{i(2\eta-\vartheta)}$ and $t = \sqrt{T}e^{i\eta}$, where T is the transmission and ϑ and η are two independent phases.

A beam-splitter scattering matrix $\hat{Y}^{(l,r)}$ is characterized by six parameters as follows:

$$\begin{aligned}
Y_{11} &= a\, e^{i\varphi_{11}}, \quad Y_{12} = b\sqrt{1-a^2}\, e^{i\varphi_{12}}, \\
Y_{13} &= \sqrt{(1-a^2)(1-b^2)}\, e^{i\varphi_{13}}, \\
Y_{22} &= -ab^2 e^{i(2\varphi_{12}-\varphi_{11})} + (1-b^2)e^{i\varphi_{22}}, \\
Y_{23} &= -b\sqrt{1-b^2}\, e^{i\varphi_{13}} \left[a e^{i(\varphi_{12}-\varphi_{11})} + e^{i(\varphi_{22}-\varphi_{12})} \right], \\
Y_{33} &= e^{i2\varphi_{13}} \left[-a(1-b^2)e^{-i\varphi_{11}} + b^2 e^{i(\varphi_{22}-2\varphi_{12})} \right], \\
Y_{\alpha\beta} &= Y_{\beta\alpha}, \quad 1 \le \alpha < \beta \le 3,
\end{aligned} \tag{B.2}$$

where $a, b \in [0,1]$, and $\varphi_{11,22,12,13} \in [0, 2\pi]$. For $a = 1$, $b = 0$, and $b = 1$, the 1, 2, and 3 lead is decoupled to the rest, respectively. The H-junction scattering matrix

elements $S_{\alpha\beta}$ are determined by the linear equations

$$
\begin{aligned}
\begin{pmatrix} S_{00} \\ S_{10} \\ x \end{pmatrix} &= \hat{Y}^{(l)} \begin{pmatrix} 1 \\ 0 \\ rx+ty \end{pmatrix}, \quad \begin{pmatrix} S_{20} \\ S_{30} \\ y \end{pmatrix} = \hat{Y}^{(r)} \begin{pmatrix} 0 \\ 0 \\ tx+r'y \end{pmatrix}, \\
\begin{pmatrix} S_{01} \\ S_{11} \\ x \end{pmatrix} &= \hat{Y}^{(l)} \begin{pmatrix} 0 \\ 1 \\ rx+ty \end{pmatrix}, \quad \begin{pmatrix} S_{21} \\ S_{31} \\ y \end{pmatrix} = \hat{Y}^{(r)} \begin{pmatrix} 0 \\ 0 \\ tx+r'y \end{pmatrix}, \\
\begin{pmatrix} S_{22} \\ S_{32} \\ y \end{pmatrix} &= \hat{Y}^{(r)} \begin{pmatrix} 1 \\ 0 \\ tx+r'y \end{pmatrix}, \quad \begin{pmatrix} S_{02} \\ S_{12} \\ x \end{pmatrix} = \hat{Y}^{(l)} \begin{pmatrix} 0 \\ 0 \\ ty+rx \end{pmatrix}, \\
\begin{pmatrix} S_{23} \\ S_{33} \\ y \end{pmatrix} &= \hat{Y}^{(r)} \begin{pmatrix} 0 \\ 0 \\ tx+r'y \end{pmatrix}, \quad \begin{pmatrix} S_{03} \\ S_{13} \\ x \end{pmatrix} = \hat{Y}^{(l)} \begin{pmatrix} 0 \\ 0 \\ ty+rx \end{pmatrix}.
\end{aligned}
\tag{B.3}
$$

Appendix C

Microwave versus SFQ

Here we will briefly compare the Floquet operator of SFQ pulse trains and microwave drive, to show that they perform similarly when acting on a two-level system.

When applying a transverse microwave drive, the Hamiltonian of the system is

$$H_{tot} = H_0 + H_{mw}, \tag{C.1}$$

where $H_0 = -(\omega_0/2)\sigma_z$ is the qubit Hamiltonian with qubit frequency ω_0, σ_z the Pauli operator, and $H_{mw} = A\left[a\exp(-i\omega_d t) + a^\dagger \exp(i\omega_d t)\right]$ is the Hamiltonian describing the coupling between the qubit and microwave drive, with ω_d the drive frequency, a the annihilator and $a^\dagger$ the creator. In rotating frame, the total effective Hamiltonian takes the form

$$H_{eff} = \begin{pmatrix} -\omega_0/2 & A \\ A & \omega_0/2 - \omega_d. \end{pmatrix} \tag{C.2}$$

Then the Floquet operator is written as

$$\mathcal{F}_{mw} = e^{-iH_{eff}t}. \tag{C.3}$$

In our discussion, we work in a near-resonant regime, where $|w_d - w_0| \ll w_0$. At this limit, the Floquet operator of microwave-driving system is approximately

$$\mathcal{F}_{mw} = 1 - iA\sigma_x T, \tag{C.4}$$

Where $T = 2\pi/\omega_d$ is the drive period. For one cycle of SFQ pulse trains, a delta pulse is immediately followed by a free evolution. In the near-resonant regime, the SFQ Floquet operator of the qubit system takes the form

$$\mathcal{F}_{sfq} = 1 - i\delta\theta\sigma_x \tag{C.5}$$

where $\delta\theta$ is the integral of pulse voltage. Therefore, chosen $\delta\theta = TA$, the SFQ pulse trains can coherently control a two-level system the same as resonant microwave drive with amplitude $A = \delta\theta/T$.

Before we make any detailed explanations on CZ gate implementations, here we present in Fig. C-1 the performance of CZ gates that are realized by near-resonant Microwave drive, SFQ drive and turning-on interaction scheme. The gate errors and gate times are almost exactly the same for SFQ-driven gates and MW-driven gates, whereas the turning-on interacting CZ gates takes longer and presents less errors.

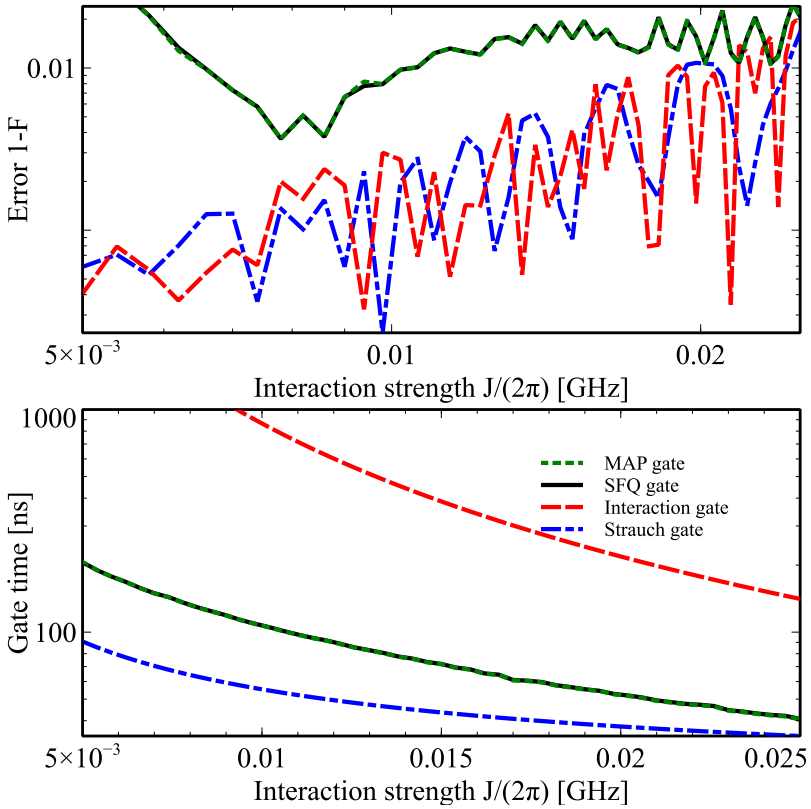

Figure C-1: Fidelity (upper panel) and gate time (bottom panel) of CZ gates as functions of interaction strength J. The black solid line represents the data for SFQ CZ gate and red dashed line represents the interaction CZ gate. In both cases, single qubit gates are applied to factor out the non-conditional phases accumulated due to the finite gate time. Here, $\omega_1/(2\pi) = 4.4$ GHz and $\omega_2/(2\pi) = 4.9$ GHz. The anharmonicity of the first qubit $\alpha_1/(2\pi) = 0.4$ GHz and that of the second qubit $\alpha_2/(2\pi) = 0.25$ GHz, determined by $\alpha_2 = (\omega_2 - \omega_1)/2$. The drive frequency is 1.00053 times the interested transition frequency.

Appendix D

Purcell-type Transitions in Single Qubit Readout

The interaction of qubit and resonator will introduce qubit transitions and the most thoroughly studied transition is the typical Purcell decay from the first excited state to the ground state. The Purcell rate, to the first order purterbation theory in qubit-resonator interaction g, takes a Lorentzian shape and is $\kappa g^2/\Delta^2$, where Δ is the qubit-resonator detuning. In figure D-1, we show the numerical values of this decay rate which automatically takes higher order terms into account. To the right of the qubit frequency 5.695 GHz, the curves decrease monotonically with resonator frequency as expected. The discreteness on the left side, however, should not be interpretted as the true transition rates. The presence of them are due to ambiguity of labeling when two levels become degenerate with each other as we decrease the resonator frequency. For example, when the resonator frequency is at the qubit frequency 5.695 GHz, the state $\left|0,n\right\rangle$ and $\left|1,n-1\right\rangle$ have the same energy. One can find that $\overline{\langle 1,n-2|a|0,n\rangle}$ is none-zero as well, indicating that at the degeneracy point, Purcell decay needs to be better defined to catch the related transitions. Experiments are usually taken when qubit and resonator frequencies are far detuned (by the definition of dispersive readout). At this limit, as mentioned in the main text of Chapter 6, a Purcell filter can easily suppress the qubit decay from the first excited state to the ground state. However, other Purcell-type qubit transitions of higher order in g

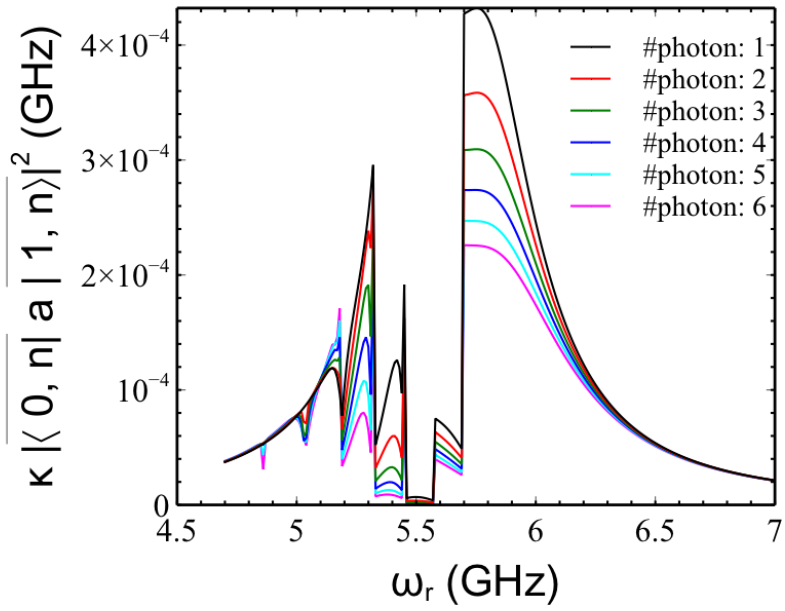

Figure D-1: Purcell decay rate from the state $\overline{|1,n\rangle}$ to $\overline{|0,n\rangle}$ for different value of resonator photon number n as a function of resonator frequency.

may not be efficiently suppressed as their transition frequencies could be closer to the resonator frequency than the qubit frequency. Therefore, in the following discussion, we will quantify these transition rates by analyzing the corresponding matrix element of the decay operator.

Here we'll take the transition from state $\overline{|1,n\rangle}$ to state $\overline{|2,n-2\rangle}$ as an example to show that during single qubit readout process, the photon decay in the resonator causes Purcell-type transitions for the measured qubit.

To see this, we can look at the matrix element of the resonator decay operator $\hat{a}$ corresponding to state $\overline{|1,n\rangle}$ to state $\overline{|2,n-2\rangle}$. If we ignore the descrepancy between the Mathieu basis and the LC basis, which is in higher order of E_c and can be ignored compared to the perturbation due to qubit-resonator interaction, the first order transition vanishes as

$$\begin{aligned}\overline{\langle 2,n-2|}a\overline{|1,n\rangle} \approx & \frac{g\sqrt{2(n-1)}}{\Delta-|\alpha|}\langle 1,n-1|a|1,n\rangle \\ & -\frac{g\sqrt{2n}}{\Delta-|\alpha|}\langle 2,n-2|a|2,n-1\rangle = 0,\end{aligned} \tag{D.1}$$

.

where Δ and g are the detuning and interaction between the qubit and the resonator respectively. The second order in g transition won't exist since the charge interaction between the qubit and resonator only changes the qubit level by one, thus even order in interaction can't lead to transitions between two states with odd qubit level difference. Therefore the matrix element only contains non-zero contribution starting from the third order in qubit-resonator interaction g.

Standard perturbation theory gives the following contributing terms for the matrix element:

$$
\begin{aligned}
me_{21} \approx & g^3 \frac{\sigma_{01}\sigma_{12}\sqrt{n(n-1)}\sqrt{n-1}}{(\Delta-\alpha)(2\Delta-\alpha)} \frac{\sigma_{01}(n+1)}{\Delta} \\
& - \frac{g^3}{2}\left(\frac{\left(\sigma_{23}\sqrt{n-2}\right)^2}{(-\Delta+2\alpha)^2} + \frac{\left(\sigma_{12}\sqrt{n-1}\right)^2}{(\Delta-\alpha)^2}\right)\frac{\sigma_{12}\sqrt{n(n-1)}}{-\Delta+\alpha} \\
me_{12} \approx & \frac{g^3\sigma_{23}^2\sigma_{12}(n-2)}{-\Delta+2\alpha}\frac{\sqrt{n(n-1)}}{(-2\Delta+3\alpha)(-\Delta+\alpha)} \\
& - \frac{g^3}{2}\left(\frac{\left(\sigma_{12}\sqrt{n}\right)^2}{(-\Delta+\alpha)^2} + \frac{\left(\sigma_{01}\sqrt{n+1}\right)^2}{\Delta^2}\right)\frac{\sigma_{12}\sqrt{n(n-1)}}{\Delta-\alpha} \\
me_{03} \approx & g^3\sqrt{n-1}\left(\frac{\sigma_{23}\sigma_{23}(n-1)\sigma_{12}\sqrt{n}}{(-2\Delta+3\alpha)(-\Delta+\alpha)^2}\right. \\
& \left. - \frac{\sigma_{12}\sqrt{n}\left|\sigma_{01}\sqrt{n+1}\right|^2}{(-\Delta+\alpha)^2\Delta} - \frac{\sigma_{12}\sqrt{n}\left|\sigma_{12}\sqrt{n}\right|^2}{(-\Delta+\alpha)^2(-\Delta+\alpha)}\right) \\
& - g^3\frac{\sqrt{n-1}}{2}\left(\frac{\sigma_{12}\sqrt{n}\left|\sigma_{01}\sqrt{n+1}\right|^2}{(-\Delta+\alpha)\Delta^2} + \frac{\sigma_{12}\sqrt{n}\left|\sigma_{12}\sqrt{n}\right|^2}{(-\Delta+\alpha)(-\Delta+\alpha)^2}\right) \\
me_{30} \approx & g^3\sqrt{n}\left(\frac{\sigma_{01}\sigma_{01}\sigma_{12}n\sqrt{n-1}}{(2\Delta-\alpha)(\Delta-\alpha)^2}\right. \\
& \left. - \frac{\sigma_{12}\sqrt{n-1}\left|\sigma_{23}\sqrt{n-2}\right|^2}{(\Delta-\alpha)^2(-\Delta+2\alpha)} - \frac{\sigma_{12}\sqrt{n-1}\left|\sigma_{12}\sqrt{n-1}\right|^2}{(\Delta-\alpha)^2(\Delta-\alpha)}\right) \\
& - g^3\frac{\sqrt{n}}{2}\left(\frac{\sigma_{12}\sqrt{n-1}\left|\sigma_{12}\sqrt{n-1}\right|^2}{(\Delta-\alpha)(\Delta-\alpha)^2} + \frac{\sigma_{12}\sqrt{n-1}\left|\sigma_{23}\sqrt{n-2}\right|^2}{(\Delta-\alpha)(-\Delta+2\alpha)^2}\right),
\end{aligned}
\tag{D.2}
$$

where σ_{ij} is the matrix element of qubit creator corresponding to state i and j. me_{ij} means the terms that connects ith perturbation component of state $\left|\overline{2, n-2}\right\rangle$

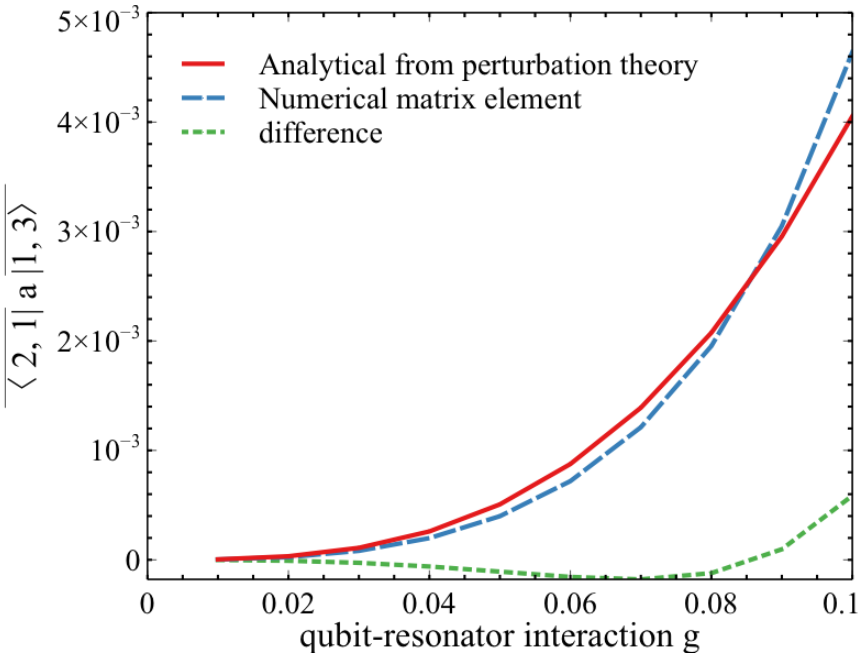

Figure D-2: Matrix element of decay operator $\hat{a}$ of the readout reasonator corresponding to state $\overline{|1,3\rangle}$ and $\overline{|2,1\rangle}$ as a function of qubit-resonator interaction strength g. The solid red line is the analytical matrix element from the third order perturbation theory including only the RWA terms, while the dashed blue line indicates the numerical matrix element. The dotted green line is the difference between the two, which could consist of contributions of both counter-rotating terms and higher order terms.

and jth perturbation component of $\overline{|1,n\rangle}$. Here we have omitted counter-rotating terms and only consider perturbation terms that are within the same RWA ladders as the original states. Each terms is colored in accordance with the arrows in Fig. 6-3.

With qubit-resonator interaction g of 0.0786 GHz, which is typical choice of parameters for the state-of-art transmon systems, the magnitude of the matrix element of the decay operator is about $4-5$ MHz for photon number $n=3$, as shown in Fig. D-2. However, for a larger photon number, counter rotating terms may play more important roles and further complicate the expression.

We also mentioned in the main text that there could be accidental resonance between computational basis and higher qubit levels within the same RWA ladder when the qubit frequency is larger than the resonator frequency. In our choice of parameters, the resonance can happen between the first excited state of the qubit and

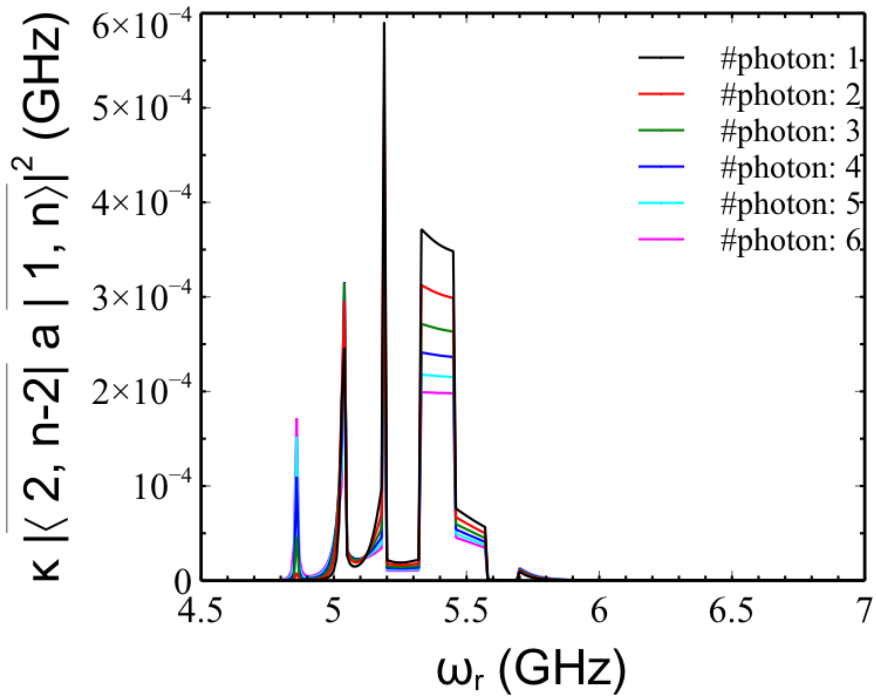

Figure D-3: Transition rate from the state $\overline{|1,n\rangle}$ to $\overline{|2,n-2\rangle}$ for different value of resonator photon number n.

its sixth excited state, which introduces non-zero or even non-negligible corresponding matrix element for the decay operator.

In Fig. D-4, we show transition rate from $\overline{|1,n\rangle}$ to $\overline{|6,n-6\rangle}$ due to the nonzero corresponding matrix element of $\hat{a}$ as a function of resonator frequency. It is alarming that they could be of the same order of magnitude as the transitions from the first excited state of the qubit to the second excited state of the qubit for some photon numbers at resonator frequency of 4.83 GHz. Furthermore, these transitions also have transition frequencies more close to the resonator frequency than the qubit frequency thus they are less likely to be suppressed by the Purcell filter and can potentially harm the single qubit readout fidelity.

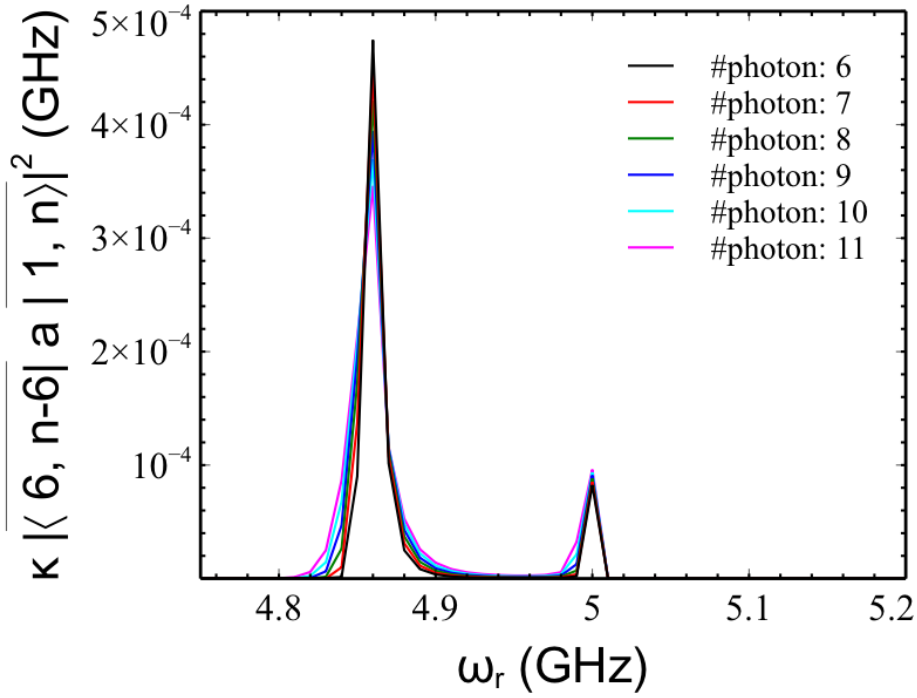

Figure D-4: Transition rate from the state $\overline{|1, n\rangle}$ to $\overline{|6, n-6\rangle}$ for different value of resonator photon number n.

List of Figures

List of Tables

Bibliography

[1] M. A. Nielsen and I. Chuang, *Quantum computation and quantum information*, 2002.

[2] D. P. DiVincenzo, *The physical implementation of quantum computation*, *Fortschritte der Physik: Progress of Physics* **48** (2000), no. 9-11 771–783.

[3] E. Knill, R. Laflamme, and G. J. Milburn, *A scheme for efficient quantum computation with linear optics*, *nature* **409** (2001), no. 6816 46.

[4] X.-D. Cai, C. Weedbrook, Z.-E. Su, M.-C. Chen, M. Gu, M.-J. Zhu, L. Li, N.-L. Liu, C.-Y. Lu, and J.-W. Pan, *Experimental quantum computing to solve systems of linear equations*, *Physical review letters* **110** (2013), no. 23 230501.

[5] S. Barz, I. Kassal, M. Ringbauer, Y. O. Lipp, B. Dakić, A. Aspuru-Guzik, and P. Walther, *A two-qubit photonic quantum processor and its application to solving systems of linear equations*, *Scientific reports* **4** (2014) 6115.

[6] H.-L. Huang, Q. Zhao, X. Ma, C. Liu, Z.-E. Su, X.-L. Wang, L. Li, N.-L. Liu, B. C. Sanders, C.-Y. Lu, et al., *Experimental blind quantum computing for a classical client*, *Physical review letters* **119** (2017), no. 5 050503.

[7] S. Debnath, N. M. Linke, C. Figgatt, K. A. Landsman, K. Wright, and C. Monroe, *Demonstration of a small programmable quantum computer with atomic qubits*, *Nature* **536** (2016), no. 7614 63.

[8] M. G. Dutt, L. Childress, L. Jiang, E. Togan, J. Maze, F. Jelezko, A. Zibrov, P. Hemmer, and M. Lukin, *Quantum register based on individual electronic and nuclear spin qubits in diamond*, *Science* **316** (2007), no. 5829 1312–1316.

[9] N. A. Gershenfeld and I. L. Chuang, *Bulk spin-resonance quantum computation*, *science* **275** (1997), no. 5298 350–356.

[10] A. Imamog, D. D. Awschalom, G. Burkard, D. P. DiVincenzo, D. Loss, M. Sherwin, A. Small, et al., *Quantum information processing using quantum dot spins and cavity QED*, *Physical review letters* **83** (1999), no. 20 4204.

[11] J. Preskill, *Quantum Computing in the NISQ era and beyond*, *Quantum* **2** (2018) 79.

[12] C. Cohen-Tannoudji, J. Dupont-Roc, and G. Grynberg, *Atom-photon interactions: basic processes and applications*, .

[13] F. Bloch, *Generalized theory of relaxation*, *Physical Review* **105** (1957), no. 4 1206.

[14] A. G. Redfield, *On the theory of relaxation processes*, *IBM Journal of Research and Development* **1** (1957), no. 1 19–31.

[15] S. Nakajima, *On quantum theory of transport phenomena: steady diffusion*, *Progress of Theoretical Physics* **20** (1958), no. 6 948–959.

[16] R. Zwanzig, *Ensemble method in the theory of irreversibility*, *The Journal of Chemical Physics* **33** (1960), no. 5 1338–1341.

[17] H. Schoeller and G. Schön, *Mesoscopic quantum transport: Resonant tunneling in the presence of a strong Coulomb interaction*, *Physical Review B* **50** (1994), no. 24 18436.

[18] G. Lindblad, *On the generators of quantum dynamical semigroups*, *Communications in Mathematical Physics* **48** (1976), no. 2 119–130.

[19] R. Alicki and K. Lendi, *Quantum dynamical semigroups and applications*, vol. 717. Springer, 2007.

[20] H.-P. Breuer, F. Petruccione, et al., *The theory of open quantum systems*. Oxford University Press on Demand, 2002.

[21] R. S. Whitney, *Staying positive: going beyond Lindblad with perturbative master equations*, .

[22] Y. Makhlin, G. Schön, and A. Shnirman, *Quantum-state engineering with Josephson-junction devices*, *Reviews of modern physics* **73** (2001), no. 2 357.

[23] Y. Makhlin, G. Schön, and A. Shnirman, *Dissipation in Josephson qubits*, in *New Directions in Mesoscopic Physics (Towards Nanoscience)*, pp. 197–224. Springer, 2003.

[24] F. Haake, *Statistical treatment of open systems by generalized master equations*, in *Springer tracts in modern physics*, pp. 98–168. Springer, 1973.

[25] F. Haake, *On a non-Markoffian master equation*, *Zeitschrift für Physik A Hadrons and nuclei* **223** (1969), no. 4 364–377.

[26] C. Xu, A. Poudel, and M. G. Vavilov, *Nonadiabatic dynamics of a slowly driven dissipative two-level system*, *Physical Review A* **89** (2014), no. 5 052102.

[27] M. Kenmoe, H. Phien, M. Kiselev, and L. Fai, *Effects of colored noise on Landau-Zener transitions: Two-and three-level systems*, *Physical Review B* **87** (2013), no. 22 224301.

[28] V. L. Pokrovsky and N. Sinitsyn, *Fast noise in the Landau-Zener theory*, *Physical Review B* **67** (2003), no. 14 144303.

[29] V. L. Pokrovsky and D. Sun, *Fast quantum noise in the Landau-Zener transition*, *Physical Review B* **76** (2007), no. 2 024310.

[30] M. Wubs, K. Saito, S. Kohler, P. Hänggi, and Y. Kayanuma, *Gauging a quantum heat bath with dissipative Landau-Zener transitions*, *Physical review letters* **97** (2006), no. 20 200404.

[31] M. Wubs, K. Saito, S. Kohler, Y. Kayanuma, and P. Hänggi, *Landau–Zener transitions in qubits controlled by electromagnetic fields*, *New Journal of Physics* **7** (2005), no. 1 218.

[32] K. Saito, M. Wubs, S. Kohler, Y. Kayanuma, and P. Hänggi, *Dissipative Landau-Zener transitions of a qubit: Bath-specific and universal behavior*, *Physical Review B* **75** (2007), no. 21 214308.

[33] P. Nalbach and M. Thorwart, *Landau-zener transitions in a dissipative environment: Numerically exact results*, *Physical review letters* **103** (2009), no. 22 220401.

[34] P. Nalbach and M. Thorwart, *Competition between relaxation and external driving in the dissipative Landau–Zener problem*, *Chemical Physics* **375** (2010), no. 2-3 234–242.

[35] P. P. Orth, A. Imambekov, and K. Le Hur, *Universality in dissipative Landau-Zener transitions*, *Physical Review A* **82** (2010), no. 3 032118.

[36] R. S. Whitney, M. Clusel, and T. Ziman, *Temperature can enhance coherent oscillations at a Landau-Zener transition*, *Physical review letters* **107** (2011), no. 21 210402.

[37] Z. Sun, J. Ma, X. Wang, and F. Nori, *Photon-assisted Landau-Zener transition: Role of coherent superposition states*, *Physical Review A* **86** (2012), no. 1 012107.

[38] J. Avron, M. Fraas, G. M. Graf, and P. Grech, *Landau-Zener tunneling for dephasing Lindblad evolutions*, *Communications in mathematical physics* **305** (2011), no. 3 633–639.

[39] E. Shimshoni and A. Stern, *Dephasing of interference in Landau-Zener transitions*, *Physical Review B* **47** (1993), no. 15 9523.

[40] G. Lindblad, *Entropy, information and quantum measurements*, *Communications in Mathematical Physics* **33** (1973), no. 4 305–322.

[41] J. Koch, *Lecture notes: Theory of Open Quantum Systems*, Winter, 2013. URL: `https://sites.northwestern.edu/koch/teaching/`. Last visited on 2019/8/25.

[42] P. Pearle, *Simple derivation of the Lindblad equation*, *European Journal of Physics* **33** (2012), no. 4 805.

[43] M. B. Plenio and P. L. Knight, *The quantum-jump approach to dissipative dynamics in quantum optics*, *Reviews of Modern Physics* **70** (1998), no. 1 101.

[44] C. H. Wong, M. A. Eriksson, S. N. Coppersmith, and M. Friesen, *High-fidelity singlet-triplet S-T- qubits in inhomogeneous magnetic fields*, *Physical Review B - Condensed Matter and Materials Physics* **92** (2015), no. 4 045403.

[45] J. R. Petta, A. C. Johnson, J. M. Taylor, E. A. Laird, A. Yacoby, M. D. Lukin, C. M. Marcus, M. P. Hanson, and A. C. Gossard, *Coherent manipulation of coupled electron spins in semiconductor quantum dots*, *Science* **309** (sep, 2005) 2180–4.

[46] X. Wu, D. R. Ward, J. R. Prance, D. Kim, J. K. Gamble, R. T. Mohr, Z. Shi, D. E. Savage, M. G. Lagally, M. Friesen, S. N. Coppersmith, and M. A. Eriksson, *Two-axis control of a singlet-triplet qubit with an integrated micromagnet.*, *Proc. Nat. Acad. Sci.* **111** (aug, 2014) 11938–42.

[47] C. Zener, *Non-Adiabatic Crossing of Energy Levels*, *Proc. R. Soc. Lond. A* **137** (1932), no. 833 696–702.

[48] C. Zener, *Dissociation of Excited Diatomic Molecules by External Perturbations*, *Proceedings of the Royal Society A: Mathematical, Physical and Engineering Sciences* **140** (jun, 1933) 660–668.

[49] M. S. Rudner, A. Shytov, L. S. Levitov, D. M. Berns, W. D. Oliver, S. O. Valenzuela, and T. P. Orlando, *Quantum phase tomography of a strongly driven qubit*, *Physical review letters* **101** (2008), no. 19 190502.

[50] S. Ashhab, J. Johansson, A. Zagoskin, and F. Nori, *Two-level systems driven by large-amplitude fields*, *Physical Review A* **75** (2007), no. 6 063414.

[51] S. Shevchenko, S. Ashhab, and F. Nori, *Landau–zener–stückelberg interferometry*, *Physics Reports* **492** (2010), no. 1 1–30.

[52] S. Gasparinetti, P. Solinas, and J. P. Pekola, *Geometric landau-zener interferometry*, *Physical review letters* **107** (2011), no. 20 207002.

[53] S. Ganeshan, E. Barnes, and S. D. Sarma, *Exact Classification of Landau-Majorana-Stückelberg-Zener Resonances by Floquet Determinants*, *Physical review letters* **111** (2013), no. 13 130405.

[54] F. Forster, G. Petersen, S. Manus, P. Hänggi, D. Schuh, W. Wegscheider, S. Kohler, and S. Ludwig, *Characterization of qubit dephasing by Landau-Zener-Stückelberg-Majorana interferometry*, *Physical review letters* **112** (2014), no. 11 116803.

[55] P. Nalbach, J. Knörzer, and S. Ludwig, *Nonequilibrium Landau-Zener-Stueckelberg spectroscopy in a double quantum dot*, *Physical Review B* **87** (2013), no. 16 165425.

[56] X. Tan, D.-W. Zhang, Z. Zhang, Y. Yu, S. Han, and S.-L. Zhu, *Demonstration of geometric Landau-Zener interferometry in a superconducting qubit*, *Physical review letters* **112** (2014), no. 2 027001.

[57] L. D. Landau, *Zur theorie der energieubertragung. II*, *Phys. Z. Sowjetunion* **2** (1932), no. 2 46–51.

[58] E. Stückelberg, *Theory of inelastic collisions between atoms(Theory of inelastic collisions between atoms, using two simultaneous differential equations)*, *Helv. Phys. Acta (Basel)* **5** (1932) 369–422.

[59] S. Shevchenko, S. Ashhab, and F. Nori, *Landau–Zener–Stückelberg interferometry*, *Phys. Rep.* **492** (jul, 2010) 1–30.

[60] J. R. Petta, H. Lu, and A. C. Gossard, *A coherent beam splitter for electronic spin states*, *Science* **327** (2010), no. 5966 669–672.

[61] H. Ribeiro, J. R. Petta, and G. Burkard, *Harnessing the GaAs quantum dot nuclear spin bath for quantum control*, *Phys. Rev. B* **82** (2010), no. 11.

[62] H. Ribeiro, J. R. Petta, and G. Burkard, *Interplay of charge and spin coherence in Landau-Zener-Stückelberg-Majorana interferometry*, *Phys. Rev. B* **87** (jun, 2013) 235318.

[63] H. Ribeiro, G. Burkard, J. R. Petta, H. Lu, and A. C. Gossard, *Coherent adiabatic spin control in the presence of charge noise using tailored pulses*, *Phys. Rev. Lett.* **110** (2013), no. February 1–5, [arXiv:1207.2972].

[64] L. K. Castelano, F. F. Fanchini, and K. Berrada, *Open quantum system description of singlet-triplet qubits in quantum dots*, *Physical Review B* **94** (2016), no. 23 235433.

[65] G. Burkard, D. Loss, and D. P. DiVincenzo, *Coupled quantum dots as quantum gates*, *Phys. Rev. B* **59** (1999), no. 3 2070.

[66] J. M. Nichol, S. P. Harvey, M. D. Shulman, A. Pal, V. Umansky, E. I. Rashba, B. I. Halperin, and A. Yacoby, *Quenching of dynamic nuclear polarization by spin–orbit coupling in GaAs quantum dots*, *Nat. Commun.* **6** (2015) 7682.

[67] K. Wang, C. Payette, Y. Dovzhenko, P. W. Deelman, and J. R. Petta, *Charge relaxation in a single-electron Si/SiGe double quantum dot*, *Phys. Rev. Lett.* **111** (2013), no. July 1–5.

[68] B. Thorgrimsson, D. Kim, Y.-C. Yang, C. Simmons, D. R. Ward, R. H. Foote, D. Savage, M. Lagally, M. Friesen, S. Coppersmith, et al., *Mitigating the effects of charge noise and improving the coherence of a quantum dot hybrid qubit*, *arXiv preprint arXiv:1611.04945* (2016).

[69] O. E. Dial, M. D. Shulman, S. P. Harvey, H. Bluhm, V. Umansky, and A. Yacoby, *Charge noise spectroscopy using coherent exchange oscillations in a singlet-triplet qubit*, *Phys. Rev. Lett.* **110** (2013), no. April 1–5, [arXiv:1208.2023v].

[70] F. Bloch, *Generalized Theory of Relaxation*, *Phys. Rev.* **105** (feb, 1957) 1206–1222.

[71] A. G. Redfield, *On the Theory of Relaxation Processes*, *IBM J. Res. Dev.* **1** (1957), no. 1 19–31.

[72] C. Xu, A. Poudel, and M. G. Vavilov, *Nonadiabatic dynamics of a slowly driven dissipative two-level system*, *Phys. Rev. A* **89** (2014), no. February 052102, [arXiv:1402.4210].

[73] Y. Makhlin, G. Schön, and A. Shnirman, *Dissipative effects in Josephson qubits*, *Chem. Phys.* **296** (jan, 2004) 315–324.

[74] O. Astafiev, Y. A. Pashkin, Y. Nakamura, T. Yamamoto, and J. S. Tsai, *Quantum noise in the Josephson charge qubit*, *Phys. Rev. Lett.* **93** (2004), no. 26 267007.

[75] P. Harvey-Collard, N. T. Jacobson, M. Rudolph, J. Dominguez, G. a. T. Eyck, J. R. Wendt, T. Pluym, J. K. Gamble, M. P. Lilly, M. Pioro-Ladrière, and M. S. Carroll, *Nuclear-driven electron spin rotations in a single donor coupled to a silicon quantum dot*, *preprint arXiv:1512.016061* (2015), no. November.

[76] M. H. Devoret et al., *Quantum fluctuations in electrical circuits*, *Les Houches, Session LXIII* **7** (1995), no. 8.

[77] G. Burkard, R. H. Koch, and D. P. DiVincenzo, *Multilevel quantum description of decoherence in superconducting qubits*, *Physical Review B* **69** (2004), no. 6 064503.

[78] A. Wallraff, D. Schuster, A. Blais, L. Frunzio, J. Majer, M. Devoret, S. Girvin, and R. Schoelkopf, *Approaching unit visibility for control of a superconducting qubit with dispersive readout*, *Physical review letters* **95** (2005), no. 6 060501.

[79] F. W. Strauch, P. R. Johnson, A. J. Dragt, C. J. Lobb, J. R. Anderson, and F. C. Wellstood, *Quantum logic gates for coupled superconducting phase qubits.*, *Phys. Rev. Lett.* **91** (2003), no. 16 167005.

[80] L. DiCarlo, J. Chow, J. Gambetta, L. S. Bishop, B. Johnson, D. Schuster, J. Majer, A. Blais, L. Frunzio, S. Girvin, et al., *Demonstration of two-qubit algorithms with a superconducting quantum processor*, *Nature* **460** (2009), no. 7252 240–244.

[81] R. C. Bialczak, M. Ansmann, M. Hofheinz, E. Lucero, M. Neeley, A. D. O'Connell, D. Sank, H. Wang, J. Wenner, M. Steffen, A. N. Cleland, and J. M. Martinis, *Quantum process tomography of a universal entangling gate implemented with Josephson phase qubits*, *Nat. Phys.* **6** (2010), no. 6 409–413.

[82] T. Yamamoto, M. Neeley, E. Lucero, R. C. Bialczak, J. Kelly, M. Lenander, M. Mariantoni, A. D. O'Connell, D. Sank, H. Wang, M. Weides, J. Wenner, Y. Yin, A. N. Cleland, and J. M. Martinis, *Quantum process tomography of two-qubit controlled-Z and controlled-NOT gates using superconducting phase qubits*, *Phys. Rev. B* **82** (2010), no. 18 1–8.

[83] L. Casparis, T. W. Larsen, M. S. Olsen, F. Kuemmeth, P. Krogstrup, J. Nygård, K. D. Petersson, and C. M. Marcus, *Gatemon Benchmarking and Two-Qubit Operations*, *Phys. Rev. Lett.* **116** (apr, 2016) 150505.

[84] A. Cottet, *Implementation of a quantum bit in a superconducting circuit*. PhD thesis, PhD Thesis, Université Paris 6, 2002.

[85] J. Koch, T. Yu, J. Gambetta, A. Houck, D. Schuster, J. Majer, A. Blais, M. Devoret, S. Girvin, and R. Schoelkopf, *Charge-insensitive qubit design derived from the Cooper pair box*, *Phys. Rev. A* **76** (oct, 2007) 042319.

[86] J. Majer, J. Chow, J. Gambetta, J. Koch, B. Johnson, J. Schreier, L. Frunzio, D. Schuster, A. Houck, A. Wallraff, A. Blais, M. Devoret, S. Girvin, and R. Schoelkopf, *Coupling superconducting qubits via a cavity bus*, *Nature* **449** (2007), no. 7161 443–447.

[87] H. Paik, D. I. Schuster, L. S. Bishop, G. Kirchmair, G. Catelani, A. P. Sears, B. R. Johnson, M. J. Reagor, L. Frunzio, L. I. Glazman, S. M. Girvin, M. H. Devoret, and R. J. Schoelkopf, *Observation of High Coherence in Josephson Junction Qubits Measured in a Three-Dimensional Circuit QED Architecture*, *Phys. Rev. Lett.* **107** (Dec, 2011) 240501.

[88] C. Rigetti, J. M. Gambetta, S. Poletto, B. L. T. Plourde, J. M. Chow, A. D. Córcoles, J. A. Smolin, S. T. Merkel, J. R. Rozen, G. A. Keefe, M. B. Rothwell, M. B. Ketchen, and M. Steffen, *Superconducting qubit in a waveguide cavity with a coherence time approaching 0.1 ms*, *Phys. Rev. B* **86** (Sep, 2012) 100506.

[89] D. Esteve, J.-M. Raimond, and J. Dalibard, *Quantum entanglement and information processing: lecture notes of the Les Houches Summer School 2003*, vol. 79. Elsevier, 2004.

[90] W. Chang, V. Manucharyan, T. Jespersen, J. Nygård, and C. M. Marcus, *Tunneling spectroscopy of quasiparticle bound states in a spinful Josephson junction*, *Phys. Rev. Lett.* **110** (2013), no. 21 217005.

[91] T. W. Larsen, K. D. Petersson, F. Kuemmeth, T. S. Jespersen, P. Krogstrup, J. Nygård, and C. M. Marcus, *Semiconductor-Nanowire-Based Superconducting Qubit*, *Phys. Rev. Lett.* **115** (Sep, 2015) 127001.

[92] G. de Lange, B. van Heck, A. Bruno, D. J. van Woerkom, A. Geresdi, S. R. Plissard, E. P. A. M. Bakkers, A. R. Akhmerov, and L. DiCarlo, *Realization of Microwave Quantum Circuits Using Hybrid Superconducting-Semiconducting Nanowire Josephson Elements*, *Phys. Rev. Lett.* **115** (sep, 2015) 127002.

[93] J. Shabani, M. Kjaergaard, H. J. Suominen, Y. Kim, F. Nichele, K. Pakrouski, T. Stankevic, R. M. Lutchyn, P. Krogstrup, R. Feidenhans'l, S. Kraemer, C. Nayak, M. Troyer, C. M. Marcus, and C. J. Palmstrøm, *Two-dimensional epitaxial superconductor-semiconductor heterostructures: A platform for topological superconducting networks*, *Phys. Rev. B* **93** (Apr, 2016) 155402.

[94] Y.-J. Doh, J. A. van Dam, A. L. Roest, E. P. A. M. Bakkers, L. P. Kouwenhoven, and S. De Franceschi, *Tunable Supercurrent Through Semiconductor Nanowires*, *Science* **309** (2005), no. 5732 272–275.

[95] A. Kringhøj, L. Casparis, M. Hell, T. W. Larsen, F. Kuemmeth, M. Leijnse, K. Flensberg, P. Krogstrup, J. Nygård, K. D. Petersson, and C. M. Marcus, *Anharmonicity of a Gatemon Qubit with a Few-Mode Josephson Junction*, *arXiv:1703.05643* (2017).

[96] Y. Chen, C. Neill, P. Roushan, N. Leung, M. Fang, R. Barends, J. Kelly, B. Campbell, Z. Chen, B. Chiaro, A. Dunsworth, E. Jeffrey, A. Megrant, J. Y. Mutus, P. J. O'Malley, C. M. Quintana, D. Sank, A. Vainsencher, J. Wenner, T. C. White, M. R. Geller, A. N. Cleland, and J. M. Martinis, *Qubit architecture with high coherence and fast tunable coupling*, *Phys. Rev. Lett.* **113** (2014), no. 22 220502.

[97] M. R. Geller, E. Donate, Y. Chen, M. T. Fang, N. Leung, C. Neill, P. Roushan, and J. M. Martinis, *Tunable coupler for superconducting Xmon qubits: Perturbative nonlinear model*, *Phys. Rev. A* **92** (2015), no. 1 012320.

[98] B. van Heck, S. Mi, and A. R. Akhmerov, *Single fermion manipulation via superconducting phase differences in multiterminal Josephson junctions*, *Phys. Rev. B* **90** (Oct, 2014) 155450.

[99] R.-P. Riwar, M. Houzet, J. S. Meyer, and Y. V. Nazarov, *Multi-terminal Josephson junctions as topological matter*, *Nature Communications* **7** (04, 2016) 11167 EP –.

[100] J. S. Meyer and M. Houzet, *Nontrivial Chern Numbers in Three-Terminal Josephson Junctions*, *Phys. Rev. Lett.* **119** (sep, 2017) 136807.

[101] H.-Y. Xie, M. G. Vavilov, and A. Levchenko, *Weyl nodes in Andreev spectra of multiterminal Josephson junctions: Chern numbers, conductances and supercurrents*, *arXiv:1707.07712* (2017).

[102] H.-Y. Xie, M. G. Vavilov, and A. Levchenko, *Topological Andreev bands in three-terminal Josephson junctions*, *Phys. Rev. B* **96** (Oct, 2017) 161406.

[103] C. W. J. Beenakker, *Universal limit of critical-current fluctuations in mesoscopic Josephson junctions*, *Phys. Rev. Lett.* **67** (Dec, 1991) 3836–3839.

[104] J. M. Chow, J. M. Gambetta, A. W. Cross, S. T. Merkel, C. Rigetti, and M. Steffen, *Microwave-activated conditional-phase gate for superconducting qubits*, *New J. Phys.* **15** (2013), no. 11 115012.

[105] J. Ghosh, A. Galiautdinov, Z. Zhou, A. N. Korotkov, J. M. Martinis, and M. R. Geller, *High-fidelity controlled- <math display="inline"> <msup> <mi>σ</mi> <mi>Z</mi> </msup> </math> gate for resonator-based superconducting quantum computers*, *Phys. Rev. A* **87** (feb, 2013) 022309.

[106] L. H. Pedersen, N. M. Møller, and K. Mølmer, *Fidelity of quantum operations*, *Physics Letters A* **367** (2007), no. 1 47–51.

[107] C. Neill, P. Roushan, K. Kechedzhi, S. Boixo, S. V. Isakov, V. Smelyanskiy, R. Barends, B. Burkett, Y. Chen, Z. Chen, B. Chiaro, A. Dunsworth, A. Fowler, B. Foxen, R. Graff, E. Jeffrey, J. Kelly, E. Lucero, A. Megrant, J. Mutus, M. Neeley, C. Quintana, D. Sank, A. Vainsencher, J. Wenner, T. C. White, H. Neven, and J. M. Martinis, *A blueprint for demonstrating quantum supremacy with superconducting qubits*, `arXiv:1709.06678`.

[108] P. Rott and M. J. Feldman, *Characterization of macroscopic quantum behavior using RSFQ circuitry*, *IEEE transactions on applied superconductivity* **11** (2001), no. 1 1010–1013.

[109] R. C. Rey-de Castro, M. F. Bocko, A. M. Herr, C. A. Mancini, and M. J. Feldman, *Design of an RSFQ control circuit to observe MQC on an rf-SQUID*, *IEEE transactions on applied superconductivity* **11** (2001), no. 1 1014–1017.

[110] A. Fedorov, A. Shnirman, G. Schön, and A. Kidiyarova-Shevchenko, *Reading out the state of a flux qubit by Josephson transmission line solitons*, *Physical Review B* **75** (2007), no. 22 224504.

[111] T. A. Ohki, M. Wulf, and M. F. Bocko, *Picosecond on-chip qubit control circuitry*, *IEEE transactions on applied superconductivity* **15** (2005), no. 2 837–840.

[112] M. G. Castellano, F. Chiarello, R. Leoni, G. Torrioli, P. Carelli, C. Cosmelli, M. Khabipov, A. B. Zorin, and D. Balashov, *Rapid single-flux quantum control of the energy potential in a double SQUID qubit circuit*, *Superconductor Science and Technology* **20** (2007), no. 6 500.

[113] V. Kaplunenko and A. Ustinov, *Experimental test of a superconducting digital interface for vortex qubits*, *The European Physical Journal B-Condensed Matter and Complex Systems* **38** (2004), no. 1 3–8.

[114] Y. Yamanashi, M. Ito, A. Tagami, and N. Yoshikawa, *Observation of quantized energy levels in a Josephson junction using SFQ circuits*, *IEEE transactions on applied superconductivity* **15** (2005), no. 2 864–867.

[115] K. G. Fedorov, A. V. Shcherbakova, M. J. Wolf, D. Beckmann, and A. V. Ustinov, *Fluxon readout of a superconducting qubit*, *Physical review letters* **112** (2014), no. 16 160502.

[116] R. McDermott and M. Vavilov, *Accurate qubit control with single flux quantum pulses*, *Physical Review Applied* **2** (2014), no. 1 014007.

[117] E. Leonard Jr, M. A. Beck, J. Nelson, B. G. Christensen, T. Thorbeck, C. Howington, A. Opremcak, I. V. Pechenezhskiy, K. Dodge, N. P. Dupuis, et al., *Digital coherent control of a superconducting qubit*, *Physical Review Applied* **11** (2019), no. 1 014009.

[118] D. Kafri, C. Quintana, Y. Chen, A. Shabani, J. M. Martinis, and H. Neven, *Tunable inductive coupling of superconducting qubits in the strongly nonlinear regime*, *Physical Review A* **95** (2017), no. 5 052333.

[119] J. M. Martinis, S. Nam, J. Aumentado, and C. Urbina, *Rabi oscillations in a large Josephson-junction qubit*, *Physical Review Letters* **89** (2002), no. 11 117901.

[120] I. Siddiqi, R. Vijay, F. Pierre, C. Wilson, M. Metcalfe, C. Rigetti, L. Frunzio, and M. Devoret, *RF-driven Josephson bifurcation amplifier for quantum measurement*, *Physical review letters* **93** (2004), no. 20 207002.

[121] F. Mallet, F. R. Ong, A. Palacios-Laloy, F. Nguyen, P. Bertet, D. Vion, and D. Esteve, *Single-shot qubit readout in circuit quantum electrodynamics*, *Nature Physics* **5** (2009), no. 11 791.

[122] A. Blais, R. Huang, A. Wallraff, and A. Girvin, *Cavity quantum electrodynamics for superconducting electrical circuits: An architecture for quantum computation*, *Physical Review A* **69** (2004), no. 6.

[123] Z. Qi, K. Kechedzhi, V. Smelyanskiy, and G. M. Vavilov, "Dispersive readout in transmon system with red detuned cavity." In preparation.

[124] M. Boissonneault, J. Gambetta, and A. Blais, *Dispersive regime of circuit QED: Photon-dependent qubit dephasing and relaxation rates*, .

[125] A. Wallraff, D. I. Schuster, A. Blais, L. Frunzio, R.-S. Huang, J. Majer, S. Kumar, S. M. Girvin, and R. J. Schoelkopf, *Strong coupling of a single photon to a superconducting qubit using circuit quantum electrodynamics*, *Nature* **431** (2004), no. 7005 162.

[126] J. Koch, T. M. Yu, J. Gambetta, A. Houck, D. Schuster, J. Majer, A. iis, M. Devoret, Girvin, and R. Schoelkopf.

[127] M. H. Devoret and J. M. Martinis, *Quantum Entanglement and Information Processing*. Elsevier, 2003.

[128] E. A. Sete, J. M. Martinis, and A. N. Korotkov, *Quantum theory of a bandpass Purcell filter for qubit readout*, *Physical Review A* **92** (2015), no. 1 012325.

[129] D. Sank, Z. Chen, M. Khezri, J. Kelly, R. Barends, B. Campbell, Y. Chen, B. Chiaro, A. Dunsworth, A. Fowler, E. Jeffrey, E. Lucero, A. Megrant, J. Mutus, M. Neeley, C. Neill, O. PJJ, C. Quintana, P. Roushan, A. Vainsencher, T. White, J. Wenner, A. N. Korotkov, and J. M. Martinis, *Measurement-Induced State Transitions in a Superconducting Qubit: Beyond the Rotating Wave Approximation*, *Phys Rev Lett* **117** (2016), no. 19 190503.

[130] A. K. Jimmy Chen, Mostafa Khezri, *Multiqubit Readout Transitions, APS March meeting 2018*, American Physical Society March Meeting, APS, 3, 2018.

[131] A. Cottet, *Ph.D. thesis*, *Ph.D. thesis* (2002).